[Papers in Palaeontology, 2023, e1481]

# An expanded Smithian–Spathian (Lower Triassic) boundary from a reefal build-up record in Oman: implications for conodont taxonomy, high-resolution biochronology and the carbon isotope record

*by* MARC LEU[1,*], HUGO BUCHER[1], AYMON BAUD[2], TORSTEN VENNEMANN[2], ZONEIBE LUZ[2], MICHAEL HAUTMANN[1] *and* NICOLAS GOUDEMAND[3]

[1]Paleontological Institute & Museum, University Zurich, Karl-Schmid-Strasse 4, 8006 Zurich, Switzerland; marc.leu@pim.uzh.ch
[2]Institute of Earth Sciences, Lausanne University, Geopolis, 1015 Lausanne, Switzerland
[3]Univ. Lyon, ENS de Lyon, CNRS, University Claude Bernard Lyon 1, Institut de Génomique Fonctionnelle de Lyon, UMR 5242, 46 allée d'Italie, F-69364, Lyon Cedex 07, France
*Corresponding author

Typescript received 22 April 2022; accepted in revised form 24 October 2022

**Abstract:** Some 2.7 myr after the Permian–Triassic boundary mass extinction, a stepwise extinction of the nekton (ammonoids and conodonts) ended at the Smithian–Spathian boundary (SSB) during an episode of climate cooling. SSB records from continental shelves are usually affected by an unconformity, suggesting a forced regression of glacio-eustatic origin. Here, we document a new 30-m-thick SSB section from Jebel Aweri (Batain Plain, Oman) that provides an exceptionally complete and expanded record preserved in an exotic block. Most of this SSB section consists of microbial boundstone build-ups with a framework of metazoan bioclasts that formed in shallow water on an offshore seamount. In Wadi Musjah (Hawasina nappes, Oman), another exotic block records the SSB in a deeper water setting represented by Hallstatt-type facies. These two sections provide a unique perspective on the early Spathian rapid re-diversification of conodonts. They led to a thorough revision of conodont taxonomy around the SSB and to the construction of the highest resolution biochronological scheme for this time interval in the Tethys. A total of five SSB sections from Oman representing both offshore seamounts and lower slope deposits were included in a high-resolution, quantitative unitary associations (UA) analysis. The resulting 8 conodont biozones are intercalibrated with ammonoid zones and with the carbonate carbon isotope record ultimately placing the SSB in the interval of separation between $UAZ_3$ and $UAZ_4$. Only the association of *Novispathodus pingdingshanensis* with *Icriospathodus crassatus* can be used to unambiguously characterize the base of the Spathian.

**Key words:** Oman, Smithian, Spathian, conodont, Early Triassic, unitary association.

In the aftermath of the Permian–Triassic boundary mass extinction (PTBME), the nekton (i.e. ammonoids and conodonts) experienced several Early Triassic extinction–diversification cycles (e.g. Orchard 2007; Stanley 2009; Brayard *et al.* 2009; Brayard & Bucher 2015; Wei *et al.* 2015), thus differing from the lingering recovery of the benthos (e.g. Hautmann *et al.* 2015; Friesenbichler *et al.* 2019). The most severe of these nektonic crises spanned the late Smithian and ended at the Smithian–Spathian boundary (SSB). The amount of data published on the SSB increased substantially during the last two decades (e.g. Galfetti *et al.* 2008; Romano *et al.* 2013; Goudemand *et al.* 2019; Zhang *et al.* 2018, 2019; Leu *et al.* 2019; Widmann *et al.* 2020). The Smithian–Spathian transition was associated with large-scale environmental changes such as climatic warming (Sun *et al.* 2012; Song *et al.* 2019), climatic cooling (Romano *et al.* 2013; Zhang *et al.* 2018; Goudemand *et al.* 2019), oceanic anoxia (Sun *et al.* 2015; Clarkson *et al.* 2016), a worldwide positive carbon isotope excursion (CIE) in the carbon isotope budget (Payne *et al.* 2004; Richoz 2006; Galfetti *et al.* 2007*a*, 2007*b*; Korte & Kozur 2010; Hammer *et al.* 2019; Widmann *et al.* 2020; Schneebeli-Hermann *et al.* 2020), and fluctuations in other geochemical proxies such as sulphur isotope (Stebbins *et al.* 2019; Thomazo *et al.* 2019), calcium isotope (Zhao *et al.* 2020) and mercury concentration (Grasby *et al.* 2016). Although conodonts were among the most severely affected organisms during this crisis, their abundance and high



doi: 10.1002/spp2.1481

evolutionary rates are well suited for high-resolution biostratigraphy (e.g. Chen *et al.* 2019; Wu *et al.* 2020). Their concomitant size changes have also been addressed by Chen *et al.* (2013) and Leu *et al.* (2019). Moreover, their oxygen isotopic composition has been used as a proxy for reconstructing the evolution of sea surface temperature during this extinction episode (Sun *et al.* 2012; Romano *et al.* 2013; Goudemand *et al.* 2019).

Most SSB conodont studies were based on sections from continental shelves and slopes such as in South China (e.g. Chen *et al.* 2015), the Northern Indian margin (NIM) (e.g. Krystyn *et al.* 2005; Sun *et al.* 2021), Western USA (Orchard & Zonneveld 2009; Maekawa & Jenks 2021) or the Canadian Arctic (Orchard 2008). In most of these studies based on shelf records, environmental conditions were influenced by a protracted burial of terrestrial organic matter resulting in deposition of black shales (Hammer *et al.* 2019; Schneebeli-Hermann *et al.* 2020), by changes in the weathering intensity and continental runoff (Zhang *et al.* 2018), and by the intercalation of a hiatus of probable glacio-eustatic origin (Davies & Simmons 2018) near the top of the black shales (Widmann *et al.* 2020).

In contrast with shelf records, Smithian and Spathian offshore conodont successions are characterized by more or less condensed limestone. These are usually preserved as exotic blocks such as in Oman (Orchard 1995) and Japan (Koike 1996; Maekawa *et al.* 2018), and are interpreted as seamount deposits reflecting open ocean conditions. In Oman, these offshore records yield large numbers of exceptionally well-preserved and pristine Early Triassic conodont elements (Orchard 1995), even with occasionally preserved basal bodies (Souquet & Goudemand 2020). Such abundant and well-preserved conodont elements are key to understanding the intra- and interspecies-level variation of conodonts, on which a sound and robust taxonomy must be based.

In Oman, PTBME and Early Triassic records from both offshore seamounts and continental shelves have been studied intensively during the last two decades (Krystyn *et al.* 2003; Twitchett *et al.* 2004; Richoz *et al.* 2005, 2014; Richoz 2006; Baud & Bernecker 2010; Richoz *et al.* 2010*a*, 2010*b*; Baud *et al.* 2012; Brühwiler *et al.* 2012; Clarkson *et al.* 2013, 2015, 2016; Brosse *et al.* 2019; Chen *et al.* 2019; Souquet & Goudemand 2020). However, relatively little is known from offshore records in Oman (Tozer & Calon 1990; Orchard 1995; Pillevuit *et al.* 1997; Woods & Baud 2008; Brühwiler *et al.* 2012).

Here, we present the newly discovered Jebel Aweri build-up block, one of the largest Early Triassic exotic blocks embedded in the middle Jurassic Ad Daffah conglomerate (Hauser *et al.* 2001) of the Batain plain. This block is exceptional in that it consists of an expanded shallow water carbonate succession, thus providing unprecedented resolution around the SSB. We also investigated a condensed offshore SSB record at Wadi Musjah in the Hawasina nappes (Brühwiler *et al.* 2012) because of its exceptionally rich conodont succession.

## GEOLOGICAL SETTING

During the Early Triassic (Fig. 1), Oman was located on the Northern Gondwana margin in the Tropical Realm at *c.* 30°S (Baud *et al.* 1990, 2001*a*, 2001*b*; Ricou 1994; Pillevuit *et al.* 1997; Baud 2022). The so-called exotic blocks of Permian–Triassic age found in Oman were deposited on seamounts or tilted plateaus that were rifted and drifted off the Permian–Triassic Oman margin. These blocks were dismembered during the later phase of oceanic convergence and redeposited as olistostromes in the Hawasina basin (Baud *et al.* 2001*a*, 2012; Richoz *et al.* 2014) and the Batain Basin (Hauser *et al.* 2000; Baud *et al.* 2012; Brühwiler *et al.* 2012; Brosse *et al.* 2019). The overthrusting of the Samail ophiolite carried large pieces of the Neo-Tethyan margin onto the autochthonous shelf succession (Béchennec *et al.* 1988; Bernoulli *et al.* 1990; Pillevuit *et al.* 1997; Richoz *et al.* 2005, 2014; Baud *et al.* 2012), and also led to the emplacement of the Hawasina nappes and their Early Triassic series between the autochthonous units below and the Samail ophiolites above.

### *Jebel Aweri*

In eastern Oman, southeast of the town of Sur, the Batain Plain extends *c.* 40 km from west to east and 130 km from northeast to southwest (Fig. 1). According to Roger *et al.* (1991), Béchennec *et al.* (1992) and Wyns *et al.* (1992), the geology of the Batain Plain consists of imbricated allochthonous units, with folded and faulted Permian to Late Cretaceous marine sediments and volcanic rocks that were initially assigned to the Hawasina nappes. In a first approach and due to highly discontinuous exposures, Shackleton *et al.* (1990) interpreted this apparently chaotic tectonic structure as the 'Batain Mélange'. However, according to Immenhauser *et al.* (1998), Schreurs & Immenhauser (1999), Hauser *et al.* (2000, 2002) and Peters *et al.* (2001), structural data indicate a WNW-directed nappe emplacement with NNE–SSW-trending folds and thrusts, thus contrasting with the SSW thrusting vergence of the Hawasina nappes in the Oman Mountains. Immenhauser *et al.* (1998) defined the Batain Group as including the Sal, Guwayza, Wahrah and Fayah formations, and the Qarari, Aseelah, Ad Daffah and Ruwaydah units (Peters *et al.* 2001; Hauser *et al.* 2002). Until recently, no rocks of Griesbachian or Dienerian age have been documented, and this time interval was interpreted as a hiatus in the Batain sedimentary succession by Hauser *et al.* (2001). Numerous

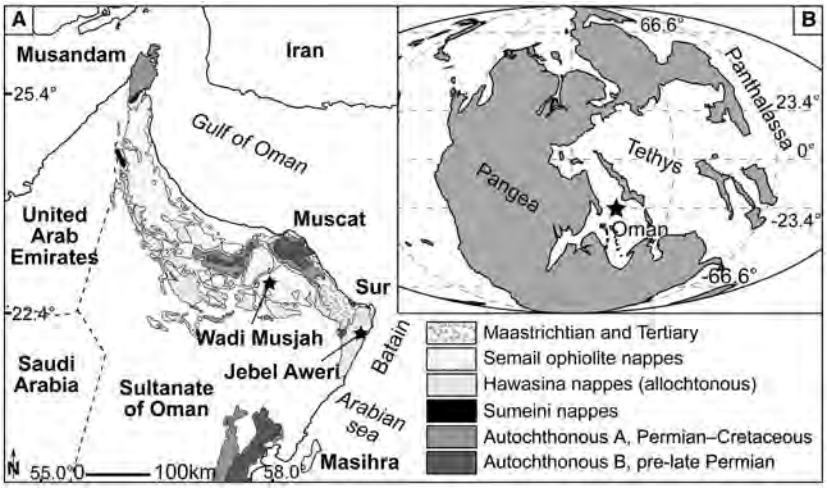


**FIG. 1.** A, simplified geological map of Oman, with the locations of the Wadi Musjah window and the Jebel Aweri block in the Batain area indicated with a star. B, simplified palaeogeographical map of the Early Triassic interval (modified after the PANALESIS plate tectonic model; Vérard 2019).

boulders of Griesbachian and/or Dienerian age were subsequently discovered by Baud (2018) and are represented by blocks of coquina or ammonoid and conodont-rich limestones in the Asselah Unit (Brosse *et al.* 2019).

The new Jebel Aweri build-up block (22°21′24.85″N, 59°45′19.32″E) has been discovered in an area mapped as Ad Daffah Unit by Peters *et al.* (2001) and is illustrated in Figures 2, 3. This Early Triassic reefal succession consists of microbially (dendrolitic stromatolite) cemented clasts and shelly biostromes. An early pervasive cementation of radiaxial, fibrous and botryoidal calcite is the main frame of the build-up. The lower part of the section spans the late Smithian – early Spathian time interval and comprises three units: (A) a lower unit, 11 m thick, subdivided into five biostrome–bioherm cycles; (B) a middle biostrome unit, 9 m thick, with three levels; and (C) a thrombolite-type bioherm upper unit, 2 m thick. The upper part of the section (parts D–F) is entirely Spathian in age and is subdivided into six levels, with a biostrome base and a bioherm upper part (Appendix S1).

### *Wadi Musjah*

The Wadi Musjah locality (22°57′44.50″N, 58°16′1.40″E; Fig. 1) was first reported by Baud *et al.* (2001*a*). The investigated blocks correspond to section 5 of Pillevuit (1993, fig. 2) and the exotic blocks D and F of Brühwiler *et al.* (2012, fig. 2b). Overlain by the Semail ophiolitic nappe, the Wadi Musjah sedimentary units are exposed through a tectonic window reaching into the Hawasina nappes. This 4.6-m-thick section of Hallstatt-type limestone spans the middle Smithian to early Spathian time interval, and represents an approximately sixfold reduction in thickness when compared with the Jebel Aweri build-up section. The Wadi Musjah section (Fig. 4) is subdivided into 11 stratigraphic levels labelled A–K, grouped into six cycles of reddish bioclastic lime mud alternating with light grey to beige, calcite-cemented biostrome. In units B and D the biostrome facies consists of millimetric and fragmentary thin-shelled bivalves that occasionally include intraclasts, peloidal grainstone and centimetric bivalves surrounded by fibrous and blocky calcite cement. In the 2.2 m upper part of the section, biostromal facies are characterized by the occurrence of brachiopod shells, crinoid ossicles and echinoid spines. Further detailed sedimentological descriptions are given in Appendix S1.

## MATERIAL AND METHOD

In addition to microfacies analysis by A. Baud (see above and Appendix S1), stable carbon isotopes and conodonts were densely sampled. The two studied sections are then added to previously described SSB conodont records from Oman in order to analyse biostratigraphic data by means of the unitary associations (UA) method (Guex 1991).

### *Carbon isotopes*

We analysed the micritic matrix of 50 carbonate rock samples from Wadi Musjah and 61 samples from Jebel Aweri for bulk carbonate carbon isotopes ($\delta^{13}C_{carb}$). The samples were carefully cleaned and cut into slabs in order to recover

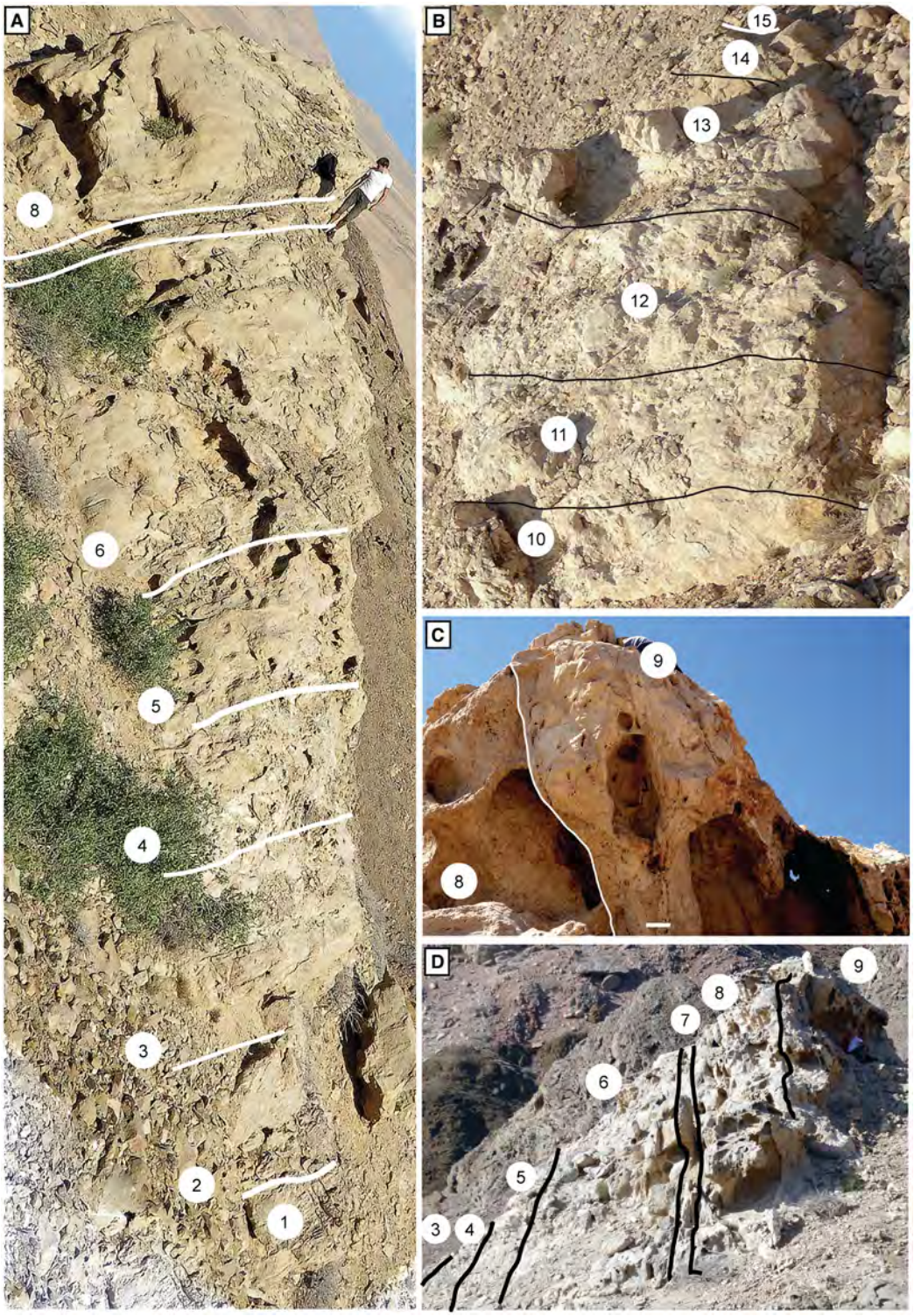


**FIG. 2.** Jebel Aweri. A, outcrop view (from West) of the Jebel Aweri build-up section; the visible lithostratigraphic levels are indicated (Fig. 3); this is the lower block, *c.* 22 m thick; the missing lithostratigraphic level 9 view is shown in C and D. B, outcrop view of the upper block (*c.* 8 m thick) of the Jebel Aweri build-up section; the visible lithostratigraphic levels are indicated. C, outcrop view (from East) of the top of the lower block with the erosive contact between the shell supported biostrome (level 8) and the overlying clast supported bioherm. D, outcrop view (from East) of the Jebel Aweri build-up section; lithostratigraphic level 9 crops out at this side and the view shows an erosive type contact of this level on the underlying shell-supported biostrome (level 8).

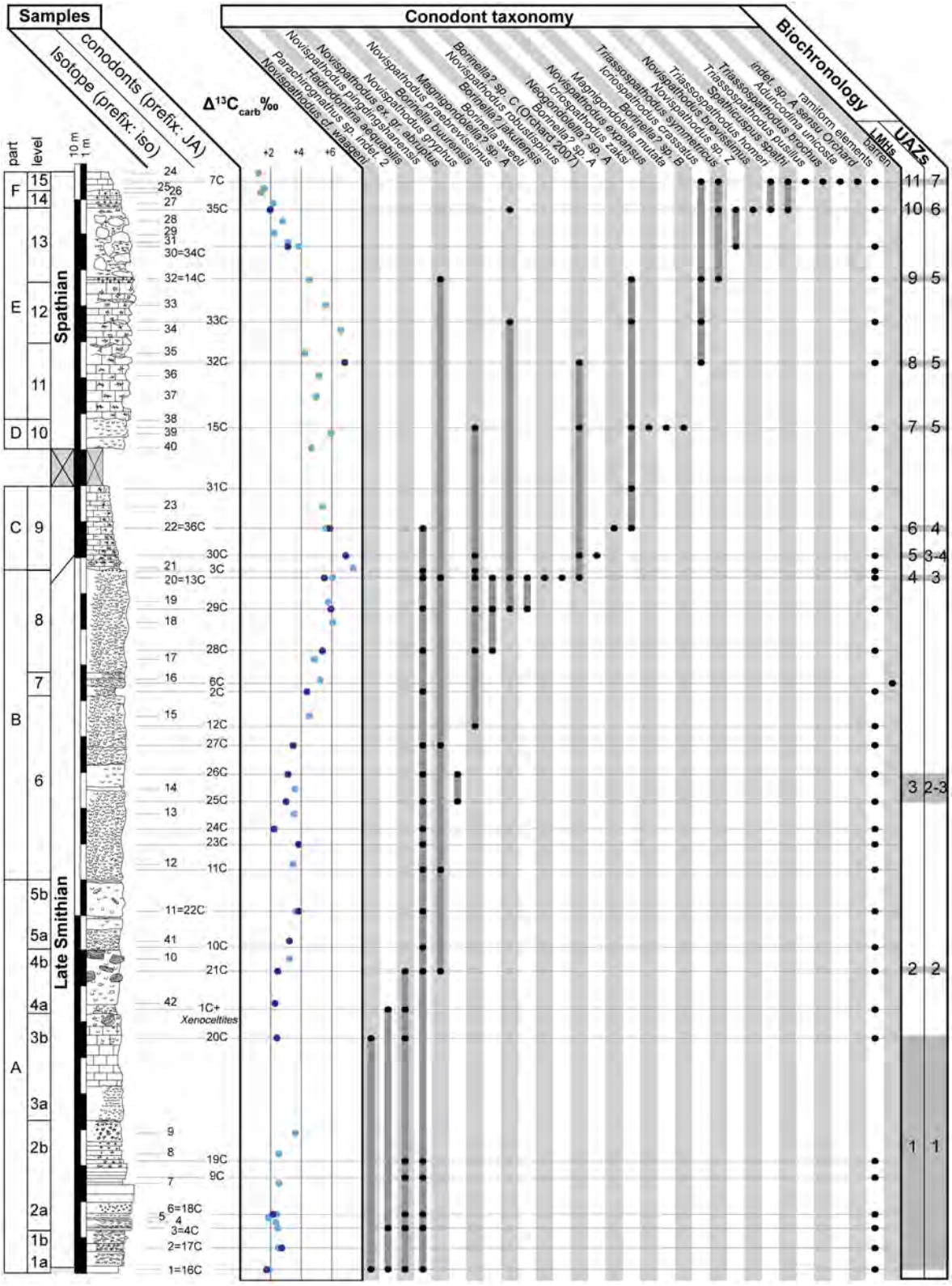


**FIG. 3.** Jebel Aweri, reefal block. Detailed stratigraphic log of the studied interval of the Jebel Aweri section showing the cycles and levels, distribution of conodont taxa, and the $\delta^{13}C_{carb}$ record throughout the Smithian–Spathian boundary interval. Local maximum horizons (LMHs) and unitary associations zones (UAZs) are indicated.

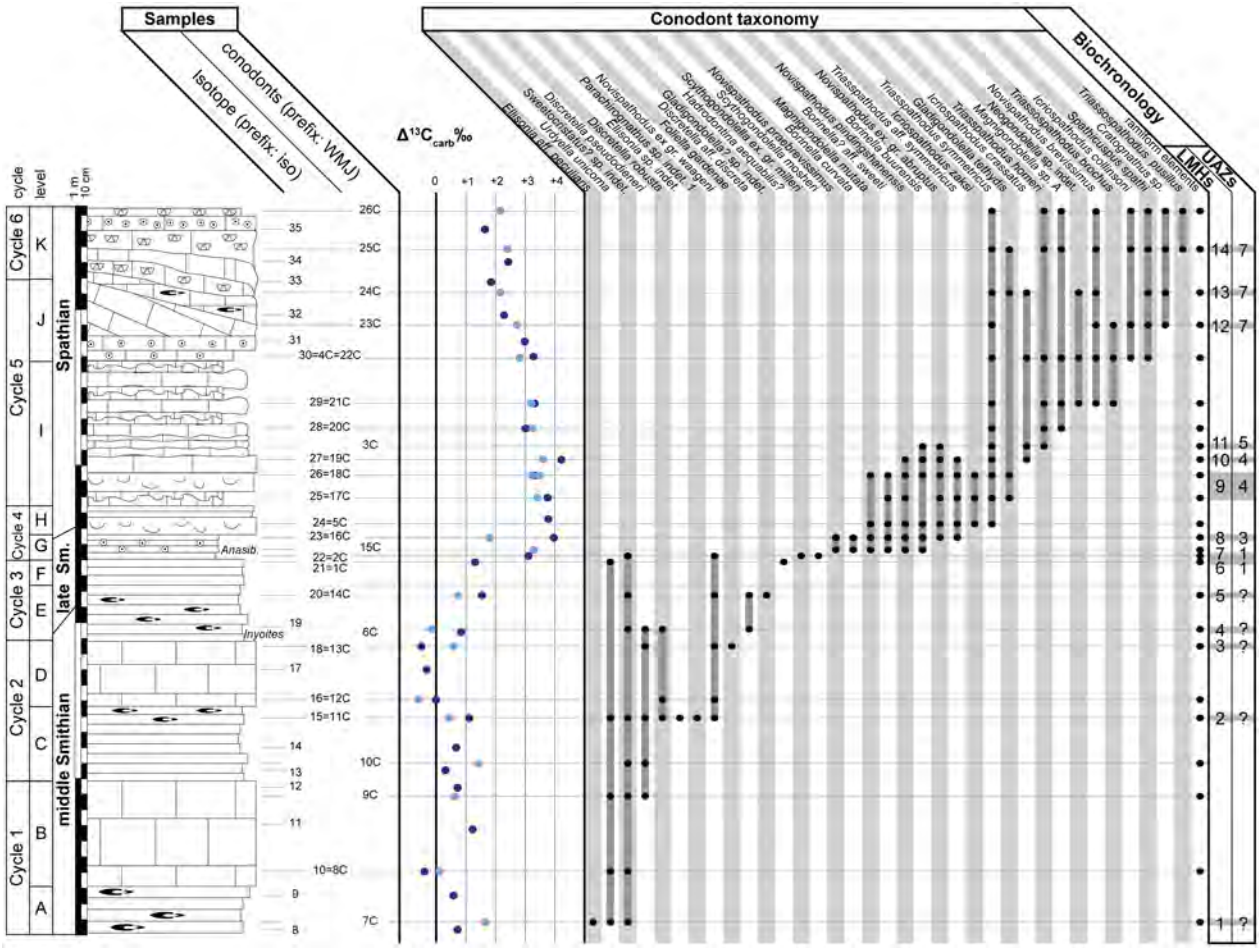


**FIG. 4.** Wadi Musjah. Detailed stratigraphic log of the studied interval of the Wadi Musjah section showing the cycles and levels, distribution of conodont taxa, and the $\delta^{13}C_{carb}$ record across the Smithian–Spathian boundary interval. Local maximum horizons (LMHs) and unitary associations zones (UAZs) are indicated. *Abbreviation: Anasib.*, *Anasibirites*.

unaltered micrite. The most homogenous part was drilled on a sawn surface with a diamond-tipped drill to produce a fine powder. All samples were processed at the Institute of Mineralogy and Geochemistry of Lausanne University and measured with a GasBench II connected to a Finnigan MAT DeltaPlus XL mass spectrometer with a He-carrier gas system (Spötl & Vennemann 2003). Reproducibility (n = 3 per run) of replicate analysis was better than 0.1‰ for standards and 0.15‰ for sediment samples. All reported carbonate carbon isotope results are in the standard δ notation (‰ deviation vs Vienna Peedee Belemnite).

*Conodont sampling and extraction*

A total of 60 samples were collected for conodonts, 26 from Wadi Musjah and 34 from Jebel Aweri. The spacing between the samples varies between 10 cm and 40 cm in the Wadi Musjah section and from 0.5 m to 3 m in the Jebel Aweri section. From Wadi Musjah, samples of 1–3 kg of carbonate rock material were dissolved with a 10% buffered acetic acid solution following the procedure of Jeppsson *et al.* (1999). In Jebel Aweri the same procedure was applied to 10–15 kg samples. The residues were treated by heavy liquid separation using sodium polytungstate (Jeppsson & Anehus 1999), then sieved with a 0.075 mm mesh. The heavy fraction was handpicked under a binocular microscope and selected conodont elements were coated with carbon and imaged using scanning electron microscopy (SEM) (JEOL JSM-6010). Uncoated elements were imaged using a Keyence VHX 6000 digital microscope.

*Unitary associations analysis*

The UA method (UAM) is a deterministic approach based on graph theory, the goal of which is to construct a discrete sequence of mutually exclusive maximal sets of

coexisting species (Guex 1991; Angiolini & Bucher 1999; Monnet & Bucher 2002; Brosse *et al.* 2016). We have used the UAM as implemented in PAST (Hammer *et al.* 2001, 2012) using an older version (v2.17c, 2013) that enables detection and analysis of $Z_4$-type contradictions (Appendix S2, Leu *et al.* 2023, appendix S3, and Results, below). Species documented only from one section were temporarily removed from the analysis via the 'null endemic taxa' option.

Five sections from Oman (Wadi Musjah (this study), Jebel Aweri (this study), Jebel Safra (Orchard 1995), Radio Tower (Chen *et al.* 2019) and Wadi Bani Khalid (Chen *et al.* 2019)) were included in the analysis. Sections with only very sparse conodont occurrences were not included (e.g. Baud *et al.* 2012; Clarkson *et al.* 2013, 2016). Taxonomic revisions were made to ensure the consistency of the dataset using all published material (see Systematic Palaeontology, below, Appendix S2 and Leu *et al.* 2022, appendix S3).

The conodonts from Jebel Safra described by Orchard (1995) were collected from Hallstatt-type ammonoid-bearing limestones (Tozer & Calon 1990). These samples yielded exceptionally well preserved early–middle Spathian conodonts (Orchard 1995). Chen *et al.* (2019) studied Smithian and Spathian conodonts from three different Tethyan areas, two of which are in Oman: the Radio Tower section and the Wadi Bani Khalid section, from which carbonate carbon isotopes were also measured. The Radio Tower section consists of distal turbidite deposits and represents a distal slope setting of the Al Jil Formation. The Wadi Bani Khalid section consists of more distal deposits of the same formation (Béchennec *et al.* 1990; Chen *et al.* 2019).

## RESULTS

In the Batain Plain, Lower Triassic shallow water exotic blocks such as that of Jebel Aweri can be easily mistaken for blocks of Permian reef limestone. The Jebel Aweri reef facies is composed of thick coquinas including brachiopods, bivalves, sponges and binding thrombolites. The benthic macrofauna identified by M. Hautmann is exclusively epifaunal and includes *Pexidella*, *Eumorphotis*, *Myalinella* and enoliid gen. nov.? (similar to '*Pecten*' *praemissus* Bittner, 1901) in sample JA2C and *Bakevellia* and *Promyalina* in sample JA6C (Fig. 3).

The uppermost part of the section (Unit F) shows a pronounced deepening with a succession consisting of crinoidal limestone overlain by reddish, pelagic micritic limestone. *Xenoceltites*, a cosmopolitan ammonoid genus typical of the late Smithian *Glyptophiceras*/*Xenoceltites* ammonoid zone, occurs in Unit 4. The detailed conodont record of Jebel Aweri is shown in Figure 3.

Only a few late Smithian ammonoids were found in Wadi Musjah. These were all assigned to *Anasibirites*, a genus restricted to the early late Smithian, which provides a useful intercalibration for the conodont succession. The stable carbon isotope curve obtained from Wadi Musjah shows the diagnostic excursions recognized globally around the SSB. In particular, the latest Smithian $\delta^{13}C$ positive shift occurs in units E, F and G, in less than 60 cm of strata, illustrating the low sedimentation rate of this relatively deep-water offshore seamount. Associated small brachiopods assigned to *Pexidella* and crinoid spines were most likely to have been transported from adjacent and shallower parts of the same seamount. The previously known oldest occurrence of *Pexidella* was no older than Anisian, thus illustrating the fact that the recovery of brachiopods is still poorly documented. The extremely rich conodont record from Wadi Musjah is shown in Figure 4.

### *Carbonate carbon isotopes*

The C-isotope values of Wadi Musjah show a positive excursion from 0 to +4.5‰ during the late Smithian, in agreement with the carbon isotope records from Wadi Bani Khalid (Chen *et al.* 2019) and from other Tethyan sections (e.g. Galfetti *et al.* 2007*a*; Leu *et al.* 2019). Values fluctuate between 0‰ and +1‰ during the middle Smithian; during the late Smithian, a positive excursion peaks at +4‰ at the boundary between units G and H; and values steadily decrease to *c.* +2‰ towards the top of the section. The positive excursion, which corresponds to 60 cm of strata in Wadi Musjah, is stretched over *c.* 20 m of strata in Jebel Aweri. In Jebel Aweri the C-isotope values range from +2‰ in the late Smithian to a *c.* +6.5‰ at the end of the positive excursion near the SSB. The magnitude of the positive excursion (4.5‰) is the same as in Wadi Musjah, but the positive *c.* 2‰ offset in absolute values probably reflects the difference in bathymetry (Meyer *et al.* 2011) between these two sections.

### *Conodonts*

Of the 60 analysed samples, 59 yielded conodont elements. All recovered conodonts show pristine preservation, with a conodont alteration index (CAI) of 1. From Jebel Aweri, more than 300 $P_1$ elements were recovered. Three samples (JA2C, JA10C and JA17C) produced only ramiform elements. Six samples (JA6C, JA22C, JA23C, JA24C, JA32C and JA34C) were monospecific and produced a maximum of 5 $P_1$ elements each (Fig. 3). In Wadi Musjah, all samples yielded abundant conodonts

and more than 1500 $P_1$ elements were recovered (Fig. 4).

### *Unitary associations analysis*

The first run led to the detection of 24 contradictions and 31 $Z_4$ cycles. At this initial stage, only three cliques were involved in cycles, which indicates that the conodont dataset was of good quality.

*Foliella gardenae*, presumably a Smithian species as documented in the Radio Tower and Wadi Musjah sections, was reported to co-occur with the early Spathian species *Triassospathodus symmetricus* in Wadi Ban Khalid (Chen *et al.* 2019). The biochronologic analysis showed that this association was involved in many contradictions that could not be easily solved. Because the Wadi Bin Khalid section consists partly of mudstones and breccias composed of both intra- and extraclasts, this association probably results from reworking. Pending further work, *F. gardenae* was treated here as a very rare and possibly long-ranging, facies-dependent taxon that was therefore removed from the analysis.

Similarly, the reported association of *Scythogondolella milleri* with *Icriospathodus crassatus* and *Triassospathodus symmetricus* (Chen *et al.* 2019) is very surprising because it has not been documented anywhere else in the world. In no other section does the range of *Sc. milleri* overlap with the late Smithian positive CIE (Orchard 2007, 2008; Zhang *et al.* 2019; Qiu *et al.* 2019). Hence, its range was here reduced up to RT22a in the Radio Tower section and up to WBK05/14 in the Wadi Bani Khalid section.

Because all illustrated specimens of *Novispathodus curtatus* in Chen *et al.* (2019) are here re-assigned to *Nv. brevissimus* (see Systematic Palaeontology, below), we also assumed that *Nv. curtatus* from bed RT36 (not illustrated) could be re-assigned to *Nv. brevissimus*. Because the association *Nv. abruptus–Nv. triangularis* is documented in other sections (e.g. Jebel Safra; Orchard 1995), the range of *Nv. abruptus* was extended up to WBK14 in the Wadi Bani Khalid section where it should virtually co-occur with *Nv. triangularis*.

Finally, *Neogondolella* ex gr. *jakutensis* was removed from the dataset. This species was involved in most of the remaining $Z_4$ cycles and many specimens illustrated as *Neogondolella* ex gr. *jakutensis* by Chen *et al.* (2019) lack the diagnostic features of this species (i.e. a narrow platform with a conspicuous terminal cusp and no posterior brim). Some of these specimens were here re-assigned to other taxa (see Systematic Palaeontology, below).

After these modifications were made, the UAM analysis no longer detected contradictions, with the exception of a single $Z_4$ cycle. The latter involves *Nv. brevissimus*, *Triassospathodus brochus*, *Nv. tahoensis* and *Nv. triangularis*. Because all of these taxa are exclusively known from the Spathian, the resolution of this $Z_4$ cycle is here not necessary for the definition of the SSB. A total of 13 preliminary UAs were obtained. UAs are useful for correlations only if they have a large enough lateral reproducibility (Fig. 5). The UAM automatically computes this parameter and produces recommendations for the merging of UAs in order to optimize the resulting lateral reproducibility of the final biozonation. The preliminary $UA_2$, $UA_4$, $UA_8$, $UA_9$, $UA_{10}$ and $UA_{12}$ are each identified in a single section only, and therefore are of little value for correlation purposes. On the basis of the dissimilarity index, the high frequency of involved arcs, the fact that Jebel Aweri is by far the most expanded SSB section and the merging recommendations of PAST, we finally merged the following preliminary UAs: $UA_1$ and $UA_2$ with $UA_3$, $UA_7$ with $UA_8$, and $UA_{10}$ and $UA_{11}$ with $UA_{12}$. That operation produces a referential of eight unitary association zones (UAZ) that are defined for the five analysed sections (Fig. 5). We propose to place the SSB within the separation interval between $UAZ_3$ and $UAZ_4$. *Icriospathodus zaksi*, *Ic. crassatus* and *Tr. symmetricus*, all typical Spathian taxa, have their oldest occurrence in $UAZ_4$. This definition is also in agreement with the chemostratigraphic positioning of the SSB based on carbon isotope analysis proposed by Zhang *et al.* (2019). In the present dataset, only Wadi Musjah and Jebel Aweri (Fig. 6) contain $UAZ_3$ and $UAZ_4$, both of which are needed for an accurate positioning of the SSB.

### *$UAZ_1$*

*Content.* *Scythogondolella mosheri*, *Nv.* ex gr. *waageni*, *Sc. milleri*, *Hadrodontina aequabilis*, *Nv. pingdingshanensis*, *Borinella* aff. *buurensis*.

*Age.* Late Smithian.

*Geographical distribution in Oman.* Jebel Aweri, Wadi Musjah, Radio Tower, Wadi Bani Khalid.

*Characteristic species.* *Scythogondolella mosheri*, *Sc. milleri and Ha. aequabilis*.

*Characteristic pair of species.* *Novispathodus* ex gr. *waageni* with *Nv. pingdingshanensis*.

*Comment.* $UAZ_1$ overlaps with the *Anasibirites* beds in Wadi Musjah. Note that there is no lower bound for $UAZ_1$ in this section. *Novispathodus* ex gr. *waageni* is a

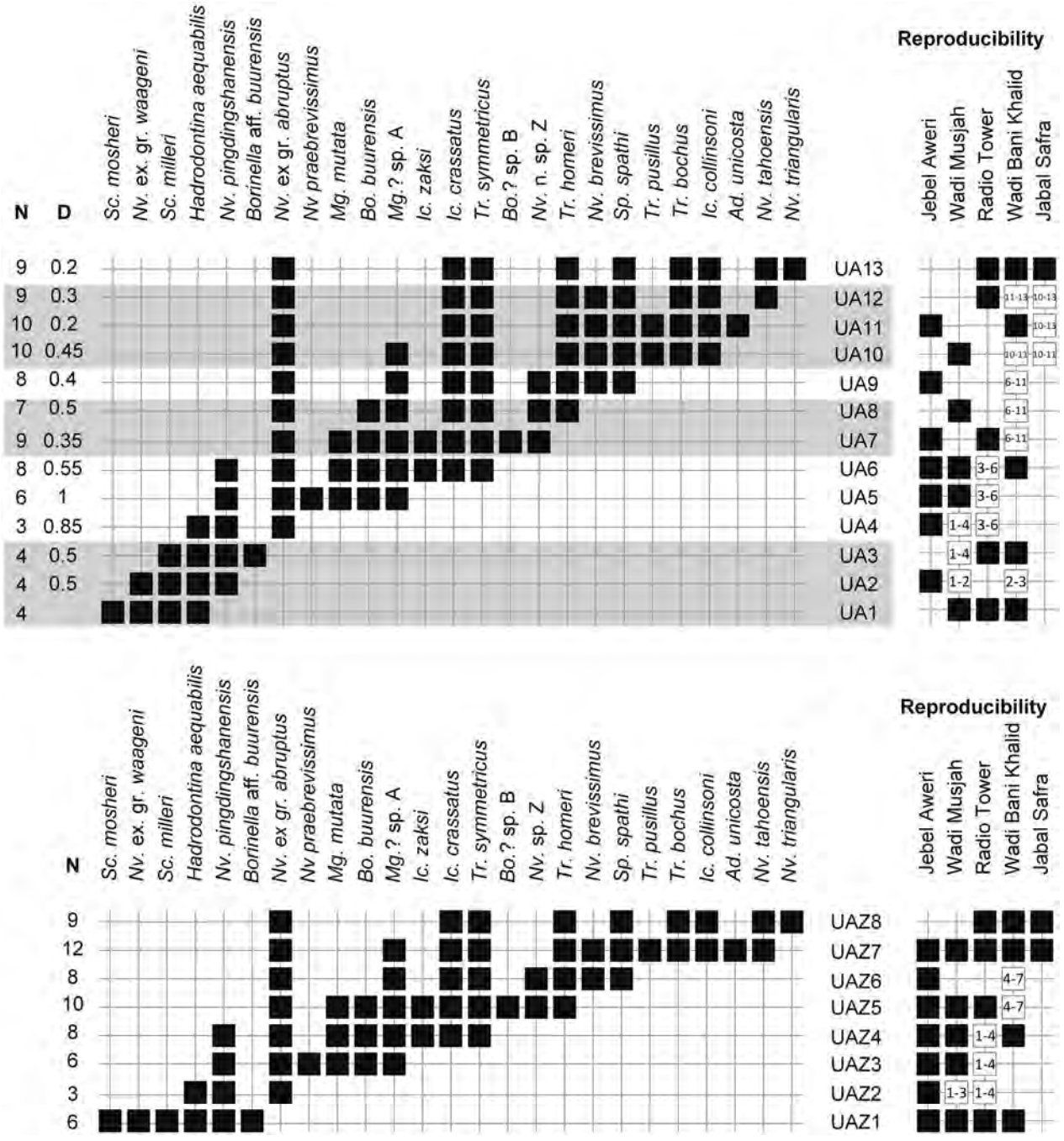


**FIG. 5.** Sequences of unitary association (UAs), unitary association zones (UAZs), lateral reproducibility and dissimilarity index (D) resulting from the biochronological analyses in the five sections in Oman from the final run. The grey shading in the upper figure highlights the poor lateral reproducibility and/or poor dissimilarity index of the $UA_1$, $UA_2$, $UA_3$, $UA_7$, $UA_8$, $UA_{10}$, $UA_{11}$ and $UA_{12}$. These 13 UAs were merged into a final total of 8 UAZs (lower figure). The Smithian–Spathian boundary is within the interval of separation between $UAZ_3$ and $UAZ_4$.

long-ranging species spanning the entire Smithian, and therefore does not qualify as a characteristic species of $UAZ_1$; only its association with *Nv. pingdingshanensis* (Fig. 5) is indicative of the late Smithian $UAZ_1$.

*$UAZ_2$*

*Content. Hadrodontina aequabilis*, *Nv. pingdingshanensis*, *Nv.* ex gr. *abruptus*.

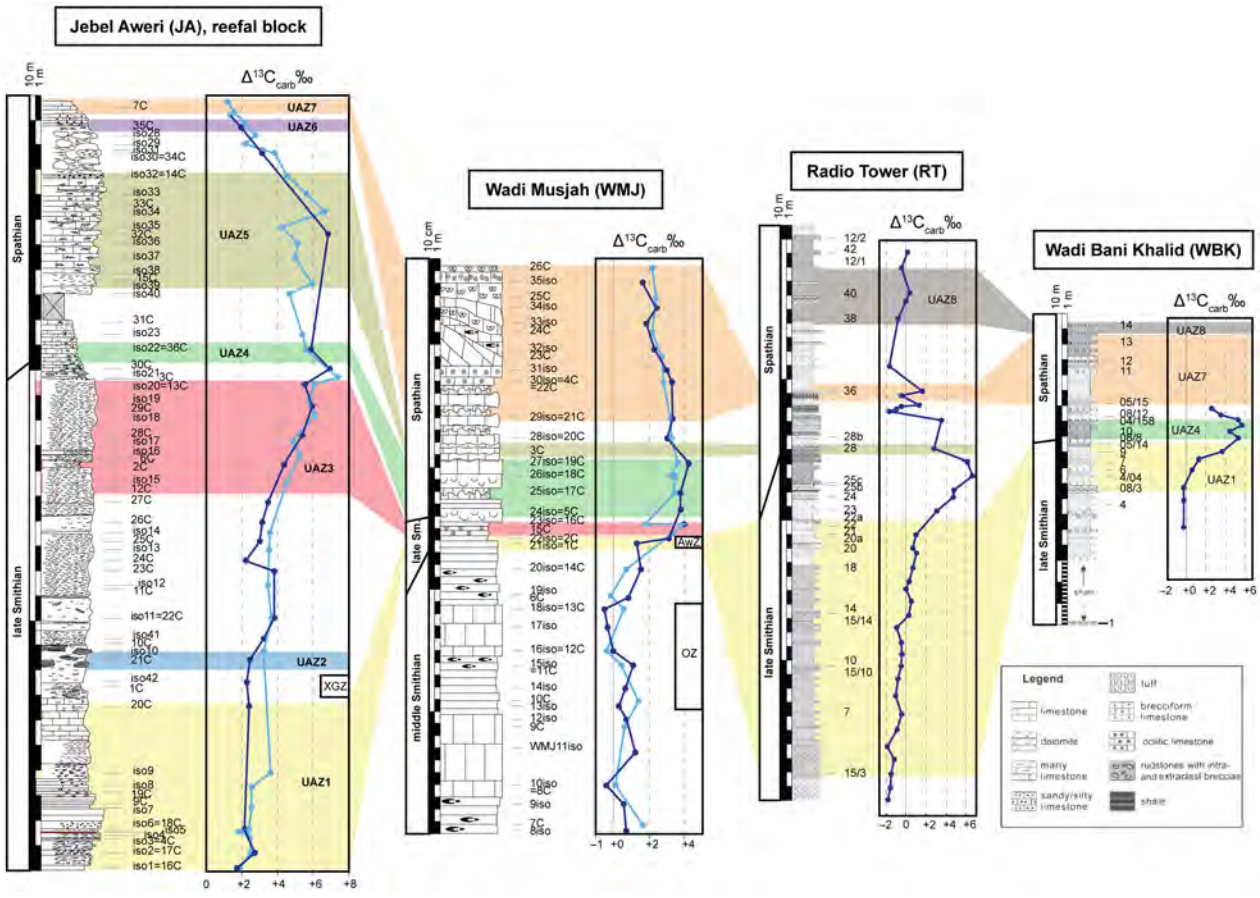


**FIG. 6.** Biostratigraphical correlations and comparison with the position of the unitary association zones (UAZs) in the studied sections Jebel Aweri, Wadi Musjah, Radio Tower and Wadi Bani Khalid. The lithological units are indicated and represented from the middle Smithian to the middle Spathian. Note the ammonoid zones recorded from Jebel Aweri and Wadi Musjah for intercalibration with the UAZs. *Abbreviations*: AwZ, *Anasibirites–Wasatchites* Zone; OZ, *Owenites* Zone; XGZ, *Xenoceltites–Glyptophiceras* Zone.

*Age.* Late Smithian.

*Geographical distribution in Oman.* Jebel Aweri.

*Characteristic pair of species. Hadrodontina aequabilis* with *Nv.* ex gr. *abruptus*.

*Comment.* $UAZ_2$ is recognized only in Jebel Aweri. However, it is retained because Jebel Aweri is the most expanded late Smithian to early Spathian section, worldwide.

*$UAZ_3$*

*Content. Novispathodus pingdingshanensis*, *Nv.* ex gr. *abruptus*, *Nv. praebrevissimus*, *Magnigondolella mutata*, *Borinella buurensis*, *Mg.*? sp. *A*.

*Age.* Latest Smithian.

*Geographical distribution in Oman.* Jebel Aweri, Wadi Musjah.

*Characteristic species. Novispathodus praebrevissimus*.

*$UAZ_4$*

*Content. Novispathodus pingdingshanensis*, *Nv.* ex gr. *abruptus*, *Mg. mutata*, *Bo. buurensis*, *Mg.*? sp. A, *Ic. zaksi*, *Ic. crassatus*, *Tr. symmetricus*.

*Age.* Earliest Spathian.

*Geographical distribution in Oman.* Jebel Aweri, Wadi Musjah, Wadi Bani Khalid.

*Characteristic pairs of species. Novispathodus pingdingshanensis* with either *Ic. zaksi*, *Ic. crassatus* or *Tr. symmetricus*.

$UAZ_5$

*Content. Novispathodus* ex gr. *abruptus*, *Mg. mutata*, *Bo. buurensis*, *Mg.*? sp. A, *Ic. zaksi*, *Ic. crassatus*, *Tr. symmetricus*, *Bo.*? sp. B, *Nv.* sp. Z, *Tr. homeri*.

*Age.* Early Spathian.

*Geographical distribution in Oman.* Jebel Aweri, Wadi Musjah, Radio Tower.

*Characteristic species. Borinella*? sp. B.

*Characteristic pairs of species.* Either *Mg. mutata*, *Bo. buurensis* or *Ic. zaksi* with either *Nv.* sp. Z or *Tr. homeri*.

*$UAZ_6$*

*Content. Novispathodus* ex gr. *abruptus*, *Mg.*? sp. A, *Ic. crassatus*, *Tr. symmetricus*, *Nv.* sp. Z, *Tr. homeri*, *Nv. brevissimus*, *Spathicuspus spathi*.

*Age.* Early Spathian.

*Geographical distribution in Oman.* $UAZ_6$ is identified only in Jebel Aweri.

*Characteristic pairs of species. Novispathodus* sp. Z with either *Nv. brevissimus* or *Sp. spathi*.

*$UAZ_7$*

*Content. Novispathodus* ex gr. *abruptus*, *Mg.*? sp. A, *Ic. crassatus*, *Tr. symmetricus*, *Tr. homeri*, *Nv. brevissimus*, *Sp. spathi*, *Tr. pusillus*, *Tr. brochus*, *Ic. collinsoni*, *Aduncodina unicosta*, *Nv. tahoensis*.

*Age.* Early or middle Spathian.

*Geographical distribution in Oman.* Jebel Aweri, Wadi Musjah, Radio Tower, Wadi Bani Khalid, Jebel Safra.

*Characteristic species. Triassospathodus pusillus* and *Ad. unicosta*.

*Characteristic pairs of species. Magnigondolella*? sp. A or *Nv. brevissimus* with either *Tr. brochus*, *Ic. collinsoni* or *Nv. tahoensis*.

*Comment.* This highly laterally reproducible $UAZ_7$ is recognized in all investigated sections. It contains conodont species that evolved during the early Spathian and which range up into the middle Spathian (e.g. *Nv. brevissimus* or *Ic. crassatus*), as well as middle Spathian species such as *Ad. unicosta* or *Tr. pusillus* (e.g. Leu *et al.* 2022).

*$UAZ_8$*

*Content. Novispathodus* ex gr. *abruptus*, *Ic. crassatus*, *Tr. symmetricus*, *Tr. homeri*, *Sp. spathi*, *Tr. brochus*, *Ic. collinsoni*, *Nv. tahoensis*, *Nv. triangularis*.

*Age.* Middle? Spathian.

*Geographical distribution in Oman.* Radio Tower, Wadi Bani Khalid, Jebel Safra.

*Characteristic pair of species. Novispathodus triangularis* with *Ic. crassatus*.

*Comment.* The first occurrence of *Nv. triangularis* typically overlaps with the last occurrence of *Ic. crassatus* in $UAZ_8$. *Nv.* ex gr. *abruptus*, *Tr. symmetricus*, *Tr. homeri*, *Sp. spathi*, *Tr. brochus*, *Ic. collinsoni* and *Nv. tahoensis* are all long-ranging species known from associations younger than $UAZ_8$.

## DISCUSSION

### *Comparisons with other conodont-based biochronological schemes for the SSB*

Based on four sections from the Tethys region (two from Oman, one from Slovenia and one from South China), Chen *et al.* (2019) constructed a UA-based biozonation consisting of seven UAZs and proposed to place the SSB between their $UAZ_4$ and $UAZ_5$ (note that their UAZ numbering is distinct from ours). In their scheme, *Nv. pingdingshanensis*, *Borinella* aff. *buurensis* (not illustrated), *Neospathodus planus* and *Ns. robustus* are characteristic species of their latest Smithian $UAZ_4$ but only *Nv. pingdingshanensis* occurs in their Omani sections. Likewise, *Platyvillosus corniger* and *Pl. regularis* are the characteristic species of their earliest Spathian $UAZ_5$, but they occur only in Slovenia, not in Oman. Additionally, the association of *Neogondolella* ex gr. *jakutensis* and *Tr. symmetricus* is considered a characteristic pair of $UAZ_5$ but it is recognized only in the Radio Tower section. Also note that their understanding of *Ng.* ex gr. *jakutensis* is at variance with ours.

Furthermore, the presumably synchronous and global positive CIE that peaks near the SSB becomes diachronous if the Chen *et al.* (2019) biozonation is applied: it is in $UA_9$ at Radio Tower, in $UA_{5–6}$ at Wadi Bani Khalid,

and in $UA_{12}$ at Jiarong. In contrast, our biozonation is compatible with a synchronous peak of the positive CIE given that it occurs in $UAZ_4$ in Wadi Musjah and Wadi Bani Khalid and in the uncertainty interval between $UAZ_3$ and $UAZ_4$ in Jebel Aweri.

### *Facies*

The bioclastic nature and abundance of skeletal debris of the Hallstatt facies in Wadi Musjah indicate a shallower setting than the usual lime mud facies of slope settings from other sections such as Radio Tower or Wadi Bani Khalid (Chen *et al.* 2019). In the Wadi Musjah section, the small (millimetric) bivalve tests of the early biostromes (cycle 1B) suggests an ecologically stressed fauna, possibly associated with the middle Smithian thermal maximum (Goudemand *et al.* 2019). However, post-mortem mechanical sorting cannot be excluded.

The Jebel Aweri section is the thickest (9 m) Early Triassic example of a continuous metazoan accumulation in a reef setting, although microbial activity is the main builder through sediment trapping and calcite precipitation. Synsedimentary cementation was important in the formation of a rigid boundstone framework and the stabilization of this Early Triassic build-up. Similar syndepositional concentric cement called 'evinosponges' is well known in younger, Middle–Upper Triassic (Russo *et al.* 2006) or Jurassic (Hoffmann *et al.* 2017) carbonate platforms.

### *Carbon isotopes*

As noted above, the difference of absolute values in the carbon isotopes between Wadi Musjah and Jebel Aweri probably reflects a difference in bathymetry. With a CAI of 1, Jebel Aweri and Wadi Musjah have apparently escaped significant thermal alteration. Absence of a siliciclastic fraction and of organic matter in these two well-oxygenated records is in agreement with the offshore setting interpretation. Therefore, these two sections are more likely to yield carbon isotope values representative of the Early Triassic open ocean, as opposed to records closer to the shelf.

Meyer *et al.* (2011) modelled the $\delta^{13}C$ depth profiles in the Panthalassa Ocean as a function of phosphate content. That study was based on a negative gradient of *c.* 4‰ from shallow to deep water settings as recorded in continental shelves from South China. The extrapolation of this gradient to the entire ocean led to the conclusion that the Early Triassic phosphate reservoir was threefold larger than the present day one. Meyer *et al.* (2011) and Shen *et al.* (2015) also suggested that the delayed recovery during the Early Triassic was a consequence of exceedingly high productivity and of widespread anoxic conditions.

In Oman, the two offshore seamounts represent shallow reef (Jebel Aweri) and slope/hemipelagic red limestones (Wadi Musjah). This difference in bathymetry is of the same order of magnitude as that documented in South China (Meyer *et al.* 2011; Shen *et al.* 2015). However, the offset between the two carbon isotope records from Oman is only 2‰, which is in agreement with the gradient of the present-day ocean (Hilting *et al.* 2008). The offshore $\delta^{13}C$ records reported here also exclude potential biases that may affect shelves in South China: (1) thermal alteration of the samples; (2) increased nutrient fluxes (e.g. phosphate) derived from continental weathering; (3) variations in terrestrial bio-productivity and burial of terrestrial organic matter; (4) larger fluctuations of seawater temperature in marginal basins; and (5) other effects linked with continental runoff and precipitation of inorganic carbon. Hence, the 2‰ offset between Jebel Aweri and Wadi Musjah highlights the fact that the $\delta^{13}C$ depth gradient was not uniform and that it was more pronounced on continental shelves.

Re-invigorated upwelling is another mechanism that has been invoked for the increasing organic carbon burial on continental shelves in conjunction with climatic cooling during the late Smithian (e.g. Song *et al.* 2013, 2019; Clarkson *et al.* 2016). However, the high-resolution time frame provided by Widmann *et al.* (2020) indicates that the onset of back shale deposition pre-dates the latest Smithian cooling.

In addition, Rock-Eval analyses of organic matter from the late Smithian black shales of an SSB section in South China (Qiakong) indicated that the existing organic matter was predominantly of terrestrial origin (Widmann *et al.* 2020). As quantitatively discussed by Widmann *et al.* (2020), an enhanced weathering of silicate rocks accompanied by an increasing flux of terrestrial organic matter is a favoured mechanism for the burial of organic matter in suboxic/anoxic continental shelves during the late Smithian. The coeval development of offshore bioclast-rich microbial boundstone reefs such as that of Jebel Aweri suggests that a pronounced lateral partitioning of the water masses occurred along the onshore–offshore gradient.

Some studies tried to explain the late Smithian diversity crisis of nektopelagic organisms by the simultaneous action of lethally warm surface waters and anoxic deep waters, which would have resulted in a very narrow mid-water refuge zone (Song *et al.* 2014). However, the timing of these two phenomena is not synchronous. Only the end of the thermal maximum overlapped with the onset of anoxia during the early late Smithian. Anoxic shelves persisted until the latest Smithian and the SSB, whereas

the onset of the 7–8°C cooling started in the middle of the late Smithian and extended into the early Spathian (Goudemand *et al.* 2019).

Finally, the correlation of the newly established conodont UAZs from Oman with the radioisotopically calibrated conodont UAZs from South China (Widmann *et al.* 2020) suggests that the onset on the late Smithian positive CIE was *c.* 400 kyr younger in the shallow water setting of Jebel Aweri than in all deeper water sections from South China and Oman. Although the onset of the positive late Smithian CIE is apparently diachronous, the peak of the shift appears to be synchronous in both offshore and shelf records, as can be inferred from the correlation of conodont UAZs. However, it should be noted that the maximum of the positive CIE may not be completed preserved on shelves that were affected by the SSB unconformity.

### *Conodonts across the SSB*

Previous studies suggested that as few as only two conodont species were recovered around the SSB crisis (Orchard 2007; Stanley 2009), indicating that this extinction was more deleterious to conodonts than the PTBME. For instance, the ellisonids, a major clade of conodonts surviving from the Permian, were among the main victims of the late Smithian extinction. Although the high sedimentation rate of Jebel Aweri has a clear dilution effect on conodont abundance, this problem could be compensated by collecting and processing larger samples (see Material and Method, above). Based on our rarefaction analysis (Fig. 7), most horizons appear to have been adequately sampled because their rarefaction curves level off.

In our Oman dataset, diversity of species and genera reached their lowest in $UAZ_2$, when the species turnover rate was at its lowest (Fig. 8). Four common species occur in both $UAZ_3$ and $UAZ_4$, thus crossing the SSB as defined here. A remarkable trait of this extinction is that although species and genus-level diversity were already recovering after $UAZ_2$, the number of Spathian subfamilies remained comparatively low from $UAZ_2$ to $UAZ_5$. The Spathian evolutionary radiation mainly proceeded at a low taxonomic level, predominantly within Novispathodinae and Neogondolellinae (Orchard 2007).

With the onset of the late Smithian extinction ($UAZ_1$), both conodonts and ammonoids distributions became largely cosmopolitan. The genus *Scythogondolella*, which was restricted to the boreal realm during the early and middle Smithian (Orchard 2008; Orchard & Zonneveld 2009), extended almost worldwide during $UAZ_1$, with the exception of a few places in the equatorial realm (e.g. Müller 1956; Matsuda 1984; Orchard 2008; Bondarenko *et al.* 2013; Maekawa *et al.* 2018; Liu *et al.* 2020). Similar cosmopolitanism can be observed with *Hadrodontina aequabilis* during the late Smithian and *Novispathodus pingdingshanensis* (and its derivatives) from the latest Smithian to the earliest Spathian (e.g. Koike 2016; Zhang *et al.* 2019). It is unclear whether this change toward cosmopolitan distributions was produced by the differential survival of opportunistic taxa (larger niche breadth, r-strategists (i.e. maximising reproductive capacity), low interspecies competition), or whether certain abiotic factors forced conodonts to migrate. Because of this increased cosmopolitanism, conodont biozones from South China and Oman can be easily correlated (Fig. S9). In both regions it is also clear that *Nv. pingdingshanensis* ranges from the late Smithian into the earliest Spathian, and that only the association of *Nv. pingdingshanensis* with *Ic. crassatus* can be used to identify the base of the Spathian. In comparison with South China, a higher resolution could be achieved in Oman with the construction of three additional UAZs around the SSB. This improved resolution largely results from the higher conodont diversity, in particular segminiplanate forms, and from more expanded sections in Oman.

The first occurrence of segminiplanate taxa in the shallow water Jebel Aweri section (in level B) supports the interpretation of a global late Smithian cooling (Goudemand *et al.* 2019) and the hypothesis that temperature rather than water depth is the critical parameter that controls the distribution of these forms (Carr *et al.* 1984; Orchard 1996; Lai *et al.* 2001; Joachimski *et al.* 2012; Leu *et al.* 2019; Chen *et al.* 2021). Furthermore, the segminiplanate genus *Gladigondolella* is here first recorded from the early Spathian in Wadi Musjah. This genus is classically known from cold water masses in lower latitudes during the Middle Triassic (Trotter *et al.* 2015). It is worth noting that this unusual early occurrence coincides with the coolest time interval around the SSB (Goudemand *et al.* 2012*a*, 2019).

Another feature of the Oman offshore Smithian–Spathian record is the larger size reached by each species compared with shelf records. For instance, *Nv. pingdingshanensis* yields a median size length of 0.3 mm, which is significantly larger (univariate, standard deviation $\delta = 0.0185$ mm, median = 0.217 mm) than its counterpart as documented by Leu *et al.* (2019) in Tulong (0.244 mm), Nammal (0.199 mm) and Guryul Ravine (0.217 mm) on the northern Indian Margin. Temporal size changes also tend to follow the same trend as established in the northern Indian Margin (Leu *et al.* 2019), but the general offset toward larger sizes in Oman remains unexplained. Plausible hypotheses include better oxygenated waters in offshore settings (e.g. Sheridan & Bickford 2011), cooler water temperatures (e.g. Bergmann 1847; Daufresne *et al.* 2009; Sheridan & Bickford 2011), and offshore migration of conodonts during their development (e.g. Armstrong & Dean 1996; Dingle & Drake 2007).

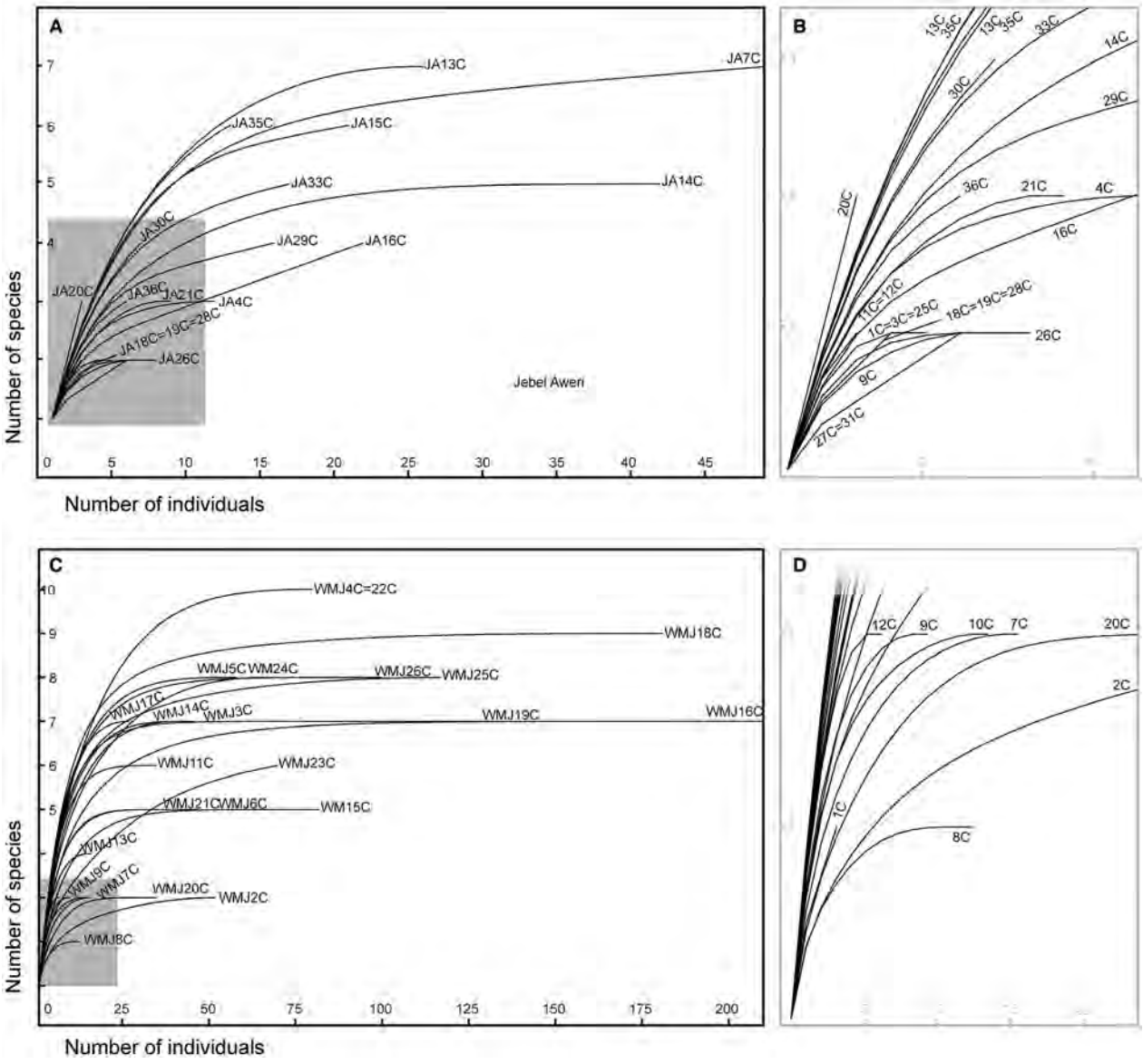


**FIG. 7.** Rarefaction curves for Jebel Aweri (JA) and Wadi Musjah (WMJ). A–B, Jebel Aweri; B, enlargement of the grey square in A. C–D, Wadi Musjah; D, enlargement of the grey square in C. Number of species is plotted as a function of the number of specimens for each sample. Note that the following samples were excluded from the rarefaction analysis: JA10C, JA17C and JA2C had no $P_1$ elements; in JA6C, JA22C, JA23C, JA24C, JA32C and JA34C, the maximum number of specimens per sample does not exceed five individuals.

## CONCLUSION

We have described in detail two offshore SSB sections from Oman, one of which (Jebel Aweri) is the most expanded SSB section known to date. This study addresses microfacies, the carbonate carbon isotope record, and the abundant and well-preserved conodont succession that enables the revision of several conodont taxa, definition of four new species, and the construction of a new and high-resolution late Smithian to early Spathian UAZ-based biochronological frame for Oman. Based on a dataset including four SSB sections in Oman, we produced eight robust and discrete conodont UAZs. These are intercalibrated with ammonoid biochronozones and the carbonate carbon isotope record. We propose to place the SSB between $UAZ_3$ and $UAZ_4$. A zone in South China correlated with $UAZ_4$ contains the earliest tirolitids indicative of a basal Spathian age (Galfetti *et al.* 2007*a*). In this scheme, *Nv. pingdingshanensis* ranges throughout the

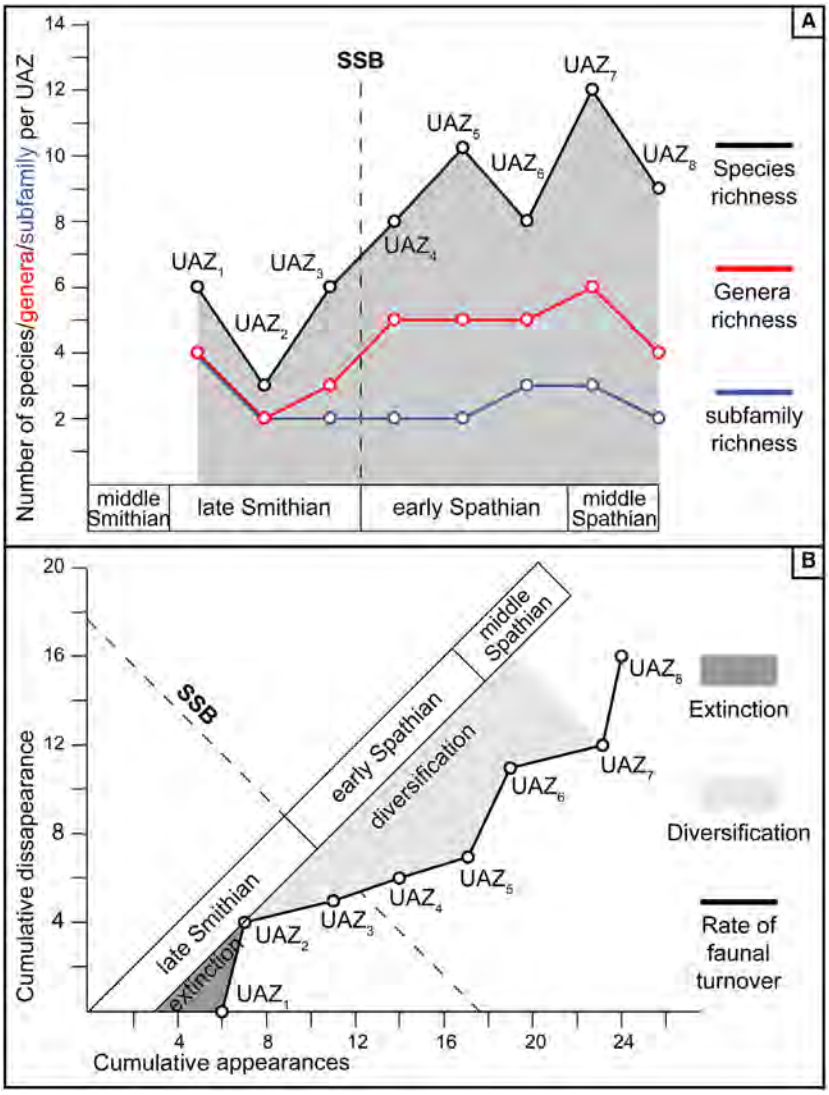


**FIG. 8.** A, temporal evolution (succession of UAZs) of the conodont faunal turnover. B, species diversity for all the conodont species from Oman during the Smithian and Spathian interval that are included in the UAZ. Calculated from the optimal solution given in Figure 5. Note the late Smithian extinction and early Spathian radiation on the species. *Abbreviations*: SSB, Smithian–Spathian boundary; UAZ, unitary association zone.

SSB and only the association of *Nv. pingdingshanensis* with *Ic. crassatus* can be used to unambiguously characterize the base of the Spathian. Moreover, typical Spathian taxa (*Ic. crassatus* and *Tr. symmetricus*) first occur in the Omani $UAZ_4$ and its correlated zone in South China. A correlated zone of the youngest late Smithian $UAZ_3$ from Oman is typically missing in many South Chinese SSB sections, where the equivalent time interval is truncated by a widespread unconformity.

In Jebel Aweri and Wadi Musjah, where neither facies nor conodont biochronology show a hiatus around the SSB, the peak of the positive CIE stretches from the separation interval that contains the SSB to the end of the basal Spathian $UAZ_4$. The 2‰ offset in $\delta^{13}C_{carb}$ values documented between Wadi Musjah and Jebel Aweri probably reflects the different bathymetry of these sections. The Oman offshore record shows no evidence of anoxia and suggests that such conditions were restricted to continental shelves under the influence of enhanced weathering and terrestrial clastic fluxes.

## SYSTEMATIC PALAEONTOLOGY

*by* Marc Leu *and* Nicolas Goudemand

Synonymies are limited to key citations and illustrations. All illustrated specimens are shown at the same scale. Many species descriptions are based on the $P_1$ element only. All figured specimens are located and stored in the Paleontological Institute and Museum of the University of Zurich (PIMUZ), Karl-Schmid-Strasse 4, 8006 Zürich, Switzerland. Supragenus-level classification mostly follows Donoghue *et al.* (2008) and Orchard (2005). The terminology for the orientation of the element is the traditional one based on the orientation and curvature of the cusp. It

refers only to the element itself and not its natural orientation in the animal (Purnell *et al.* 2000). 'Lower' refers to the side of the element from which the basal cavity opens. 'Upper' refers to the opposite side. The term 'cusp' refers only to the cusp *s.s.* (Klapper & Philip 1972).

## Class CONODONTA Eichenberg, 1930
## Division PRIONIODONTIDA Dzik, 1976
## Order OZARKODINIDA Dzik, 1976
## Superfamily GONDOLELLOIDAE Lindström, 1970
## Family GONDOLELLIDEA Lindström, 1970
## Subfamily NOVISPATHODINAE Orchard, 2005
## Genus NOVISPATHODUS Orchard, 2005

Several of the following species were originally assigned to *Neospathodus*. Because *Nv. waageni* and *Nv. pingdingshanensis* have been reconstructed as having a *Novispathodus* apparatus and the latter is considered as the rootstock of most Spathian segminate forms, we assume that most early Spathian segminate species possessed a *Novispathodus* apparatus instead. Validation of these genus-level assignments via multielement reconstructions or natural assemblages is still pending. Similarly, some early Spathian $P_1$ elements have been assigned herein to genera such as *Triassospathodus* or *Icriospathodus* on the basis of their resemblance to the $P_1$ of those genera, and hence a presumed close affinity. However, the remainder of their respective apparatuses is hitherto unknown and the S and M elements may have evolved at a different pace than the $P_1$: in other words, some of the corresponding early Spathian species may have possessed a *Novispathodus* apparatus still. If the P elements are *Triassospathodus*- or *Icriospathodus*-like, but the S-M array is more *Novispathodus*-like, it would constitute a new genus. Given that the latter is unknown for early Spathian forms to date, we tentatively assign these forms to *Novispathodus*.

### *Novispathodus* ex gr. *abruptus* (Orchard, 1995)
Figures 9J, K; 10B

1981 *Neospathodus homeri* Bender; Koike, pl. 1, fig. 5
1984 *Neospathodus* sp. A; Hatleberg & Clark, pl. 3, fig. 8, 21.
*1995 *Neospathodus abruptus* Orchard, p. 118, 119, figs 3.16–3.19, 3.23–3.26.
2005 *Novispathodus abruptus* (Orchard); Orchard, p. 90, text-fig. 16
2009 *Novispathodus abruptus* (Orchard); Orchard & Zonneveld, p. 784, fig. 15 parts 34–37.
2012*a* *Novispathodus* sp. nov. A; Goudemand & Orchard *in* Goudemand *et al.*, p. 1031, fig. 2A, R?, Z?
2012*a* *Novispathodus* sp. nov. B; Goudemand & Orchard *in* Goudemand *et al.*, p. 1031, fig. 3V.
2018 *Novispathodus abruptus* (Orchard); Maekawa *in* Maekawa *et al.*, p. 33, fig. 18.1–18.3, 18.20, 18.23, 18.24, 18.26, 18.27 (only).

*Material.* 50 specimens.

*Remarks.* The specimens illustrated here show similar morphologies to the holotype (fig. 3.23, 3.24) described by Orchard (1995). The specimens in China (Leu *et al.* 2022) are smaller than the Oman specimens.

*Occurrence.* Worldwide occurrence in upper Smithian and lower Spathian rocks. *Xenoceltites* and *Tirolites* beds in *Nv. pingdingshanensis* and *Nv. brevissimus* zones, Japan (Koike 1981; Maekawa *et al.* 2018). Oman (Orchard 1995). British Columbia (Orchard & Zonneveld 2009), South China (Goudemand *et al.* 2012*a*; Leu *et al.* 2022).

### *Novispathodus pingdingshanensis* (Zhao & Orchard *in* Zhao *et al.*, 2007)
Figures 10G, K–M, P; 11G; 12C

*2007 *Neospathodus pingdingshanensis* Zhao & Orchard; Zhao *et al.*, p. 36, pl. 1, fig. 4A–C.
2012*a* *Novispathodus pingdingshanensis* (Zhao & Orchard); Goudemand & Orchard *in* Goudemand *et al.*, pp. 1030–1031, figs 2B, F, G, I, J, M, P, Q, AD, 3T–U, 6.
2013 *Neospathodus pingdingshanensis* Zhao & Orchard; Chen *et al.*, p. 825, fig. 3.10–12.
2013 *Neospathodus waageni* subsp. nov. A; Metcalfe *et al.*, p. 1144, figs 9.1–5, 9.7, 9.8, 9.10.
2014 *Novispathodus pingdingshanensis* (Zhao & Orchard); Maekawa & Igo *in* Shigeta *et al.*, pp. 239–240, figs 171.13–31.
2015 *Novispathodus pingdingshanensis* (Zhao & Orchard); Chen *et al.*, pp. 111–112, figs 7.1–4, 8.5–6.
2016 *Novispathodus* ex. gr. *pingdingshanensis* (Zhao & Orchard); Komatsu *et al.*, p. 69, figs 5.4a–5.5c.
2016 *Neospathodus robustus* Koike; Chen & Kolar-Jurkovšek *in* Chen *et al.*, p. 93, fig. 9.5 (only).
2018 *Novispathodus pingdingshanensis* (Zhao & Orchard); Maekawa *in* Maekawa *et al.*, pp. 36–37, figs 20.2–18, 21.1–13.
2019 *Novispathodus pingdingshanensis* (Zhao & Orchard); Chen *et al.*, fig. 3 nr. 8.
2020 *Novispathodus pingdingshanensis* (Zhao & Orchard); Liu *et al.*, p. 13, pl. 3 fig. 5 (only).

*Material.* 70 specimens

*Remarks.* Most of the specimens of *Nv. pingdingshanensis* from Oman resemble the holotype of *Nv. pingdingshanensis s.s.* with recurved denticles and a relatively large basal cavity. As noted by Goudemand (*in* Goudemand *et al.* 2012*a*) the basal margin may vary between being straight or slightly upturned posteriorly. The specimen shown in Figure 10G is relatively shorter with more erect denticles than the holotype but falls within the intraspecies variation. It might represent a transitional form between *Nv. pingdingshanensis* and *Nv. praebrevissimus*.

*Occurrence.* Worldwide occurrence around the Smithian–Spathian boundary.

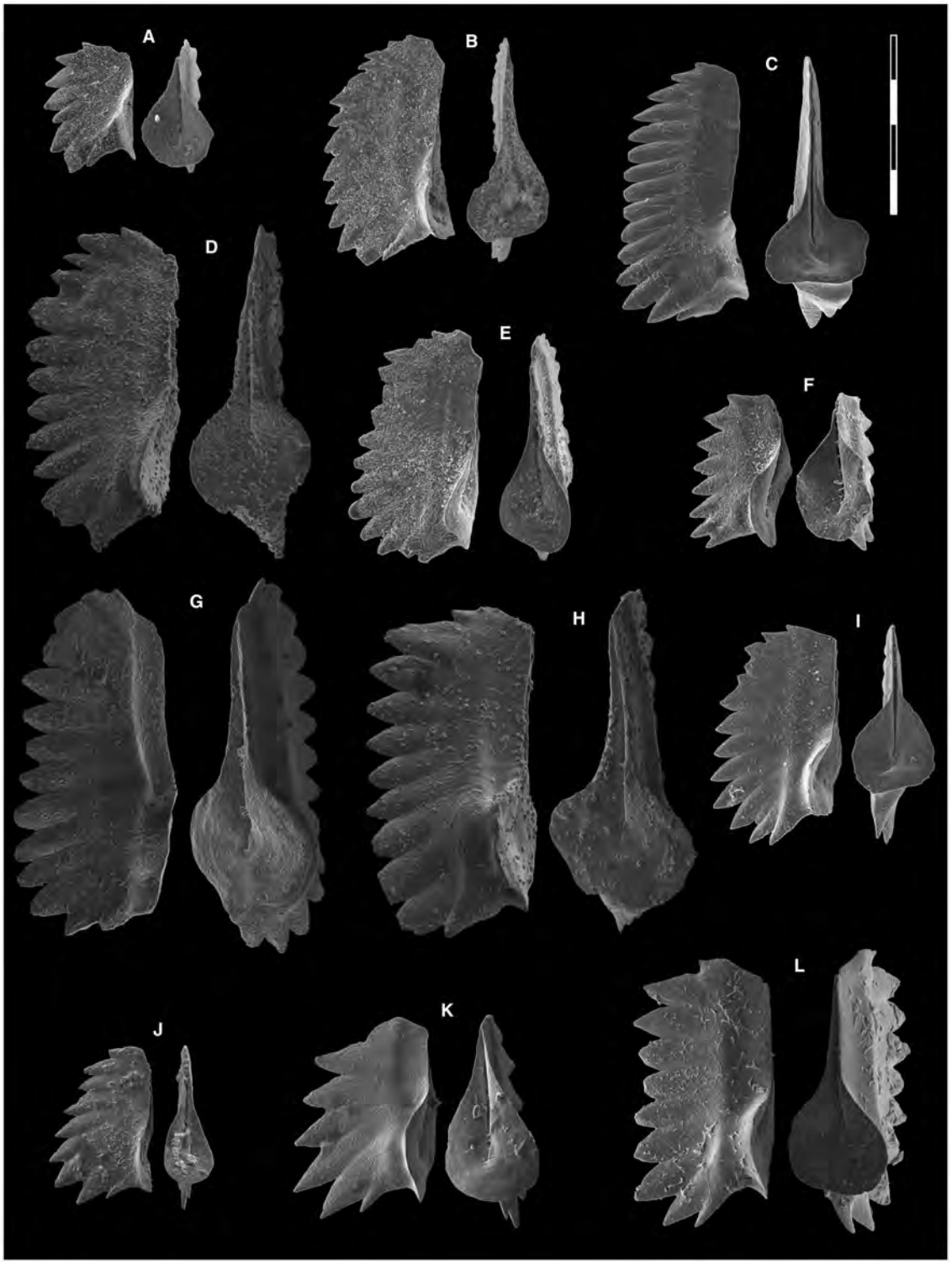


**FIG. 9.** A, *Triassospathodus* aff. *symmetricus* (Orchard); WMJ16C, PIMUZ 38915. B, *Triassospathodus homeri* (Bender); WMJ20C, PIMUZ 38927. C, D, G–I, L, *Icriospathodus crassatus* (Orchard): C, WMJ22C, PIMUZ 38858; D, JA14C, PIMUZ 38859; G, JA14C, PIMUZ 38860; H, JA14C, PIMUZ 38861; I, (juvenile?) WMJ3C, PIMUZ 38865; L, JA33C, PIMUZ 38864. E, *Triassospathodus symmetricus* (Orchard): WMJ3C, PIMUZ 38932. F, *Icriospathodus zaksi* (Buryi); WMJ17C, PIMUZ 38872. J–K, *Novispathodus* ex gr. *abruptus* (Orchard): J, JA21C, PIMUZ 38891; K, JA13C, PIMUZ 38892. Scale bar represents 400 μm. All specimens are $P_1$ elements if not otherwise specified. The orientation is standardized with the anterior side to the top and the denticle tips to the left in 'lateral' view.

### *Novispathodus robustispinus* (Zhao & Orchard *in* Zhao *et al.*, 2008)
Figures 10O, 11C

2008 *Neospathodus robustispinus* Zhao & Orchard *in* Zhao *et al.*, p. 213, pl. 1, fig. 5.

*Material.* 5 specimens

*Remarks.* The Omani material resembles the holotype from Chaohu, China (Zhao *et al.* 2008). Our impression from the illustration of the holotype is that its anterior end may be broken. Chen *et al.* (2016) assigned several specimens from the middle Spathian in Slovenia to *Nv. robustispinus*, but their illustrated specimens lack the posterior accessory denticle or bump, their carina is higher and the denticles not as wide and fused.

*Novispathodus robustispinus* most resembles *Nv. praebrevissimus* but its denticulation differs in having fewer wide denticles. Specimens of *Nv. praebrevissimus* are also relatively shorter.

*Occurrence.* JA13C, Jebel Aweri, Batain, Oman (this study), *Columbites–Tirolites* zone, Nanlinghu Formation, Lower Triassic, Chaohu, China (Zhao *et al.* 2008).

### *Novispathodus praebrevissimus* Leu & Goudemand *in* Leu *et al.*, 2022
Figure 11A, B?, D–H, P

1984 *Neospathodus* sp. aff. *triangularis* Bender; Hatleberg & Clark, pl. 3, fig. 16.
2014 *Icriospathodus*? *zaksi* (Buryi); Maekawa & Igo *in* Shigeta *et al.*, fig. 192 nr. 10–13 (only).
2015 *Novispathodus brevissimus* (Orchard); Chen *et al.*, p. 111, fig. 7.8.
2019 *Novispathodus pingdingshanensis* (Zhao & Orchard); Chen *et al.*, fig. 3 nr. 5, 9 (only) fig. 5 nr. 6 (only)
2020 *Novispathodus pingdingshanensis* (Zhao & Orchard); Liu *et al.*, p. 13, pl. 3, fig. 7 (only)

*Material.* 35 specimens

*Remarks.* This species is thought to be intermediate between *Nv. pingdingshanensis* and *Nv. brevissimus*. The $P_1$ element of this species is very similar to that of *Nv. pingdingshanensis* but the basal cavity is much larger and rounded. Compared with *Nv. brevissimus*, this species is usually smaller and has a relatively larger and more rounded basal cavity. Furthermore, the carina is lower, with less numerous denticles. In contrast to that of *Nv. praebrevissimus*, the $P_1$ element of *Neospathodus soleiformis* Zhao & Orchard is higher than wider, and that of *Ns. expansus* Zhao & Orchard is conspicuously thickened laterally.

*Occurrence.* Wadi Musjah (samples WMJ15C, WMJ16C) and Jebel Aweri (samples JA13C, JA28C, JA29C), Olenekian, Oman. South China (Leu *et al.* 2019)

### *Novispathodus* cf. *expansus* (Zhao & Orchard, 2008)
Figure 11Q

*2008 *Neospathodus expansus* Zhao & Orchard *in* Zhao *et al.*, p. 211, pl. 1, fig. 2a–c.
2022 *Novispathodus expansus* (Zhao & Orchard); Leu *et al.*, fig. 26U.

*Material.* 4 specimens

*Remarks.* The illustrated specimen is laterally thickened, has a broadly expanded, subcircular basal cavity, and strongly resembles the holotype of '*Neospathodus*' *expansus*, but it is broken anteriorly, hence the 'cf'.

*Occurrence. Columbites–Tirolites* Zone, Nanlinghu Formation, Lower Triassic, Chaohu, Anhui Province, China (Zhao *et al.* 2008); sample, JA15C, Jebel Aweri, Batain, early Spathian age, Oman (this study).

### *Novispathodus brevissimus* (Orchard, 1995)
Figure 11I–O

1981 *Neospathodus triangularis* Bender; Koike, pl. 1, fig. 6.
*1995 *Neospathodus brevissimus* Orchard, pp. 117, pl. 3, figs 14–15, 20–22.
2011 *Neospathodus brevissimus* Orchard; Ji *et al.*, p. 219, fig. 3 nr. 7.
2014 *Novispathodus triangularis* (Bender); Maekawa & Igo *in* Shigeta *et al.*, pp. 241–243, figs 172.1–9, 172.13–27, 173.1–3, 173.6–12, 173.16–21, 173.28–44, 174.1–174.24.
2015 *Triassospathodus brevissimus* (Orchard); Yan *et al.*, p. 240, fig. 3.4.
2016 *Novispathodus triangularis* (Bender); Komatsu *et al.*, p. 69, fig. 5.8.
2018 *Novispathodus brevissimus* (Orchard); Maekawa *in* Maekawa *et al.*, p. 34, fig. 19.4, 19.5, 19.7.
2019 *Neospathodus curtatus* Orchard; Chen *et al.*, fig. 6 nr. 13, 14.
2019 *Neospathodus brevissimus* Orchard; Chen *et al.*, fig. 6 nr. 15.
2019 *Triassospathodus brevissimimus* [sic.] (Orchard); Wu *et al.*, fig. 4 nr. 36.
2020 *Novispathodus brevissimus* (Orchard); Liu *et al.*, p. 14, pl. 4, figs 15, 18.

*Material.* 80 specimens.

*Remarks.* In the material from Wadi Musjah, both small (e.g. Fig. 11M) and large (Fig. 11O) specimens can be found. The holotype (GSC101638; Orchard 1995) more closely resembles the small specimens, suggesting that it may represent a juvenile form. The specimens Leu *et al.* (2022) illustrated from South China, in contrast, look like the large specimens from Oman.

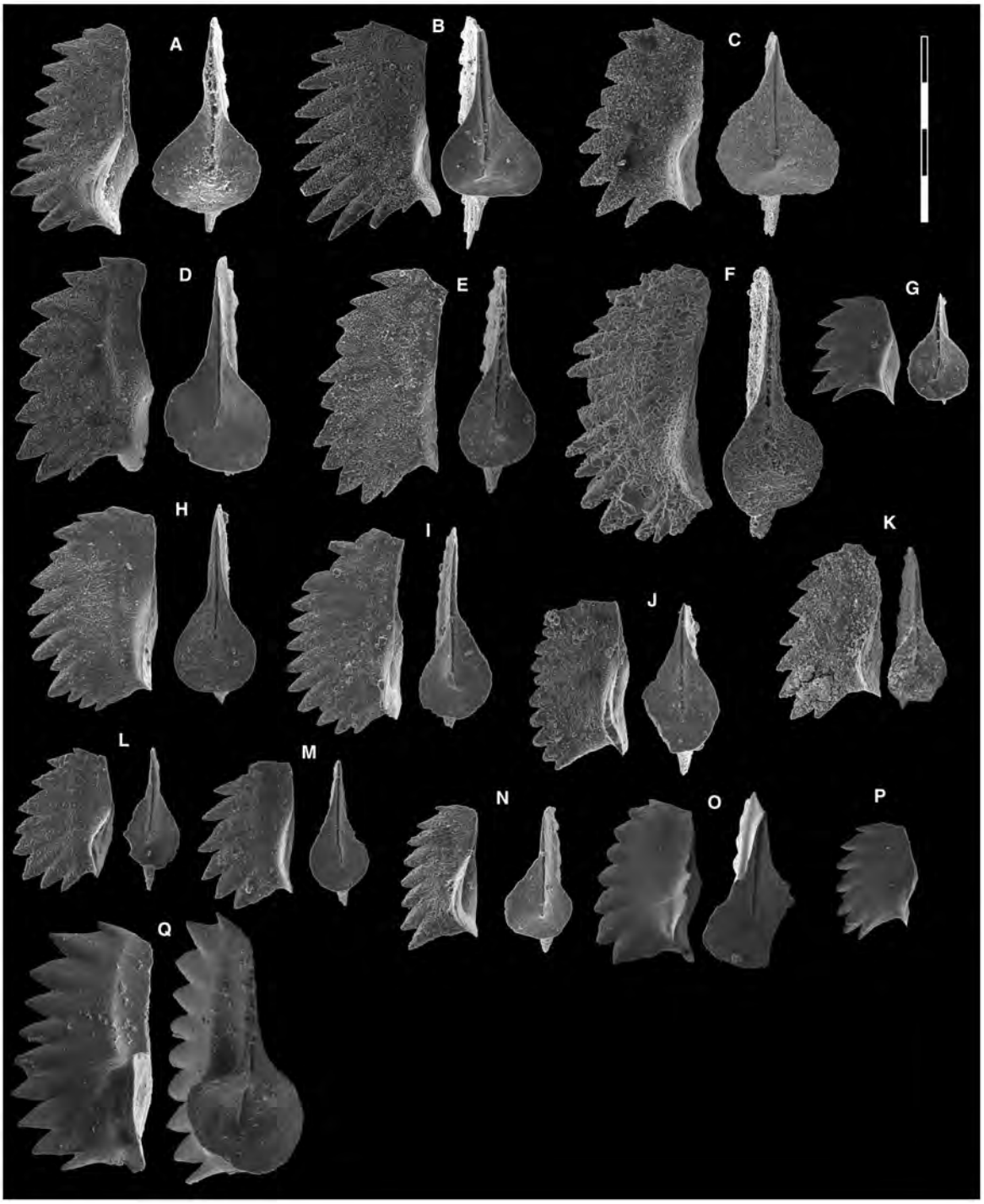


**FIG. 10.** A, Q, *Icriospathodus* zaksi (Buryi): A, WMJ18C, PIMUZ 38873; Q, JA33C, PIMUZ 38874. B, *Novispathodus* ex gr. *abruptus* (Orchard); WMJ18C, PIMUZ 38893. C–D, *Triassospathodus* aff. *symmetricus*? (Orchard); C, WMJ16C, PIMUZ 38916; D, WMJ18C, PIMUZ 38917. E–F, H–J, *Triassospathodus symmetricus* (Orchard): E, WMJ3C, PIMUZ 38933; F, WMJ4C, PIMUZ 38934; H, WMJ3C, PIMUZ 38935; I, WMJ3C, PIMUZ 38936; J, WMJ5C, PIMUZ 38937. G, K–M, P, *Novispathodus pingdingshanensis* (Zhao & Orchard): G, WMJ17C, PIMUZ 38895; K, WMJ19C, PIMUZ 38896; L, JA21C, PIMUZ 38897; M, JA21C, PIMUZ 38898; P, JA25C, PIMUZ 38899. N, *Triassospathodus* aff. *symmetricus* (Orchard); WMJ5C, PIMUZ 38918. O, *Novispathodus robustispinus* (Zhao & Orchard); JA13C, PIMUZ 38908. Original magnification ×80. Scale bar represents 400 μm. All specimens are $P_1$ elements if not otherwise specified. The orientation is standardized with the anterior side to the top and the denticle tips to the left in 'lateral' view.

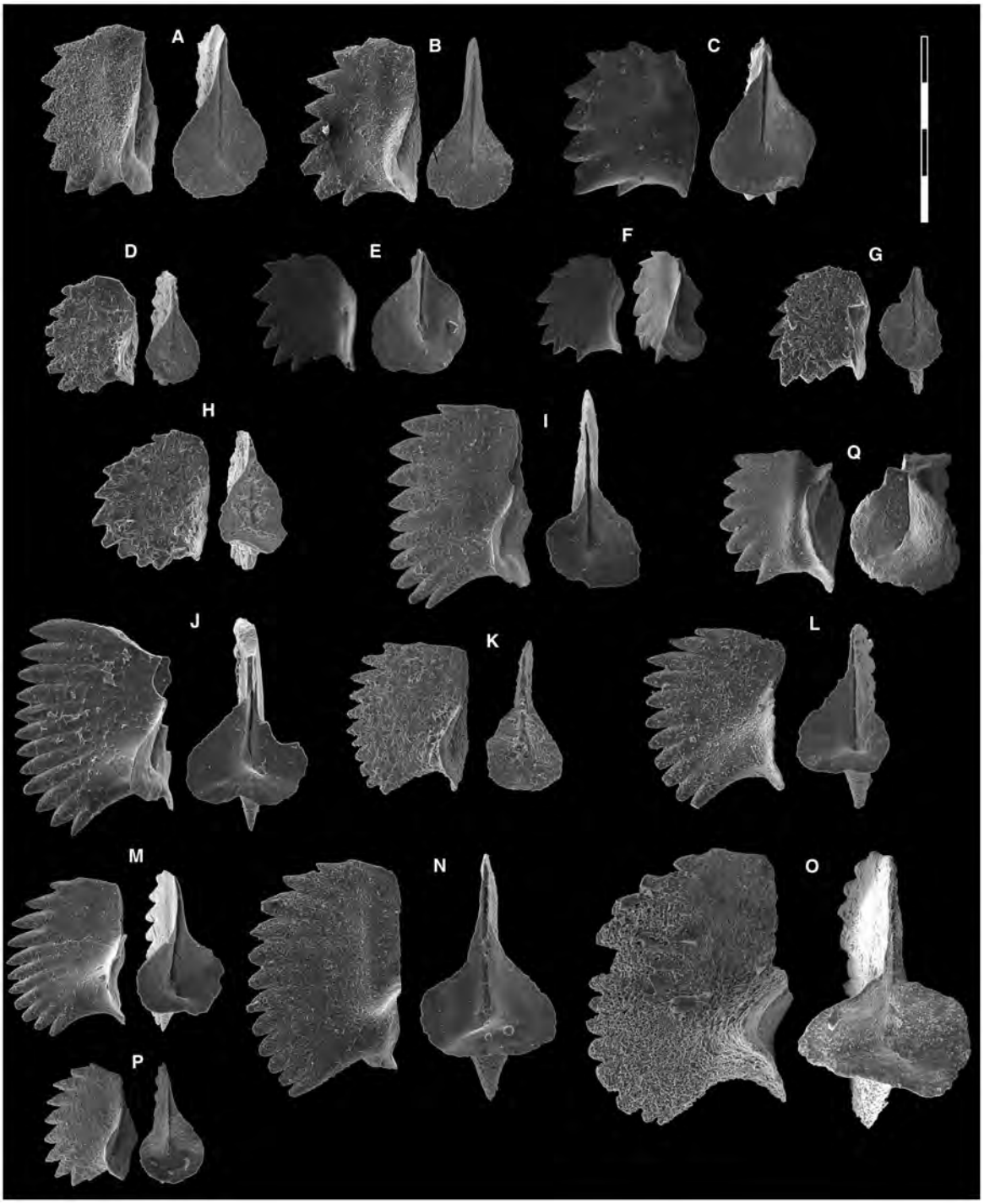


**FIG. 11.** A, B, D–F, H, P, *Novispathodus praebrevissimus* Leu & Goudemand: A, WMJ16C, PIMUZ 38900; B, WMJ16C, PIMUZ 38901; D, WMJ15C, PIMUZ 38902; E, JA29C, PIMUZ 38903; F, JA13C, PIMUZ 38904; H, WMJ15C, PIMUZ 38905; P, JA28C, PIMUZ 38906. C, *Novispathodus robustispinus* (Zhao & Orchard); JA13C, PIMUZ 38907. G, *Novispathodus pingdingshanensis* (Zhao & Orchard); WMJ15C, PIMUZ 38894. I–O, *Novispathodus brevissimus* (Orchard): I, WMJ22C, PIMUZ 38883; J, WMJ22C, PIMUZ 38884; K, WMJ24C, PIMUZ 38885; L, WMJ23C, PIMUZ 38886; M, WMJ23C, PIMUZ 38887; N, WMJ23C, PIMUZ 38888; O, WMJ21C, PIMUZ 38889. Q, *Novispathodus* cf. *expansus* (Zhao & Orchard); JA15C, PIMUZ 38890. Original magnification ×80. Scale bar represents 400 μm. All specimens are $P_1$ elements if not otherwise specified. The orientation is standardized with the anterior side to the top and the denticle tips to the left in 'lateral' view.

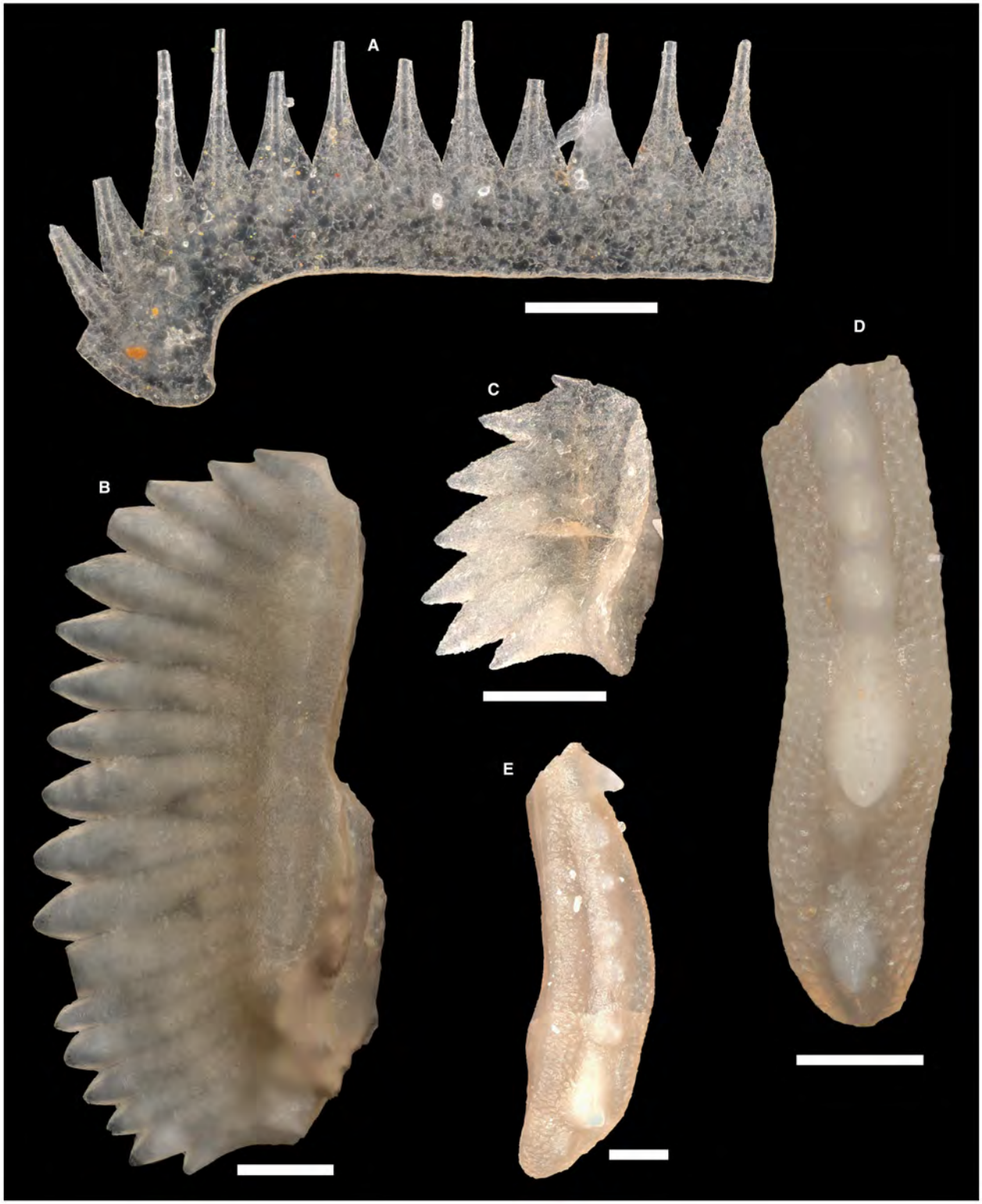


**FIG. 12.** A, indet. sp. A *sensu* Orchard *et al.* (2007*a*); JA7C, 38 875. B, *Triassospathodus symmetricus* (Orchard); JA7C, PIMUZ 38938. C, *Novispathodus pingdingshanensis* (Zhao & Orchard); WMJ17C, PIMUZ SQL54628. D–E, *Gladigondolella tethydis* (Huckriede): D, WMJ17C, PIMUZ 38847; E, WMJ17C, PIMUZ 38848. All scale bars represent 100 μm. All specimens are $P_1$ elements if not otherwise specified. The orientation is standardized with the anterior side to the top and the denticle tips to the left in 'lateral' view. Images were obtained using a Keyence VHX 6000 digital microscope.

*Occurrence.* Wadi Musjah (samples WMJ4C, WMJ21C-WMJ26C) and Jebel Aweri (JA 35C) in this study. This is a cosmopolitan species during the early Spathian.

## Genus ICRIOSPATHODUS Krahl *et al.*, 1983

*Type species and holotype.* *Neospathodus collinsoni* Solien, 1979.

*Type stratum & locality.* Unit D, Thaynes Formation, near Salt Lake City, Utah, USA.

*Remarks.* *Icriospathodus* specimens from Oman tend to show a relatively higher carina than congeneric specimens from other regions (e.g. South China; Leu *et al.* 2022).

### *Icriospathodus zaksi* (Buryi, 1979)
Figures 9F; 10A, Q; 13A–D, F, G

*1979 *Neospathodus zaksi* Buryi, p. 60 pl. 18 figs 3a, b.
2007 *Icriospathodus*? *zaksi* (Buryi); Orchard, fig. 2.
2013 *Neospathodus novaelhollandiae* McTavish; Yan *et al.*, p. 516, fig. 6BB–DD.
2014 *Icriospathodus*? *zaksi* (Buryi); Maekawa & Igo *in* Shigeta *et al.*, fig. 192 nr. 14–29.
2015 *Novispathodus pingdingshanensis* (Zhao & Orchard); Chen *et al.*, p. 111, fig. 7.1–7.2.
2016 *Neospathodus planus* sp. nov. Chen & Kolar-Jurkovšek; Chen *et al.*, p. 92, fig. 7.9a–c, 8.10.
2016 *Neospathodus robustus* Koike; Chen & Kolar-Jurkovšek *in* Chen *et al.*, p. 92, figs 8.7–8.9.
2016 *Icriospathodus*? *zaksi* (Buryi); Komatsu *et al.*, p. 69, fig. 5 nr. 2–3.
2018 *Icriospathodus zaksi* (Buryi); Henderson *et al.*, p. 18 pl. 1 fig. 18–19.
2018 *Icriospathodus zaksi* (Buryi); Maekawa *in* Maekawa *et al.*, p. 51, figs 29.20–29.26.
2018 *Icriospathodus*? sp. 1; Maekawa *in* Maekawa *et al.*, p. 54, figs 30.1–30.2.
2019 *Triassospathodus symmetricus* (Orchard); Chen *et al.*, fig. 5 nr. 8 (only)
2019 *Neospathodus* ex. gr. *planus* Chen & Kolar-Jurkovšek; Chen *et al.*, fig. 6 nr. 2.
2019 *Icriospathodus zaksi* (Buryi); Chen *et al.*, fig. 6 nr. 4, fig. 7 nr. 9, 10.
2020 *Novispathodus pingdingshanensis* (Zhao & Orchard); Liu *et al.*, p. 13, pl. 3, fig. 4 (only).

*Material.* 50 specimens

*Remarks.* The $P_1$ of this species differs from that of *Ic. crassatus* (and *Ic.* aff. *crassatus* Leu & Goudemand *in* Leu *et al.*, 2022) by its relatively larger basal cavity. The specimens of *Ic. zaksi* found in Oman (Chen *et al.* 2019; this study) appear to be generally larger than conspecific specimens from other Tethyan localities (e.g. Guryul Ravine and China; Leu *et al.* 2022 and personal collection of Guryul Ravine conodonts), suggesting that favourable local environmental factors or lifecycle migrations may have played a role.

*Occurrence.* Wadi Musjah (samples WMJ5C, WMJ17C, WMJ18C), lower Spathian, Hawasina Nappes, Oman.

### *Icriospathodus crassatus* (Orchard, 1995)
Figures 9C, D, G, H, I(juvenile?), L; 13E, H–J; 14A, B

1987 *Neospathodus triangularis* Bender; Perri & Andraghetti, pl. 33, figs 1–5.
1987 *Neospathodus collinsoni* Solien; Zakharov & Rybalka, pl. 5, figs 4, 5.
1992 *Spathoicriodus collinsoni* Solien; Koike, fig. 12 nr. 1–12, 43, 45–46, 51–53, fig. 13 nr. 1–7.
*1995 *Neospathodus crassatus* Orchard, p. 120, fig. 2 nr.19, 25–27.
2007 *Icriospathodus? crassatus* Orchard; Orchard, fig. 2.
2007 *Icriospathodus collinsoni* Solien; Lucas & Orchard, fig. 7 nr. 13–15.
2011 *Neospathodus crassatus* Orchard; Ji *et al.*, fig. 4 nr. 2a–c.
2014 *Icriospathodus? crassatus* Orchard; Maekawa & Igo *in* Shigeta *et al.*, fig. 192 nr. 7–9.
2015 *Icriospathodus? crassatus* Orchard; Yan *et al.*, fig. 3 nr. 7.
2015 *Novispathodus ? crassatus* Orchard; Lehrmann *et al.*, fig. 5 nr. 16, 17.
2015 *Icriospathodus crassatus* Orchard; Chen *et al.*, fig. 9.12.
2018 *Icriospathodus crassatus* Orchard; Maekawa *in* Maekawa *et al.*, p. 52, figs 29.8–29.19.
2019 *Icriospathodus crassatus* Orchard; Chen *et al.*, fig. 5 nr. 5, fig. 6 nr. 7 (only).
2020 *Icriospathodus crassatus* Orchard; Liu *et al.*, p. 14, pl. 4, figs 10, 14.
2021 *Triassospathodus homeri* Bender; Chen *et al.*, fig. 4 nr. 14–16.

*Material.* >50 specimens

*Remarks.* Our specimens fit well in the original description of this species by Orchard (1995), whose material was also from Oman, although some seem to have a relatively larger basal cavity than that illustrated by Orchard. Some elements (e.g. Fig. 13D) also superficially resemble the paratype of *Nv. abruptus* (Orchard 1995, figs 3.25–26) but differ in having lower, blunter denticles that are more reminiscent of those found in representatives of *Icriospathodus*. A platform flange is sometimes present, particularly posteriorly.

*Occurrence.* Oman: Wadi Musjah (samples WMJ3C, WMJ19C, WMJ22C, WMJ24C), Hawasina Nappes lower Spathian; Jebel Aweri (JA 14C, JA 22C, Batain, lower Spathian, sample RT28, $UAZ_5$), Radio Tower section (Chen *et al.* 2019); Jebel Safra (Orchard 1995). This species can be found in several localities worldwide

### *Icriospathodus collinsoni* (Solien, 1979)
Figure 13K–M

1964 *Icriodus*; Clark *et al.*, p. 376, pl. 60, fig. 1.
1970 *Neospathodus* sp. G; Hasenmüller, pp. 45–47, pl. 2, fig. 12a–b.
1971 *Neospathodus* sp. G; Sweet *et al.*, p. 453, pl. 1, figs 12, 13.
*1979 *Neospathodus collinsoni* Solien, p. 302, pl. 3, figs 10, 12–20.
1981 *Neospathodus*? *collinsoni* Solien; Koike, pl. 1, figs 42–44.
1987 *Neospathodus collinsoni* Solien; Zakharov & Rybalka, pp. 43–44, pl. 5, figs 4, 5.
1990 *Neospathodus collinsoni* Solien; Metcalfe, p. 136, pl. 1, figs 6, 7, 17.
1992 *Spathoicriodus collinsoni* (Solien); Koike, pp. 357–361, figs 11, 12.13–12.42, 12.44, 12.47–12.50, 13.8–13.37.
1995 *Icriospathodus collinsoni* (Solien); Orchard, p. 113, fig. 2.22–2.24.
2005 *Icriospathodus collinsoni* (Solien); Orchard, p. 96, fig. 22A.
2007 *Icriospathodus collinsoni* (Solien); Orchard p. 96, fig. 2.
2007 *Icriospathodus collinsoni* (Solien); Lucas & Orchard, p. 123, figs 7.4–7.7, 7.13–7.15.
2011 *Icriospathodus collinsoni* (Solien); Ji *et al.*, p. 221, fig. 5a–c.
2014 *Icriospathodus collinsoni* (Solien); Maekawa & Igo *in* Shigeta *et al.*, p. 260, figs 186.10–22, 187–191, 192.1–6.
2015 *Icriospathodus collinsoni* (Solien); Chen *et al.*, p. 113, fig. 9.1–4.
2015 *Icriospathodus collinsoni* (Solien); Yan *et al.*, p. 240, fig. 3.5–6.
2016 *Icriospathodus collinsoni* (Solien); Komatsu *et al.*, p. 69, fig. 5.9.
2018 *Icriospathodus collinsoni* (Solien); Maekawa *in* Maekawa *et al.*, pp. 49–51, figs 28.5–10, 29.1–7.
2019 *Icriospathodus collinsoni* (Solien); Chen *et al.*, fig. 6 nr. 10–12.
2020 *Icriospathodus collinsoni* (Solien); Liu *et al.*, p. 14, pl. 4, figs 6–8.
2021 *Icriospathodus collinsoni* (Solien); Chen *et al.*, figs 4.9–11.

*Material.* 50 specimens

*Remarks.* This species shows a wide range of intraspecies variation (Koike 1992). Chen *et al.* (2019) reported short and abundant occurrences of this species in other sections of Oman and suggested that such pulses may be controlled by an environmental factor. Based on our collections in other sections in both Oman and China, we concur with this observation and interpretation.

*Occurrence.* Worldwide from the lower and middle Spathian. Wadi Musjah (samples WMJ25C, WMJ 26C), lower Spathian, Hawasina Nappes, Oman.

## Genus TRIASSOSPATHODUS Kozur *et al.*, 1998

*Type species & holotype. Spathognathodus homeri* Bender, 1970 (pp. 528–529, pl. 5, fig. 16a–c).

*Type stratum & locality.* Marmarotrapeza Formation, Marathovuno, Chios, Greece.

*Remarks.* Kozur *et al.* (1998) separated this genus from *Neospathodus* on the basis of a downturning of the posterior lower margin in the $P_1$ element. Later Orchard (2005) tentatively reconstructed its multielement apparatus and revised its diagnosis accordingly. Because the collections that Orchard used for his reconstructions were mostly from the late Spathian (e.g. uppermost part of the Guandao section, Orchard 2005), it is still unclear to date whether all early or middle Spathian forms of '*Triassospathodus*' possessed the S elements that are now diagnostic of the genus. Here we tentatively assign all Spathian species of the *homeri–symmetricus* group (Orchard 2007) to *Triassospathodus*: *Tr. homeri*, *Tr. symmetricus*, *Tr. brochus*, *Tr. sosioensis*, *Tr. chionensis*, *Tr. pusillus* and *Tr. anhuiensis*.

### *Triassospathodus symmetricus* (Orchard, 1995)
Figures 9E; 10E, F, H, I, J; 12B; 15D, G

1970 *Neospathodus homeri* Bender, p. 245, pl. 1, figs 2, 3, 9, 10.
1970 *Neospathodus triangularis* Bender; Sweet, pp. 253–254, pl. 1, figs 7, 8.
1973 *Neospathodus homeri* Bender; Mosher, p. 171, pl. 20, fig. 14.
1977 *Neospathodus homeri* Bender; Goel, p. 1097, pl. 2, figs 10, 11.
1986 *Neospathodus homeri* Bender; Durkoop *et al.*, pl. 20, figs 9–10.
*1995 *Neospathodus symmetricus* Orchard, p. 120, 121, figs 2.6, 2.10–13, 2.18.
2004 *Neospathodus symmetricus* Orchard; Koike, p. 137, figs 35–38.
2007*a* *Triassospathodus* ex. gr. *homeri* (Bender); Orchard *et al.*, p. 345, fig. 5.5, 5.6.
2009 *Triassospathodus* ex. gr. *homeri* (Bender); Orchard & Zonneveld, p. 788, fig. 15, parts 38–40.
2011 *Neospathodus symmetricus* Orchard; Ji *et al.*, p. 219, figs 3.5a–c.
2014 *Triassospathodus symmetricus* (Orchard); Maekawa & Igo *in* Shigeta *et al.*, p. 254, figs 182–185, 186.1–3
2015 *Triassospathodus symmetricus* (Orchard); Chen *et al.*, figs 7.16–17, 8.19, 9.15.
2015 *Novispathodus abruptus* (Orchard); Chen *et al.*, figs 8.2, 9.13.
2018 *Novispathodus abruptus* (Orchard); Maekawa *in* Maekawa *et al.*, p. 33, figs 17.22, 17.24, 17.25, 18.4–12, 18.14–22, 18.25, 18.28 (only).
2019 *Triassospathodus symmetricus* (Orchard); Chen *et al.*, fig. 4 nr. 8, 1–13, fig. 5 nr. 4 (only)

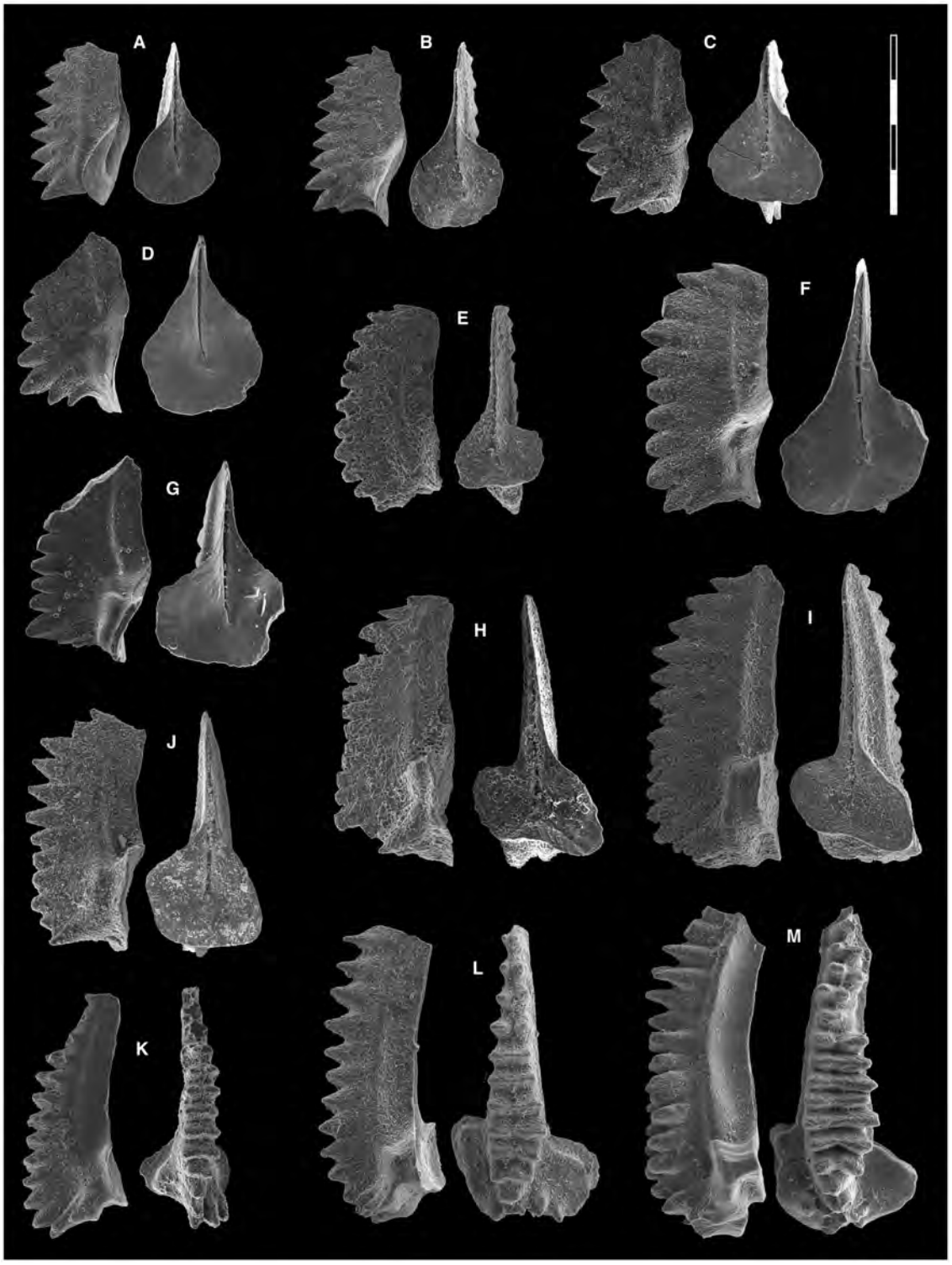


**FIG. 13.** A–D, F–G, *Icriospathodus zaksi* (Buryi): A, WMJ18C, PIMUZ 38866; B, WMJ18C, PIMUZ 38867; C, WMJ18C, PIMUZ 38868; D, WMJ5C, PIMUZ 38869; F, WMJ18C, PIMUZ 38870, G, WMJ18C, PIMUZ 38871. E, H–J, *Icriospathodus crassatus* (Orchard): E, WMJ24C, PIMUZ 38854; H, WMJ24C, PIMUZ 38855; I, WMJ24C, PIMUZ 38856; J, WMJ19C, PIMUZ 38857. K–M, *Icriospathodus collinsoni* (Solien); K, WMJ22C, PIMUZ 38851; L, WMJ26C, PIMUZ 38852; M, WMJ22C, PIMUZ 38853. Original magnification ×80. Scale bar represents 400 μm. All specimens are $P_1$ elements if not otherwise specified. The orientation is standardized with the anterior side to the top and the denticle tips to the left in 'lateral' view.

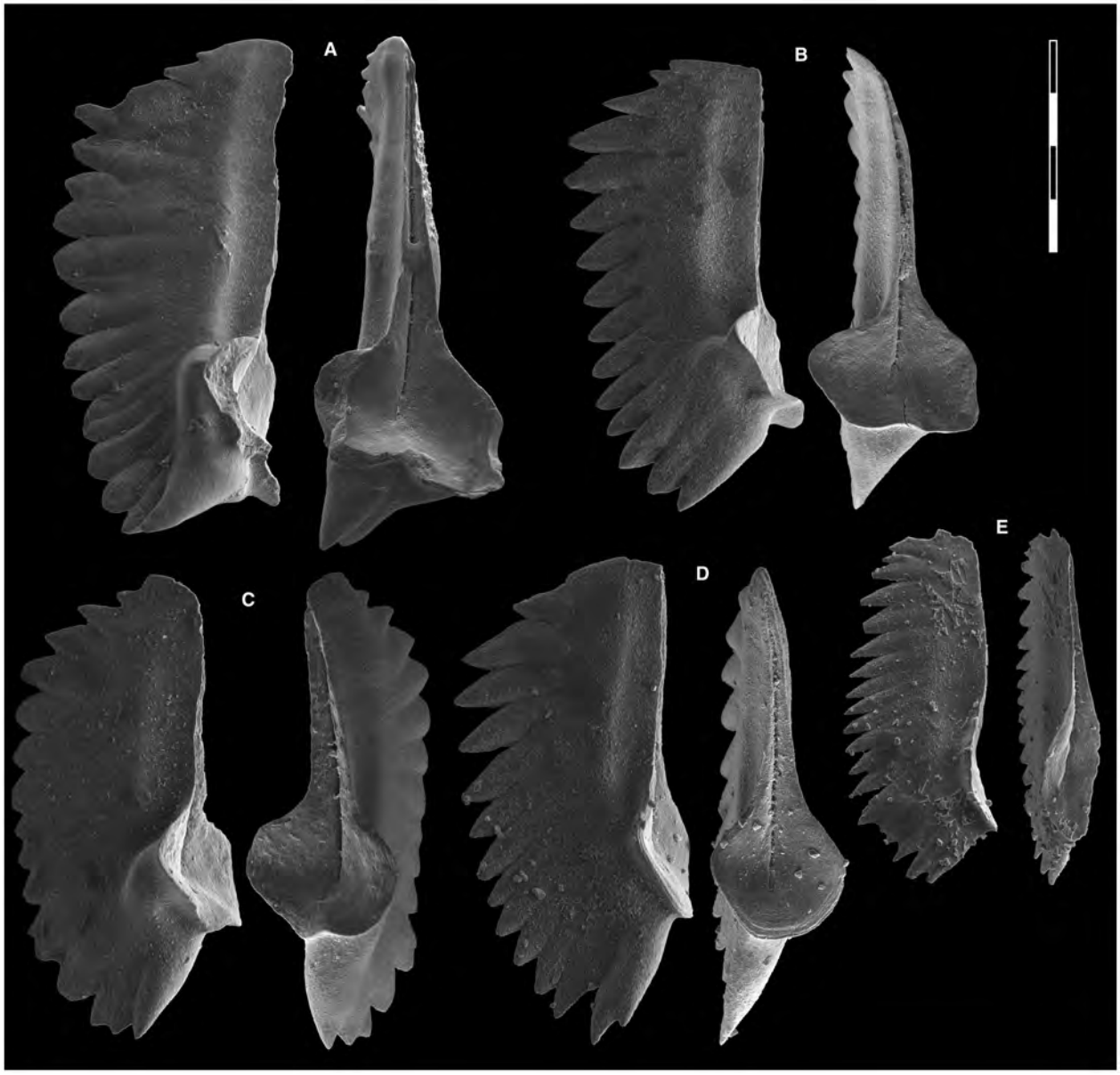


**FIG. 14.** A–B, *Icriospathodus crassatus* (Orchard): A, JA7C, PIMUZ 38862; B, JA7C, PIMUZ 38863. C–D, *Triassospathodus brochus* (Orchard): C, JA7C, PIMUZ 38924; D, JA7C, PIMUZ 38925. E, *Triassospathodus pusillus* (Orchard); JA7C, PIMUZ 38929. Original magnification ×80. Scale bar represents 400 μm. All specimens are $P_1$ elements if not otherwise specified. The orientation is standardized with the anterior side to the top and the denticle tips to the left in 'lateral' view.

*Material.* 60 specimens

*Remarks.* Our specimens from Oman exhibit a range of intraspecies variation similar to that observed in our coeval collections from China (Leu & Goudemand *in* Leu *et al.* (2022) and unpublished collections). The specimens illustrated by Orchard (1995) resemble most closely the specimens of our collections within the lower range of relative basal cavity (e.g. Fig. 15D, G). An incipient posterior denticle may be present. The $P_1$ element of this species is very similar to that of *Nv. abruptus* but differs in having subequally large denticles, not abruptly smaller, posterior denticles. The denticles on the Oman specimens tend also to be more reclined posteriorly. Some specimens with gradually smaller denticles posteriorly (e.g. Fig. 15F, I) may belong to *Nv. abruptus*, but are tentatively included here because their aspect ratio and their posteriorly strongly reclined denticulation are more reminiscent of elements assigned by Orchard (1995) to *Tr. homeri* (see his figs 2.8, 2.15) and because they appear subsymmetrical, which is the main difference between *Tr. homeri* and *Tr. symmetricus*.

*Occurrence.* Worldwide occurrence during the Spathian.

### *Triassospathodus* aff. *symmetricus* (Orchard, 1995)
Figures 9A, 10C?, D?, N

2004 *Neospathodus* sp. aff. *N. symmetricus* Orchard; Koike, p. 133, figs 2.4–5.
2015 *Triassospathodus symmetricus* (Orchard); Chen *et al.*, fig. 8.1.

*Material.* 30 specimens

*Remarks.* These specimens resemble the $P_1$ element of *Tr. symmetricus* but they are relatively shorter and possess a larger basal cavity. Morphologically very similar elements were found in South China (Leu *et al.* 2022). Some specimens (e.g. Fig. 10C, D) may belong here or be considered intermediate between this species and *Nv. pingdingshanensis*.

*Occurrence.* Taho Formation, Southwest Japan, Spathian age (Koike 2004); South China, Luolou Formation, earliest Spathian (Leu *et al.* 2022), WMJ 16 C, WMJ 18C, WMJ 5C, Wadi Musjah, Oman (this study).

### *Triassospathodus homeri* (Bender, 1970)
Figures 9B, 15H

*1970 *Spathognathodus homeri* Bender, p. 528, pl. 5, figs 16a–c.
1970 *Neospathodus homeri* (Bender); Sweet, p. 245, pl. 1, figs 2, 3, 9, 10.
1980 *Neospathodus homeri* (Bender); Chhabra & Sahni, pl. 1, fig. 28 (only).
1983 *Neospathodus homeri* (Bender); Matsuda, pp. 94–95, pl. 4, figs 3–5.
1986 *Neospathodus homeri* (Bender); Durkoop *et al.*, pl. 20, fig. 8a–d.
1995 *Neospathodus homeri* (Bender); Orchard, p. 115, figs 2.1–3, 2.7–9, 2.14–17, 2.20, 2.21.
2005 *Triassospathodus homeri* (Bender); Orchard, p. 93, fig. 19.
2007 *Triassospathodus* ex gr. *homeri* (Bender); Lucas & Orchard, p. 123, figs 7.8–9.
2007*a* *Triassospathodus* ex gr. *homeri* (Bender); Orchard *et al.*, p. 353, fig. 6 nr. 10–12.
2011 *Neospathodus homeri* (Bender); Ji *et al.*, p. 220, fig. 3.9a–c.
2014 *Triassospathodus homeri* (Bender); Maekawa & Igo *in* Shigeta *et al.*, p. 253, fig. 181.43–48.
2015 *Triassospathodus homeri* (Bender); Chen *et al.*, figs 7.13, 8.18, 9.14, 9.19.
2015 *Novispathodus abruptus* (Orchard); Chen *et al.*, figs 7.16–17, 9.16.
2019 *Triassospathodus homeri* (Bender); Chen *et al.*, fig. 7 nr. 1.
2020 *Triassospathodus symmetrucis* [sic.] (Orchard); Liu *et al.*, p. 12, pl. 2, fig. 11.
2021 *Novispathodus abruptus* (Orchard); Chen *et al.*, fig. 4.3.
2021 *Triassospathodus homeri* (Bender); Chen *et al.*, fig. 4.15, 4.16 (only).
2021 *Triassospathodus symmetricus* (Orchard); Chen *et al.*, fig. 7.2 (only).

*Material.* 80 specimens

*Remarks.* The $P_1$ element of *Tr. homeri* differs from that of *Tr. symmetricus* in having a more differentiated posterior process and a narrower, more elongated and asymmetrical basal cavity that is tapered to both posterior and anterior ends.

*Occurrence.* Worldwide occurrence during the Spathian and earliest Anisian.

### *Triassospathodus brochus* (Orchard, 1995)
Figures 14C–D, 15A, B, E, F, I?

*1995 *Neospathodus brochus* Orchard, p. 119, figs 3.27, 3.28, 3.35, 3.36.
2015 *Triassospathodus brochus* Orchard; Yan *et al.*, p. 240, fig. 3.15–3.17.
2015 *Triassospathodus brochus* Orchard; Sun *et al.*, p. 73, fig. 9.5.

*Material.* 25 specimens

*Remarks.* The $P_1$ element of this species resembles the homologous element of other *Triassospathodus* species but its denticles are subequally large and gradually strongly reclined posteriorly, such that the posteriormost denticle makes an angle of *c.* 160° with the element's lower margin. Compared with *Nv. curtatus*, which has similar features but less strongly reclined posterior denticles, its length–height aspect ratio is much larger and its basal cavity more elliptical (rather than triangular). The denticulation of the elements illustrated by Orchard (1995) is also more discrete. The denticulation of the specimens included here is not as discrete and may be more reminiscent of *Nv. curtatus* but their length–height aspect ratio and their basal cavity are more similar to that of *Tr. brochus*, to which we tentatively assign them. Alternatively, these elements may deserve to be assigned to a new, separate, possibly older species: the specimens of *Tr. brochus* described by Orchard (1995) were dated as late Spathian in age and hence are younger than the present specimens.

*Occurrence.* Jebel Aweri (sample 7C), Wadi Musjah (samples WMJ 21C, WMJ22C, WMJ23C), lower Spathian in the Hawasina nappes and Batain region. Jebel Safra (Orchard 1995). All from Oman. Nanpanjiang basin, South China, Spathian age (Sun *et al.* 2015; Yan *et al.* 2015).

### *Triassospathodus pusillus* (Orchard, 1995)
Figures 14E, 15C

1995 *Neospathodus pusillus* Orchard, p. 120, figs 3.29–34.

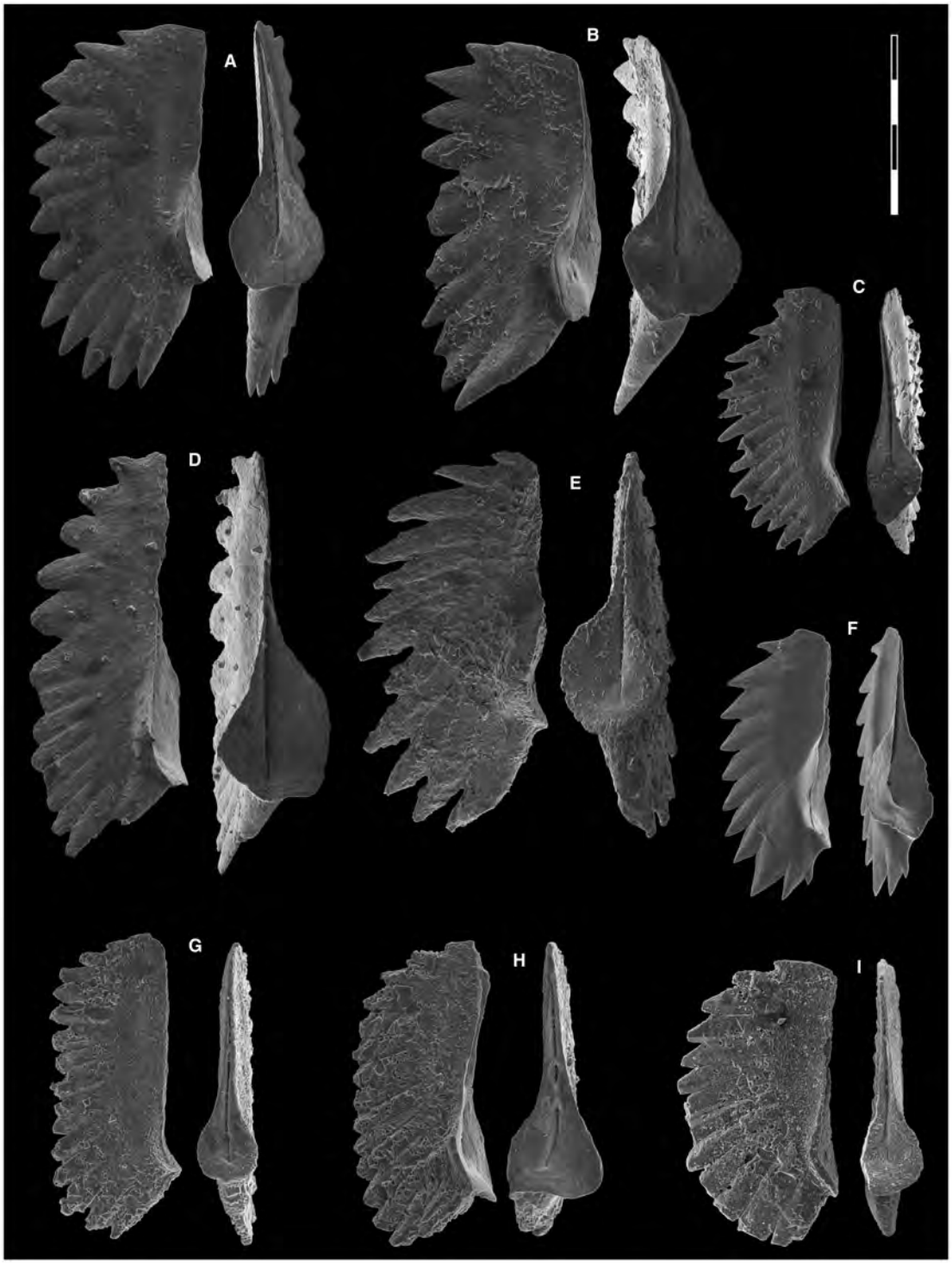


**FIG. 15.** A–B, E–F, I, *Triassospathodus brochus* (Orchard): A, JA7C, PIMUZ 38919; B, JA7C, PIMUZ 38920; E, JA7C, PIMUZ 38921; F, WMJ22C, PIMUZ 38922; I, WMJ21C, PIMUZ 38923. C, *Triassospathodus pusillus* (Orchard); JA7C, PIMUZ 38928. D, G, *Triassospathodus symmetricus* (Orchard): D, JA7C, PIMUZ 38930; G, WMJ26C, PIMUZ 38931. H, *Triassospathodus homeri* (Bender); WMJ26C, PIMUZ 38926. Original magnification ×80. Scale bar represents 400 μm. All specimens are $P_1$ elements if not otherwise specified. The orientation is standardized with the anterior side to the top and the denticle tips to the left in 'lateral' view.

*Material.* 15 specimens

*Remarks.* The specimens illustrated here are morphologically very similar to the holotype (Orchard 1995), also described from Oman. They feature the characteristic numerous, needle-like denticles, the narrow elongate basal cavity and the higher at mid-length blade.

*Occurrence.* Jebel Aweri (sample 7C) Batain, Jebel Safra (Orchard 1995), lower Spathian, Oman.

### Subfamily NEOGONDOLELLINAE Hirsch, 1994
### Genus MAGNIGONDOLELLA Golding & Orchard, 2018

*Type species.* *Magnigondolella salomae* Golding & Orchard, 2018

*Type stratum & locality.* *Paracrochordiceras americanum* Zone (lower Anisian) of the Toad Formation, northeastern British Columbia, Canada.

*Remarks.* The $P_1$ element is diagnostic and characterized by a uniformly high, fused carina. The denticles of *Borinella* are more discrete and are gradually larger anteriorly. The $P_1$ element of *Neogondolella* tends to be arched and the carina lower, especially at mid-length. Although these three genera differ in their other elements with reasonable probability, the $P_1$ elements may be very difficult to distinguish. *Borinella* may have a very similar multielement apparatus to *Neogondolella* (Orchard 2005).

Some species around the Smithian–Spathian transition tend to be intermediate between *Borinella*, *Neogondolella* and *Magnigondolella*. Given that the latter two genera are defined using much younger collections and correspond to extreme cases in the segminiplanate morphospace, it is at times difficult to make genus-level assignments for these intermediate species.

#### *Magnigondolella mutata* (Orchard, 2021)
Figures 16A, B, 17D, E?

2007 *Neogondolella* sp. D; Orchard, p. 99, text-fig. 1.
2019 *Neogondolella* ex. gr. *jakutensis* Dagis; Chen *et al.*, fig. 4.1 (only).
2019 *Neogondolella* sp. B; Chen *et al.*, fig. 5.3.
*2021 *Magnigondolella mutata* Orchard, fig. 13Z–AF.

*Material.* >20 specimens

*Description.* The segminiplanate $P_1$ elements have a developed teardrop-shaped platform that tapers gradually towards the anterior end. There is no free blade. A very narrow brim may be present posteriorly. Micro-ornamentation (isometrical polygonal epithelial cell imprints) is visible around the swollen platform margins. The subequal denticles are high and fused, a characteristic feature of *Magnigondolella*. The cusp is neither terminal, nor conspicuous.

*Remarks.* A specimen (Fig. 17E) is morphologically very similar to *Mg. mutata* but differs in having a large terminal cusp. It is unclear whether it should be included herein.

*Occurrence.* Radio Tower section, Oman (Chen *et al.* 2019); Jebel Aweri, Batain and Wadi Musjah, Hawasina nappes, Oman (this study).

#### *Magnigondolella?* sp. A
Figures 16E, 17F

2021 *Magnigondolella* sp.; Golding, fig. 5 nr. 13–15.

*Material.* 5 specimens

*Description.* Segminiplanate $P_1$ element with a relatively narrow but deep, thickened platform. Large terminal cusp surrounded by a platform brim. The other denticles are subequal in size and discrete. In anterior–posterior cross-section, the platform has a deltoid shape due to the thickening of the blade. A microreticulation is present on the upper margin of the platform.

*Remarks.* The platform of these elements is narrower and deeper than that of representatives of *Mg. mutata*. It has a deltoid rather than hastate (triangular with sharp basal loops) outline in transverse section. The thickened platform and the relatively low carina (in comparison with other *Magnigondolella* species) bearing discrete denticles are reminiscent of the genus *Gladigondolella*, but a posterior process is missing in these specimens.

*Occurrence.* Jebel Aweri, Wadi Musjah, lower Spathian, Oman (this study). Northern Indian Margin, Kashmir, as yet unpublished collection.

### Genus BORINELLA Budurov & Sudar, 1994

1988 *Pseudogondolella* Kozur, p. 244.
1993 *Kozurella* Budurov & Sudar, p. 24.
*1994 *Borinella* Budurov, p. 30 (June).
1994 *Chengyuania* Kozur, pp. 529–530 (September).

*Type species.* *Neogondolella buurensis* Dagis, 1984.

*Type stratum & locality.* Buur River Basin, Northern middle Siberia, Lower Triassic *Hedenstroemia* Zone, Russia.

#### *Borinella buurensis* (Dagis, 1984)
Figures 17A, 18A, E, F, G?

1978 *Neogondolella jubata* Sweet; Weitschat & Lehmann, p. 98, pl. 13, figs 1–6.
*1984 *Neogondolella buurensis* Dagis, p. 12, pl. 2, figs 6–15; pl. 3, figs 1–2; pl. 11, figs 1–4; pl. 12, figs 1, 2; pl. 16, figs 1–4.
1984 *Neogondolella elongata* Sweet; Hatleberg & Clark, pl. 1, fig. 14 (only).
2005 *Neogondolella* aff. *sweeti* Kozur & Mostler; Zhao, p. 131, pl. 13, fig. 1.

2007 *Borinella buurensis* (Dagis); Orchard, p. 113, pl. 1, figs 7, 15, 27.
2008 *Borinella buurensis* (Dagis); Nakrem *et al.*, p. 528, fig. 4.19.
2008 *Borinella* aff. *buurensis* (Dagis); Nakrem *et al.*, p. 528, fig. 4.17–4.18.
2008 *Borinella buurensis* (Dagis); Orchard, p. 400, figs 5.9–13.
2012*a* *Borinella* aff. *buurensis* (Dagis); Goudemand & Orchard *in* Goudemand *et al.*, p. 1032, figs 2AA.
2015 *Borinella* aff. *buurensis* (Dagis); Chen *et al.*, fig. 9.11.
2018 *Borinella* aff. *buurensis* (Dagis); Maekawa *in* Maekawa *et al.*, p. 45, fig. 29.27.
2019 *Neogondolella* ex. gr. *jakutensis* Dagis; Chen *et al.*, figs 4.3, 4.5 (only).
2020 *Borinella* aff. *buurensis* (Dagis); Liu *et al.*, p. 13, pl. 3, fig. 10 (only).
2021 *Borinella* aff. *buurensis* (Dagys); Chen *et al.*, fig. 5.9 (only).
2021 *Borinella buurensis* (Dagys) Golding, fig. 5 nr. 10–12.

*Material.* 20 specimens

*Remarks.* In oral view, our specimens of *Bo. buurensis* strongly resemble our specimens of *Mg. mutata* (see above) but in lateral view it is clear that their carinas differ in being gradually higher and more discrete towards the anterior end, a typical *Borinella* feature. Compared with the holotype of *Bo. buurensis*, the specimens from Oman tend to have a more fused and higher carina. Dagis (1984, pl. 2, figs 13–15) illustrated similar specimens with a more prominent, fused carina and a terminal cusp, suggesting that such variation is considered as intraspecific. The specimens from Oman closely resemble coeval elements found in China (compare Fig. 18F, G, with Leu *et al.* 2022, fig. 13A), in Kashmir (M. Leu, collection from 2013 Guryul Ravine expedition stored at University of Zurich), or in North America (compare Fig. 18A with Orchard 2021, fig. 9N). The distinction from *Bo. sweeti* is not trivial because transitional forms occur. Most of these specimens have a straight carinal axis and are rounded posteriorly, which is reminiscent of *Bo. sweeti*. However, their relatively long and discrete blade denticles seems more compatible with *Bo. buurensis*. They may also deserve assignment to a separate morphotype or species in the future based on the high carina and the more rectangular platform (e.g. *Bo.? curvata*; Orchard 2021).

Chen *et al.* (2019) illustrated similar specimens from another locality in Oman, which they mostly assigned to *Ng.* ex. gr. *jakutensis* Dagis. Because *Ng. jakutensis* has slimmer platforms and no platform brim at the posterior end, we question this assignment.

*Occurrence.* Jebel Aweri, Wadi Musjah, Smithian–Spathian transition, Oman (this study). South China, *Nv. pingdingshanensis* Zone (Goudemand *et al.* 2012*a*; Chen *et al.* 2015); Japan (Maekawa *et al.* 2018), *Hedenstroemia* zone; Siberia (Dagis 1984), *Tardus* zone; Canadian Arctic (Orchard 2008), Spitsbergen (Weitschat & Lehmann 1978; Nakrem *et al.* 2008).

### *Borinella*? aff. *sweeti* (Kozur & Mostler, 1976)
Figure 17C

*Material.* 5 specimens

*Description.* The platform margins are subparallel for most of the element length, the platform anterior is tapered. The pronounced cusp is accompanied by a similarly high denticle (bicuspidate form) and a small gap separates them from the anterior ones, which are moderately fused and subequal in height.

*Remarks.* The carina is lower and the fusion of the denticles is less developed than in *Bo. sweeti* or *Bo. buurensis*. The accessory carinal nodes on the posterior part are also reminiscent of *Bo. buurensis*. This specimen shows also some affinity with *Neogondolella* but neither its carinal profile in lateral view nor its accessory posterior denticles are typical of the latter.

*Occurrence.* Wadi Musjah WMJ18C, Oman (this study).

### *Borinella*? sp. A
Figure 19A

*Material.* 2 specimens

*Description.* Segminiplanate to carminiplanate $P_1$ element with a narrow, subsymmetrical biconvex-shaped platform that tapers at both ends. The posteriormost denticles appear to be set on a short, constricted posterior process. The carinal denticles are subequally high and strongly fused at midlength, more discrete anteriorly.

*Occurrence.* Jebel Aweri, Batain, Oman (this study).

### *Borinella*? sp. B
Figure 19B

2019 *Neogondolella* ex. gr. *jakutensis* Dagis; Chen *et al.*, fig. 5.1.

*Material.* 2 specimens

*Remarks.* These specimens resemble *Bo.* aff. *sweeti* except for the presence posteriorly of two bifurcated nodes. They may represent gerontic forms of the latter. Similar specimens are known from Kashmir (M. Leu, collection from 2013 expedition stored at University of Zurich).

*Occurrence.* Radio Tower section, UAZ5, Oman (Chen *et al.* 2019), Jebel Aweri, Batain, Oman (this study); Unit H3, Khunamuh Formation, Guryul Ravine, Kashmir (M. Leu, collection from 2013 expedition stored at University of Zurich)

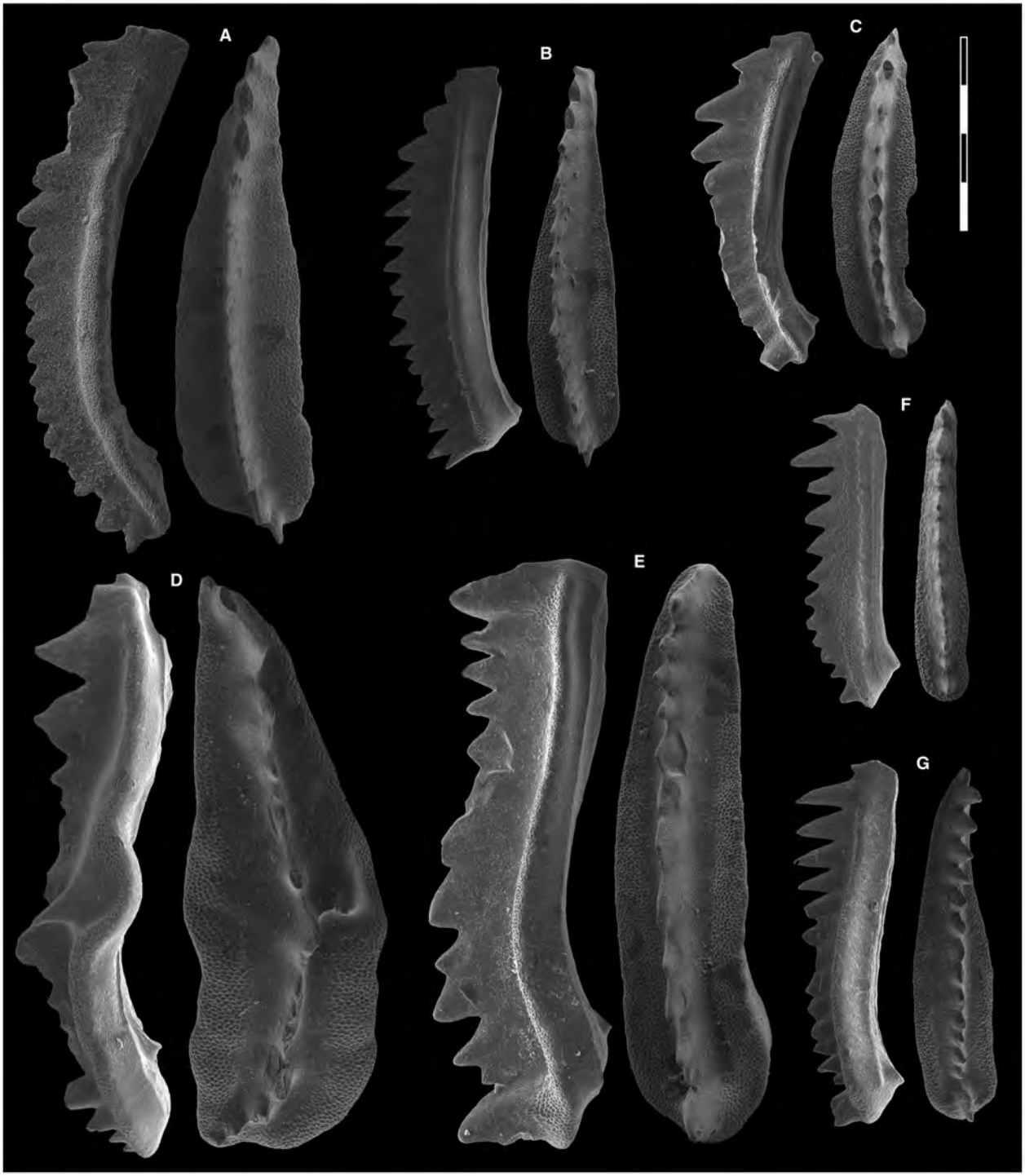


**FIG. 16.** A–B, *Magnigondolella mutata* (Orchard): A, JA15C, PIMUZ 38877; B, JA15C, PIMUZ 38878. C, *Borinella*? sp. C *sensu* Orchard (2007); JA13C, PIMUZ 38841. D, *Neogondolella*? sp. A; JA36C, PIMUZ 38882. E, *Magnigondolella*? sp. A; JA30C, PIMUZ 38880. F, *Borinella*? *jakutensis* (Dagis); JA13C, PIMUZ 38838. G, *Borinella sweeti* (Kozur & Mostler); JA 29C, PIMUZ 38842. Original magnification ×80. Scale bar represents 400 μm All specimens are $P_1$ elements if not otherwise specified. The orientation is standardized with the anterior side to the top and the denticle tips to the left in 'lateral' view.

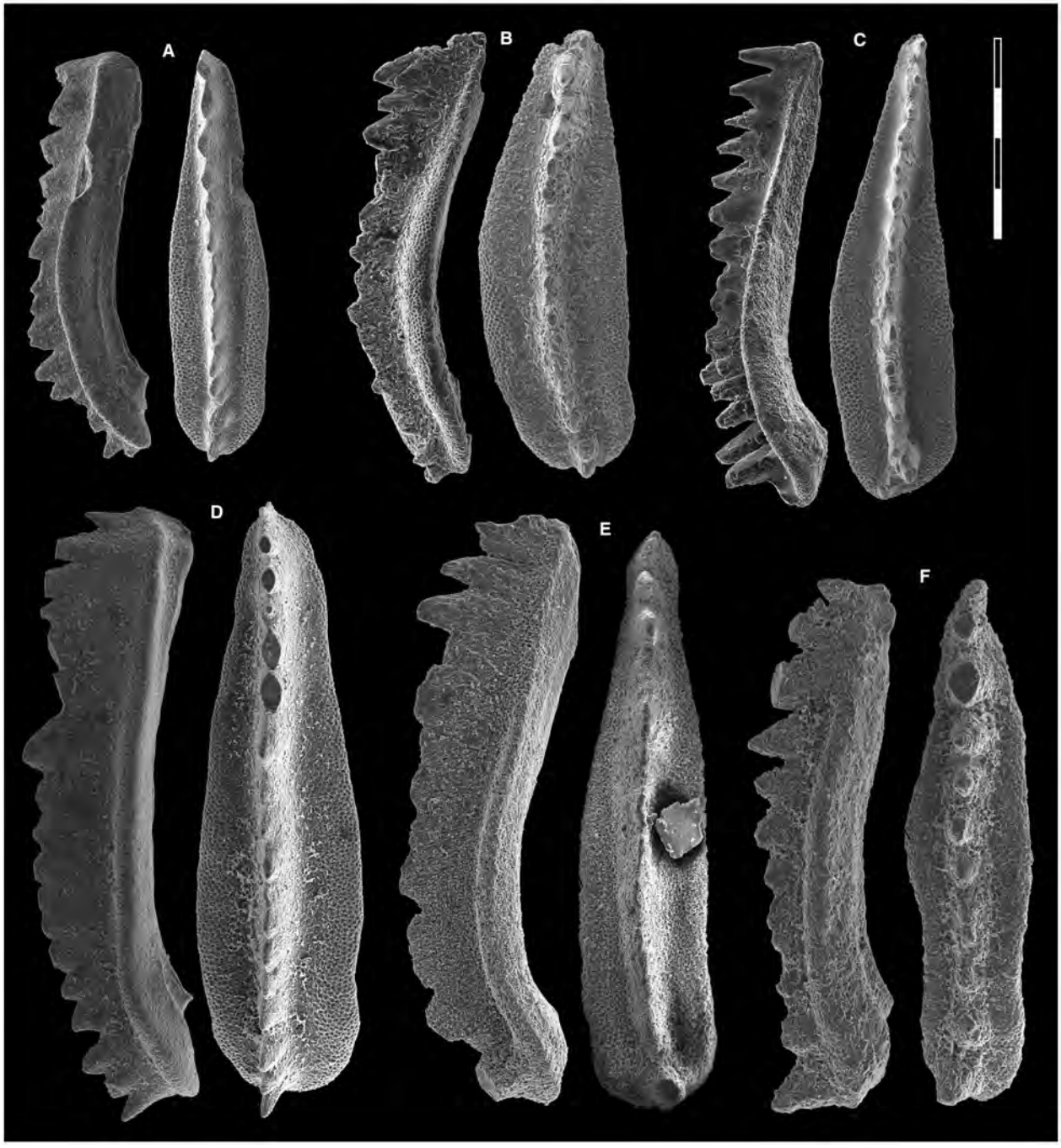


**FIG. 17.** A, *Borinella buurensis* (Dagis); WMJ5C, PIMUZ 38832. B, *Borinella curvata* (Orchard); WMJ15C, PIMUZ 38837. C, *Borinella*? aff. *sweeti* (Kozur & Mostler); WMJ15C, PIMUZ 38831. D, *Magnigondolella mutata* (Orchard); WMJ18C, PIMUZ 38879. E, *Magnigondolella* aff. *mutata* (Orchard); WMJ16C, PIMUZ 38876. F, *Magnigondolella*? sp. A; WMJ26C, PIMUZ 38881. Original magnification ×80. Scale bar represents 400 μm. All specimens are $P_1$ elements if not otherwise specified. The orientation is standardized with the anterior side to the top and the denticle tips to the left in 'lateral' view.

*Borinella*? sp. C *sensu* Orchard (2007)
Figure 16C

2007 *Borinella*? sp. C; Orchard, p. 99, text-fig. 1.
2021 '*Borinella*' *laii* Chen; Orchard, fig. 9Z, AA.

*Material.* 5 specimens

*Diagnosis & description.* See Orchard (2021).

*Remarks.* The denticles of this specimen are partly broken in the posterior part. We tentatively assign it to *Borinella*? sp. C *sensu*

Orchard, a species first described by Orchard (2007) from the Oman collections as 'early *Gladigondolella*'. A formal description of this species is still pending. Although Orchard (2021) assigned this species to '*Borinella*' *laii* (Chen *et al*. 2021), the latter usually develops a posterior denticle behind the large cusp, which is not the case in the illustrated specimen of Orchard (2021, fig. 9Z–AA). Its denticles are more fused than typical *Borinella* specimens but they tend to be getting higher and more discrete to the anterior, which is typical for that genus. In oral view the platform is teardrop shaped, rounded posteriorly, gradually tapered anteriorly. A platform brim is present around the large, terminal, slightly reclined cusp. The main axis is slightly flexed laterally.

*Occurrence.* Oman: Jebel Aweri (JA13C), Hawasina Nappes, Jebel Safra, (Orchard 2021).

### Genus NEOGONDOLELLA Bender & Stoppel, 1965

*Neogondolella*? sp. A

Figure 16D

*Material.* 3 specimens

*Remarks.* These presumably pathological specimens resemble *Bo. buurensis* in oral view, especially because of their small posterior carinal nodes that are deflected laterally. In lateral view the denticles, which may have been broken and possibly badly repaired, are more reminiscent of *Neogondolella*, but with considerable uncertainty. Very similar (also presumed pathological) elements are known from coeval collections from Kashmir (M. Leu, collection from 2013 Guryul Ravine expedition stored at University of Zurich)

*Occurrence.* Unit H3, Khunamuh Formation, Guryul Ravine, Kashmir (M. Leu, collection from 2013 expedition stored at University of Zurich).

### Subfamily GLADIGONDOLELLINAE Hirsch, 1994

### Genus GLADIGONDOLELLA Müller, 1962

1968 *Dichodella* Mosher, p. 923

*Type species. Polygnathus tethydis* Huckriede, 1958 (pp. 157–158, pl. 2, fig. 38a–b).

*Type stratum & locality. Trachyceras austriacum* bed (Julian), Feuerkogel near Röthelstein, Austria.

### *Gladigondolella tethydis* (Huckriede, 1958)

Figure 12D, E

*1958 *Polygnathus tethydis* Huckriede, pl. 12, fig. 38a–b; pl. 13, figs 2–5.
1968 *Gladigondolella tethydis* (Huckriede); Nogami, pl. 9, figs 1–10, pl. 11, figs 5, 6.
1980 *Gladigondolella tethydis* (Huckriede); Kovács & Kozur, pl. 3, figs 5, 6.
2007*a* *Gladigondolella tethydis* (Huckriede); Orchard *et al*., fig. 6.35.
2007*b* *Gladigondolella tethydis* (Huckriede); Orchard *et al*., fig. 5.29, 5.30.
2010 *Gladigondolella tethydis* (Huckriede); Orchard, figs 7.1–7.3.
2011 *Gladigondolella tethydis* (Huckriede); Ishida & Hirsch, figs 7.1, 7.2
2015 *Gladigondolella tethydis* (Huckriede); Ovtcharova *et al*., fig. 3 G.
2016 *Gladigondolella tethydis* (Huckriede); Kilic, figs 5.1, 5.7–5.9, 6.8, 6.9.

*Material.* 5 specimens

*Remarks.* These carminate $P_1$ elements are characterized by discrete, rounded, low carinal nodes. The elongated platform is narrow. A keel is present posterior of the pit. It has been suggested that *Gladigondolella* may have evolved from *Cratognathus* during the late Spathian (Chen *et al*. 2016) or from *Borinella* in the Spathian (Orchard 2007). Orchard (2007) mentioned that $P_1$ elements similar to '*Gladigondolella*' *carinata* occur in Spathian collections from Oman and may represent the earliest representatives of that genus (recently described as *Bo.*? *laii* in Orchard 2021), although the other elements of the apparatus remain undescribed and do not correspond to those of the type species *Gladigondolella tethydis*, as reconstructed by Orchard (2005) from the Middle Triassic (hence the quotes). *Gladigondolella tethydis* itself is known to date only from Anisian strata and it was actually proposed as one of several proxies for the definition of the base of the Anisian (Goudemand *et al*. 2012*b*). Hence it is very surprising to find these specimens in the earliest Spathian, co-occurring with *Nv. pingdingshanensis* (Fig. 4). Their presence suggests that the origin of '*Gladigondolella*' is even older. Stratigraphic admixture can be excluded with almost certainty for the following reasons: No 'jumps' in the carbon isotope record, no visible admixture in the sedimentology (see Appendix S1), no unusual ammonoid faunas and no co-occurrence of other (typically younger) conodont species with *Gladigondolella tethydis*.

*Occurrence.* Worldwide, usually found from around the Spathian–Anisian boundary until the Carnian. The oldest '*Gladigondolella*' specimens are reported from WMJ17C, at the base of the Spathian (this study).

### Subfamily MULLERINAE Orchard, 2005

### Genus DISCRETELLA Orchard, 2005

*Type species & holotype. Ctenognathus discreta* Müller, 1956 (pp. 821–822, pl. 95, fig. 28).

*Type stratum & locality.* Smithian ammonoid bed, Crittenden Springs, Elko County, Nevada.

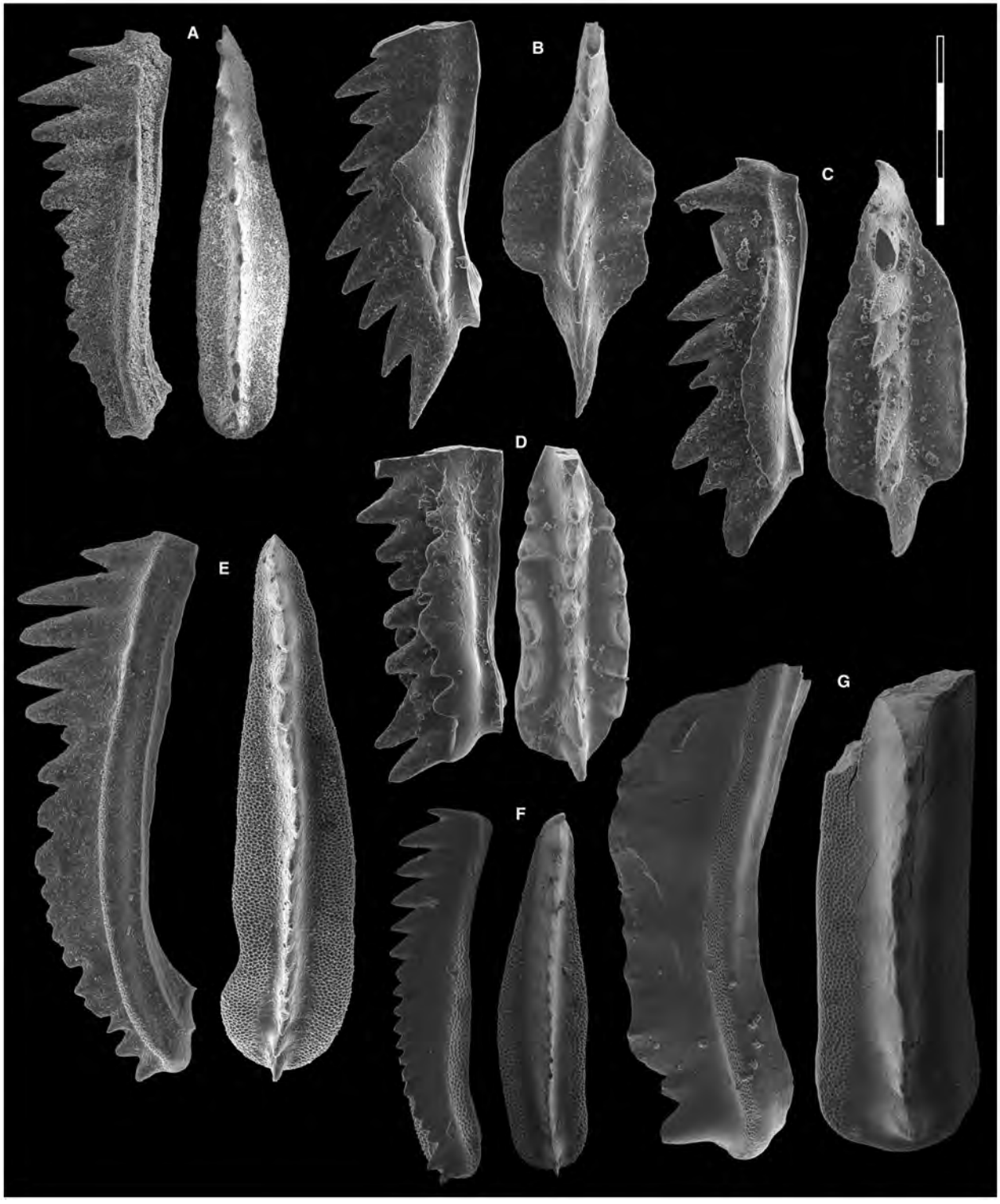


**FIG. 18.** A, E–G, *Borinella buurensis* (Dagis): A, WMJ19C, PIMUZ 38833; E, JA15C, PIMUZ 38834; F, JA15C, PIMUZ 38835; G, JA13C, PIMUZ 38836. B–D, *Scythogondolella* ex gr. *milleri* (Müller): B, WMJ2C, PIMUZ 38911; C, WMJ2C, PIMUZ 38912; D, WMJ2C, PIMUZ 38913. Original magnification ×80. Scale bar represents 400 μm. All specimens are $P_1$ elements if not otherwise specified. The orientation is standardized with the anterior side to the top and the denticle tips to the left in 'lateral' view.

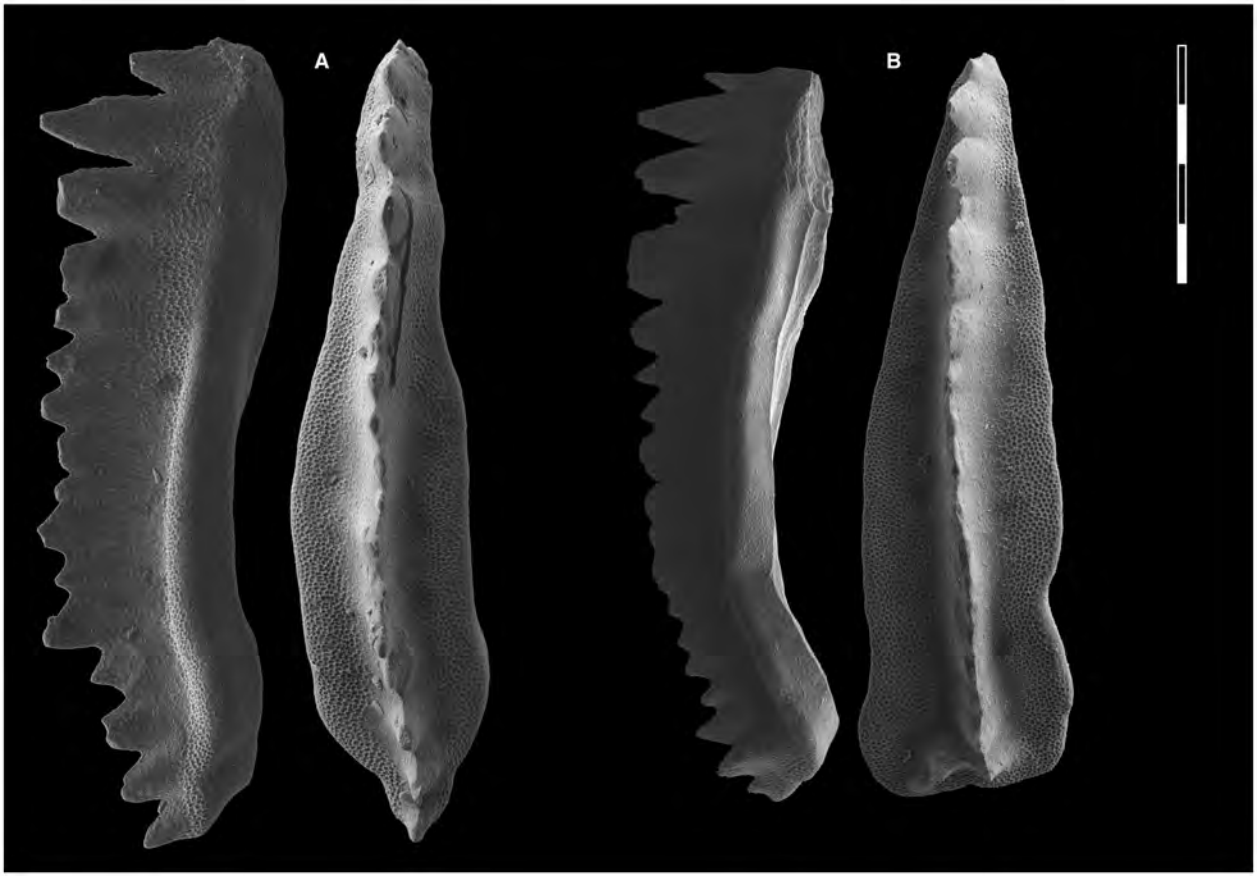


**FIG. 19.** A, *Borinella*? sp. A; JA30C, PIMUZ 38839. B, *Borinella*? sp. B; JA15C, PIMUZ 38840. Original magnification ×80. Scale bar represents 400 μm. All specimens are $P_1$ elements if not otherwise specified. The orientation is standardized with the anterior side to the top and the denticle tips to the left in 'lateral' view.

### *Discretella robusta* (Wang & Wang, 1976)
Figure 20D

1976 *Cratognathodus robustus* Wang & Wang, p. 397, pl. 3, figs 21–25
1983 *Cratognathodus robustus* Wang & Wang; Tian *et al.*, p. 347, pl. 88, fig. 8a, b.
2007 *Guangxidella*? *robustus* (Wang & Wang); Orchard, fig. 1.
2014 *Discretella robustus* (Wang & Wang); Maekawa & Igo *in* Shigeta *et al.*, p. 203, fig. 147, nr. 16–18, 22–33 (only).
2018 *Discretella robusta* (Wang & Wang); Maekawa *in* Maekawa *et al.*, p. 23, fig. 14 nr. 6 (only, juvenile form).
2021 *Guangxidella robustus* (Wang & Wang); Sun *et al.*, fig. 6 nr. 21.

*Material.* 3 specimens

*Description.* Carminate $P_1$ element. The very conspicuous and reclined cusp is larger than adjacent denticles and about twice as wide. The short, slightly downturned posterior process bears 1–2 small denticles. The 3–5 anterior denticles are reclined, discrete, and gradually smaller and less reclined towards the anterior end. The lower margin is sub-straight. The basal cavity is globally subcircular but tapers abruptly under the posterior process.

*Remarks.* The anteriormost part of the illustrated element is broken. The overall shape of this species is reminiscent of that of homologous elements of *Guangxidella*. Orchard (2005) discussed the striking similarities of both genera also in terms of multielement apparatuses.

*Occurrence.* Wadi Musjah (sample WMJ11C), middle Smithian, Hawasina nappes, Oman. *Novispathodus* ex gr. *waageni* Zone (*Flemingites rursiradiatus*, *Urdyceras tulongensis* and *Owenites koeneni* beds; Smithian), Bac Thuy Formation, northeastern Vietnam (Shigeta *et al.* 2014), Qoomolangma, Tibet (Wang & Wang 1976), *Guangxidella bransoni* subzone of the *Nv.* ex. gr. *waageni* zone, southwest Japan (Maekawa *et al.* 2018).

### *Discretella pseudodieneri* Leu & Goudemand *in* Leu *et al.*, 2022
Figure 20A–C

2013 *Neospathodus dieneri* Sweet; Yan *et al.*, p. 516, fig. 6S (only).
2014 *Neospathodus dieneri* Sweet; Maekawa & Igo *in* Shigeta *et al.*, p. 224, fig. 162 nr. 40–42, 46–54 (only).

2014 *Discretella* sp. indet. A; Maekawa & Igo *in* Shigeta *et al.*, pp. 202–207, fig. 151.13–15 (only).
2015 *Discretella* sp.; Chen *et al.*, p. 112, fig. 8.12.
2018 *Neospathodus dieneri* Sweet; Maekawa *in* Maekawa *et al.*, p. 26, fig. 15.32–34 (only).
2021 *Neospathodus* cf. *dieneri discreta*; Sun *et al.*, fig. 5.10.
2021 *Discretella* sp. A; Sun *et al.*, fig. 6.15.

*Material.* 10 specimens

*Remarks.* Leu and Goudemand (Leu *et al.* 2022) differentiated elements that bear some superficial resemblance with *Neospathodus dieneri* but are laterally flattened and exhibit typical features of *Discretella*. The specimens from Oman tend to be larger than those from China and their basal cavity is a bit more upturned. Concomitant with their larger size, they also usually bear 4–5 denticles instead of the 3 denticles typically found in elements from China.

## Subfamily CORNUDININAE Orchard, 2005
## Genus URDYELLA Leu & Goudemand *in* Leu *et al.*, 2022

*Type species. Urdyella unicorna* Leu & Goudemand *in* Leu *et al.*, 2022.

*Type stratum & locality.* Luolou Formation, Laren, Guangxi, South China

### *Urdyella unicorna* Leu & Goudemand *in* Leu *et al.*, 2022
Figure 20E, G, I

1970 *Neospathodus peculiaris* Sweet?; Hasenmüller, p. 62, pl. 2, fig. 10
2005 *Aduncodina unicosta* Ding; Zhao, pl. 6, fig. 9–10.

*Material.* 20 specimens

*Remarks.* In comparison to most of the specimens found in China and Kashmir (see Leu *et al.* 2022), the elements recovered from Oman are particularly well preserved. Their size is similar to that of the largest specimens from China. In those large specimens, an additional anterior node or denticle is often present (see also Leu *et al.* 2022, fig. 20K).

*Occurrence.* Luolou Formation, Smithian age, South China (Leu *et al.* 2022); Khunamuh Formation, unit H2, Smithian age, Guryul Ravine, Kashmir (pers. collection). Wadi Musjah, Smithian age, Oman (this study).

## Subfamily SCYTHOGONDOLELLINAE Orchard, 2007
## Genus SCYTHOGONDOLELLA Kozur, 1989

*Type species. Gondolella milleri* Müller, 1956 (p. 823, pl. 95, figs 4–6).

*Type stratum & locality.* Lower Triassic cephalopod bed, Dinner Springs Canyon, Elko County, Nevada, USA.

### *Scythogondolella* ex. gr. *milleri* (Müller, 1956)
Figure 18B–D

*1956 *Gondolella milleri* Müller, p. 823, pl. 95, figs 1–9.
1956 *Gondolella eotriassica* Müller, pl. 95, figs 10–11.
1966 *Gondolella milleri* Müller; Clark & Mosher, pl. 47, figs 30–35.
1968 *Gondolella milleri* Müller; Nogami, pl. 10, figs 1–5, 8, 9 (only).
1971 *Neogondolella milleri* Müller; Sweet *et al.*, pl. 1, fig. 37.
1973 *Neogondolella milleri* (Müller); Mosher, pl. 19, figs 22, 23, 25.
1976 *Gondolella milleri parva* Kozur & Mostler, pl. 1, fig. 7a–c.
1979 *Neogondolella milleri* (Müller); Buryi, p. 64, pl. 9, fig. 8; pl. 11, figs 4, 6–8; pls 15–16.
1979 *Neogondolella milleri* (Müller); Solien, p. 302, pl. 2, figs 19–26.
1983 *Neogondolella milleri* (Müller); Tian *et al.*, p. 352, pl. 94, figs 2, 4.
1984 *Neogondolella milleri* (Müller); Berry *et al.*, p. 133, pl. 1, figs 12–21.
1984 *Neogondolella milleri* (Müller); Dagis, pl. 4, fig. 2.
1984 *Gondolella milleri* (Müller); Matsuda, pl. 3, figs 1–4.
1984 *Neogondolella milleri* (Müller); Hatleberg & Clark, pl. 4, figs 18, 19?
1991 *Neogondolella milleri* (Müller); Beyers & Orchard, pl. 5, fig. 11.
1997 *Neogondolella milleri* (Müller); Buryi, pl. 2, figs 13–17.
2006 *Scythogondolella milleri* (Müller); Klets & Kopylova, pl. 1, figs 1,6,7.
2008 *Scythogondolella milleri* (Müller); Klets, pl. 1, fig. 1.
2008 *Scythogondolella milleri* (Müller); Nakrem *et al.*, fig. 5.1–3.
2008 *Scythogondolella milleri* (Müller); Orchard, p. 410, fig. 5, parts 5–7.
2009 *Scythogondolella milleri* (Müller); Orchard & Zonneveld, fig. 15, parts 1–5.
2010 *Scythogondolella*? aff. *crenulata* Mosher; Beranek *et al.*, p. 65, figs 6.29, 6.30.
2011 *Neogondolella* sp., Liang *et al.*, fig. 3.10.
2013 *Scythogondolella milleri* (Müller); Bondarenko *et al.*, figs 5.7–14, 6.3.
2013 *Scythogondolella* sp.; Bondarenko *et al.*, fig. 5.6
2018 *Scythogondolella milleri* (Müller); Maekawa *in* Maekawa *et al.*, p. 54, fig. 30.5–11, 30.13–16.
2019 *Scythogondolella* cf. *milleri* (Müller); Li *et al.*, p. 6, fig. 5.22–23.
2019 *Scythogondolella milleri* (Müller); Chen *et al.*, fig. 3.3, 3.10, 3.11.
2019 *Scythogondolella lachryformis* (Müller); Chen *et al.*, fig. 3.4, 3.12 (only).
2019 *Scythogondolella milleri* (Müller); Qiu *et al.*, p. 38, fig. 5.4.

2019 *Scythogondolella lachryformis* (Müller); Qiu *et al.*, p. 38, fig. 5.1, 5.3.
2020 *Scythogondolella milleri* (Müller); Liu *et al.*, p. 11, pl. 1, figs 1, 2.
2020 *Scythogondolella milleri parva* Kozur & Mostler; Liu *et al.*, p. 11, pl. 1, fig. 4.
2020 *Scythogondolella lachryformis* Orchard; Liu *et al.*, p. 11, pl. 1, figs 3, 8 (only).
2020 *Scythogondolella dolosa* Bondarenko & Popov, p. 288, fig. 1 a–d.
2020*a* *Scythogondolella milleri* (Müller); Sun *et al.*, figs 2–6 (natural assemblages of apparatus).
2021 *Scythogondolella milleri* (Müller); Chen *et al.*, figs 5.1–2, 5.5–7, 5.10.
2021 *Scythogondolella milleri* (Müller); Sun *et al.*, fig. 6.23.

*Material.* 40 specimens

*Remarks.* Our collections from Oman exhibit a wide range of intraspecies variation, in particular two possibly distinct morphotypes differentiated by the extension of their platform. (compare Fig. 18B and D). The somewhat typical crenulation of the platform margins is also variable and may be absent, as illustrated in Figure 18C. Pending completion of ongoing revisions based on abundant and well-preserved material from Timor (Dudit *et al.*, unpub. data.), we retain all these variants within a broad *Sc.* ex gr. *milleri*.

*Occurrence.* Worldwide. This species might be more abundant in the high latitudes and the tropics compared with equatorial regions such as South China.

## Suborder PRIONIODININA Donoghue *et al.*, 2008
## Family ELLISONIDAE Clark, 1972
## Subfamily HADRODONTINAE Koike, 2016
## Genus HADRODONTINA Staesche, 1964

*Type species.* *Hadrodontina anceps* Staesche, 1964.

*Type stratum & locality.* Campiller member, Skyth, South Tirol, Italy.

### *Hadrodontina aequabilis* (Staesche, 1964)
Figure 20F ($P_1$ element), 20H ($P_2$ element)

$P_1$ element:

*1964 *Hadrodontina aequabilis* Staesche, p. 275, figs 43, 44.
1984 *Sweetocristatus unicus* Dagis, pp. 37–38, pl. 10, figs 6–9.
1990 *Pachycladina peculiaris* Zhang, pl. 2, fig. 4.
1991 *Pachycladina peculiaris* Zhang *in* Zhang & Yang, p. 40, pl. 3, figs 1, 2.
1997 *Parapachycladina peculiaris* Zhang; Zhang *et al.*, pp. 65–69, pl. 1, figs 1–2; pl. 2, figs 1–2; pl. 3, figs 1–2.
2004 *Ellisonia* sp. aff. *E. triassica* Müller, 1956; Koike *et al.*, figs 8.7, 8.8.
2009 *Ellisonia*? cf. *peculiaris* Sweet; Igo *in* Shigeta *et al.*, p. 182, fig. 152.22.
2013 *Parachirognathus geiseri* Clark; Yan *et al.*, p. 516, fig. 6FF.
2015 *Parachirognathus peculiaris* Zhang & Guo; Chen *et al.*, fig. 8.20–21, 8.24.
2015 *Sweetocristatus unicus* Dagis; Chen *et al.*, fig. 8.23.
2016 *Hadrodontina aequabilis* Staesche; Koike, pp. 164–167, fig. 2 nr. 1–3.
2018 *Hadrodontina aequabilis* Staesche; Maekawa *in* Maekawa *et al.*, p. 18, fig. 13.3?–4 (only).
2020*b* *Hadrodontina aequabilis* Staesche; Sun *et al.*, figs 1–7 (natural assemblage of the *Hadrodontina* apparatus).
2021 *Hadrodontina aequabilis* Staesche; Maekawa & Jenks, fig. 11.1–4.

$P_2$ element:

*1964 *Hadrodontina aequabilis* Staesche, p. 275, fig. 44.
2004 *Ellisonia* sp. aff. *E. triassica* Müller; Koike *et al.*, p. 247, fig. 8.6.
2016 *Hadrodontina aequabilis* Staesche; Koike, p. 165, figs 2.4 ($P_2$ element).
2020*b* *Hadrodontina aequabilis* Staesche; Sun *et al.*, figs 1–7 (natural assemblage of the *Hadrodontina* apparatus).

*Material.* 15 $P_1$ elements

*Remarks.* See discussion in Leu *et al.* (2022). The elements from Oman tend to be larger than homologous elements from China and Kashmir (Leu *et al.* 2022; M. Leu, collection from 2013 Guryul Ravine expedition stored at University of Zurich). Very similar $P_2$ elements were also recovered in China (Leu *et al.* 2022, fig. 28B). With three natural assemblages of *Hadrodontina aequabilis* from the late Smithian Helongshan Formation, South China, the Sun *et al.* (2020*b*) findings fit with our observations about the $P_1$ and $P_2$ elements belonging to the same apparatus.

*Occurrence.* Oman: Wadi Musjah, Smithian stage (this study) Russia; Smithian *Hedenstroemia* and *tardus* zones, Siberia (Dagis 1984), Zhitkov Formation, Smithian age, Abrek Bay area, South Primorye (Shigeta *et al.* 2009); China: Beisi Formation,

**FIG. 20.** A–C, *Discretella pseudodieneri* (Leu & Goudemand): A, WMJ6C, PIMUZ 38845; B, WMJ6C; C, PIMUZ 38843, WMJ11C, PIMUZ 38844. D, *Discretella robusta* (Wang & Wang); WMJ11C, PIMUZ 38846. E, G, I, *Urdyella unicorna* Leu & Goudemand: E, WMJ7C, PIMUZ 38939; G, WMJ6C, PIMUZ 38940; I, WMJ6C, PIMUZ 38941. F, *Hadrodontina aequabilis* ($P_1$) Staesche; WMJ11C, PIMUZ 38849. H, *Hadrodontina aequabilis* ($P_2$) Staesche; WMJ2C, PIMUZ 38850. J, *Novispathodus* sp. ($P_2$); WMJ11C, PIMUZ 38910. K, sp. indet. (?$P_2$); WMJ11C, PIMUZ 38914. L, *Novispathodus* sp. (M); WMJ6C, PIMUZ 38909. Original magnification ×80. Scale bar represents 400 μm. All specimens are $P_1$ elements if not otherwise specified. The orientation is standardized with the anterior side to the top and the denticle tips to the left in 'lateral' view.

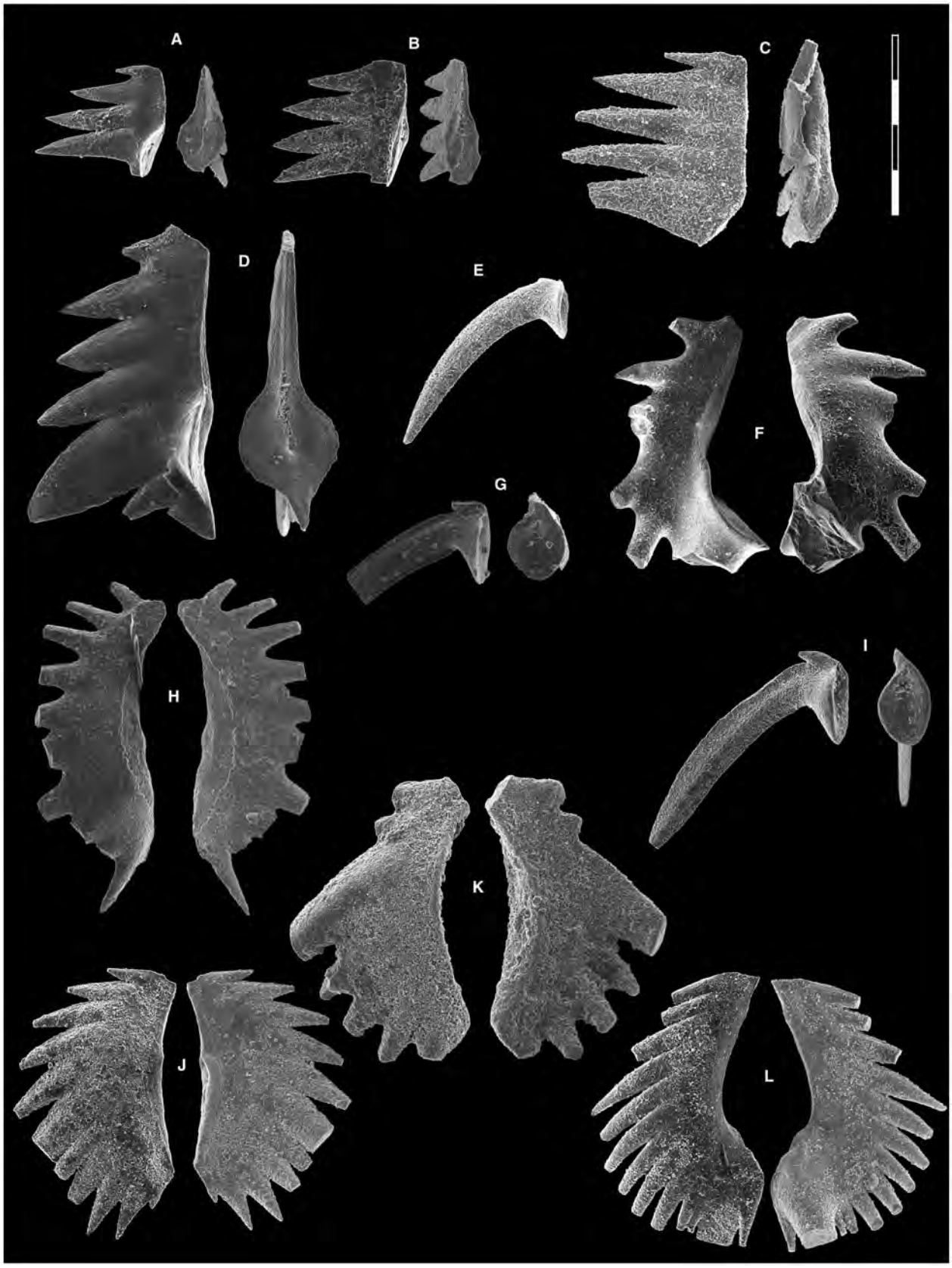

Taiping, Pingguo western Guangxi Province (Zhang *et al.* 1997), Loulou Formation, Smithian age, Jiarong and Bianyang, Nanpanjiang Basin, southern Guizhou Province (Yan *et al.* 2013; Chen *et al.* 2015); Japan: Taho Formation, Shirokawa-cho, Higashiuwa-gun, Ehime Prefecture (below Smithian–Spathian boundary) (Koike *et al.* 2004; Koike 2016); Europe: Campiller member, Werfen Formation, Skyth, South Tirol, Italy (Staesche 1964).

Family UNKNOWN
Genus UNKOWN
INDET. sp. A *sensu* Orchard *et al.*, 2007*b* (fig. 12A)

2007*b* Genus et sp. nov. A; Orchard *et al.*, p. 345, fig. 5.10.
2007*a* New Genus et sp. A; Orchard *et al.*, p. 353, fig. 6.16.

*Material.* 3 elements

*Remarks.* These extremely thin, blade-like elements resembling S elements of Cornudininae were first reported by Orchard *et al.* (2007*a*, 2007*b*) from latest Spathian collections from China and Romania. We report here their occurrence in much older Spathian collections from Oman ($UAZ_7$, middle Spathian).

*Occurrence.* Around the Spathian–Anisian boundary, North Debrogea, Romania (Orchard *et al.* 2007*b*); China: around the Spathian–Anisian boundary, Guandao (Orchard *et al.* 2007*a*), Monggan-Wan Tuo (Ovtcharova *et al.* 2015); sample JA07, Jebel Aweri, Oman, early–middle Spathian (this study).

*Acknowledgements.* Thomas Brühwiler, Romain Jattiot and Mhairi Reid are thanked for their support in the field and for the insightful discussions. Imaging was performed with equipment maintained by the Centre for Microscopy and Image Analysis, University of Zurich. This work is supported by the Schweizer Nationalfonds (SNF) project 160055.

*Author contributions.* **Conceptualization** M Leu (ML), H Bucher (HB), N Goudemand (NG); **Data Curation** ML, Z Luz (ZL), T Vennemann (TV), M Hautmann (MH); **Formal Analysis** ML, HB, NG, A Baud (AB), MH; **Funding Acquisition** HB; TV; **Investigation** ML, HB, AB, TV, ZL, MH, NG, R Jattiot; **Methodology** ML, HB, NG; **Project Administration** HB; **Resources** ML, HB, AB, TV, NG; **Software** ML, NG, M Brosse; **Supervision** HB, NG; **Validation** ML, HB, NG, AB, TV, ZL, MH, NG; **Visualization** ML, M Brosse; **Writing– Original Draft Preparation** ML, HB, NG; **Writing – Review & Editing** ML, HB, AB, TV, ZL, MH.

## DATA ARCHIVING STATEMENT

Data for this study are available in the Dryad Digital Repository: https://doi.org/10.5061/dryad.37pvmcvp6 Files include the UA matrix in Excel format with the following sheets: the raw data, only the local maximum horizons, the first run when using the UA method in PAST (V.2.17c), the run when applying all of the solutions (from Appendix S2) and the cleaned last version (Appendix S3); and values of the studied carbon isotope samples (Appendix S4).

*Editor.* Paul Smith

## SUPPORTING INFORMATION

Additional Supporting Information can be found online (https://doi.org/10.1002/spp2.1481):
**Appendix S1.** Sedimentological analysis, including Figures S1–S8.
**Appendix S2.** Qualitative solutions for the contradictions when applying the UA method to the data.
**Appendix S3.** Dataset for unitary association analyses.
**Appendix S4.** Carbon isotope data from Wadi Musjah and Jebel Aweri.
**Appendix S5.** Summary of conodont biochronozones and carbon isotope excursions around the Smithian–Spathian transition from Oman and China.
**Fig. S9.** Conodont biochronozones from Oman and South China calibrated against U–Pb ages. Intercalibrated with ammonoid biochronozones from Oman and China and the $\delta^{13}C_{carb}$ records from Jebel Aweri, Wadi Musjah, Qiakong, Laren, Shanggang and Lilong. Timing of Early Triassic after Bayesian age depth model by Widmann (2019), Ammonoid zones after Brayard & Bucher (2008) and Brühwiler *et al.* (2009, 2010, 2012). South China conodont biochronozones after Leu *et al.* (2022).

## REFERENCES

ANGIOLINI, L. and BUCHER, H. 1999. Taxonomy and quantitative biochronology of Guadalupian brachiopods from the Khuff Formation, Southeastern Oman. *Geobios*, **32**, 665–699.
ARMSTRONG, H. A. and DEAN, M. T. 1996. Conodonts from Ruddenleys, Lamancha and Crawford, Southern Uplands, Scotland. *British Geological Survey Technical Report*.
BAUD, A. 2018. Final results and recommendations of the last 10 years IGCP 572 and 630 field workshops in South Turkey, Oman, India (Kashmir) and Armenia. *Journal of Earth Science*, **29**, 733–744.
BAUD, A. 2022. La transition permo-triasique sur la marge omanaise. *In* SOCIÉTÉ GÉOLOLOGIQUE DE FRANCE (ed.) *Destination Oman*. Géochronique, Volume spécial.
BAUD, A. and BERNECKER, M. 2010. *The Permian–Triassic transition in the Oman Mountains*. IGCP 572 Field Guide Book. GUtech, Muscat, 109 pp.
BAUD, A., MARCOUX, J. and STAMPFLI, G. 1990. Evolution of the Oman margin, from rifting to passive margin stage Permian to early Mesozoic. In *Symposium on ophiolite genesis and evolution of oceanic lithosphere*.
BAUD, A., BÉCHENNEC, F., KRYSTYN, L., LE MÉTOUR, J., MARCOUX, J., MAURY, R. and RICHOZ, S. 2001*a*. Permo-Triassic deposits: from the

platform to the basin and seamounts. Pre-conference excursion A01. International Conference on the Geology of Oman. Oman Ministry of Commerce & Industry. 56 pp. https://www.researchgate.net/publication/236624812

BAUD, A., BÉCHENNEC, F., CORDEY, F., LE MÉTOUR, J., MARCOUX, J., MAURY, R. and RICHOZ, S. 2001*b*. Permo-Triassic deposits: from shallow water to base of slope. Post-conference excursion B01. International Conference on Geology of Oman: field guidebook. Oman Ministry of Commerce & Industry. 40 pp. https://www.researchgate.net/publication/236624866

BAUD, A., RICHOZ, S., BEAUCHAMP, B., CORDEY, F., GRASBY, S., HENDERSON, C. M., KRYSTYN, L. and NICORA, A. 2012. The Buday'ah Formation, Sultanate of Oman: a middle Permian to Early Triassic oceanic record of the Neotethys and the late Induan microsphere bloom. *Journal of Asian Earth Sciences*, **43**, 130–144.

BÉCHENNEC, F., LE MÉTOUR, J., RABU, D., VILLEY, M. and BEURRIER, M. 1988. The Hawasina Basin: a fragment of a starved passive continental margin, thrust over the Arabian Platform during obduction of the Sumail Nappe. *Tectonophysics*, **151**, 323–343.

BÉCHENNEC, F., LE METOUR, J., RABU, D., BOURDILLON-DE-GRISSAC, C., DE WEVER, P., BEURRIER, M. T. and VILLEY, M. 1990. The Hawasina Nappes: stratigraphy, palaeogeography and structural evolution of a fragment of the south-Tethyan passive continental margin. *Geological Society, London, Special Publications*, **49**, 213–223.

BÉCHENNEC, F., ROGER, J., CHEVREL, S. and LE MÉTOUR, J. 1992. Explanatory notes to the geological map of Al Ashkharah. Sheet NF40-12, scale 1:250,000. Directorate General of Minerals, Oman Ministry of Petroleum & Minerals, 44 pp.

BENDER, H. 1970. Zur Gliederung der Mediterranen Trias II. Die Conodontenchronologie der Mediterranen Trias. *Annales Géologiques des Pays Helléniques*, **19**, 465–540.

BENDER, H. and STOPPEL, D. 1965. Perm-Conodonten. *Geologisches Jahrbuch*, **82**, 331–364.

BERANEK, L. P., MORTENSEN, J. K., ORCHARD, M. J. and ULLRICH, T. 2010. Provenance of North American Triassic strata from west-central and southeastern Yukon: correlations with coeval strata in the Western Canada Sedimentary Basin and Canadian Arctic Islands. *Canadian Journal of Earth Sciences*, **47**, 53–73.

BERGMANN, C. 1847. About the relationships between heat conservation and body size of animals. *Goett Stud*, **1**, 595–708.

BERNOULLI, D., WEISSERT, H. and BLOME, C. D. 1990. Evolution of the Triassic Hawasina basin, central Oman mountains. *Geological Society, London, Special Publications*, **49**, 189–202.

BERRY, R., BURRET, C. and BANK, M. 1984. New Triassic faunas from East Timor and their tectonic significance. *Geologica et Palaeontologica*, **18**, 127–137.

BEYERS, J. M. and ORCHARD, M. J. 1991. *Ordovician to Triassic conodont paleontology of the Canadian Cordillera*. Geological Survey of Canada: Bulletin, **417**.

BITTNER, A. 1901. Uber Pseudomonotis telleri und verwandte Arten der unteren Trias. *Jahrbuch der kaiserlichkoniglichen Geologischen Reichsanstalt*, **50**, 559–592.

BONDARENKO, L. G. and POPOV, A. M. 2020. A new conodont species *Scythogondolella dolosa* sp. nov. from the *Anasibirites nevolini* Zone (Lower Triassic) of Southern Primorye. *Paleontological Journal*, **54**, 287–289.

BONDARENKO, L., BURYI, G., ZAKHAROV, Y. and POPOV, X. B. 2013. Late Smithian (Early Triassic) conodonts from Artyom, South Primorye, Russian Far East. *The Triassic System: New Developments in Stratigraphy & Paleontology: New Mexico Museum of Natural History & Science Bulletin*, **61**, 55–66.

BRAYARD, A. and BUCHER, H. 2008. *Smithian (Early Triassic) ammonoid faunas from northwestern Guangxi (South China): Taxonomy and biochronology*. Wiley-Blackwell, 179 pp.

BRAYARD, A. and BUCHER, H. 2015. Permian–Triassic extinctions and rediversifications. 465–473. *In* KLUG, C., KORN, D., DE BAETS, K., KRUTA, I. and MAPES, R. H. (eds) *Ammonoid paleobiology: From macroevolution to paleogeography*. Springer.

BRAYARD, A., ESCARGUEL, G., BUCHER, H. and BRÜHWILER, T. 2009. Smithian and Spathian (Early Triassic) ammonoid assemblages from terranes: paleoceanographic and paleogeographic implications. *Journal of Asian Earth Sciences*, **36**, 420–433.

BROSSE, M., BUCHER, H. and GOUDEMAND, N. 2016. Quantitative biochronology of the Permian–Triassic boundary in South China based on conodont unitary associations. *Earth-Science Reviews*, **155**, 153–171.

BROSSE, M., BUCHER, H., BAUD, A., FRISK, Å. M., GOUDEMAND, N., HAGDORN, H., NÜTZEL, A., WARE, D. and HAUTMANN, M. 2019. New data from Oman indicate benthic high biomass productivity coupled with low taxonomic diversity in the aftermath of the Permian–Triassic Boundary mass extinction. *Lethaia*, **52**, 165–187.

BRÜHWILER, T., GOUDEMAND, N., GALFETTI, T., BUCHER, H., BAUD, A., WARE, D., HERMANN, E., HOCHULI, P. A. and MARTINI, R. 2009. The Lower Triassic sedimentary and carbon isotope records from Tulong (South Tibet) and their significance for Tethyan palaeoceanography. *Sedimentary Geology*, **222**, 314–332.

BRÜHWILER, T., BUCHER, H., BRAYARD, A. and GOUDEMAND, N. 2010. High-resolution biochronology and diversity dynamics of the Early Triassic ammonoid recovery: the Smithian faunas of the Northern Indian Margin. *Palaeogeography, Palaeoclimatology, Palaeoecology*, **297**, 491–501.

BRÜHWILER, T., BUCHER, H., GOUDEMAND, N. and GALFETTI, T. 2012. Smithian (Early Triassic) ammonoid faunas from Exotic Blocks from Oman: taxonomy and biochronology. *Palaeontographica Abteilung – Palaozoologie-Stratigraphie*, **296**, 3–107.

BUDUROV, K. J. 1994. *Borinella* Budurov & Stefanov nomen novum for the Triassic conodont genus *Kozurella* Budurov & Sudar 1993. *Geologica Balcanica*, **24** (3), 30.

BUDUROV, K. J. and SUDAR, M. N. 1993. Kozurella gen. n. (Conodonta) from the Olenekian (Early Triassic). *Geologica Balcanica*, **23**, 24.

BURYI, G. I. 1979. *Nizhnetriasovye konodonty yuzhnogo Primorya. [Lower Triassic conodonts of the South Primorye]*. Nauk, Moscow, 144 pp. [in Russian]

BURYI, G. I. 1997. Triassic conodont biostratigraphy of the Sikhote-Alin. *Mémoires de Géologie (Lausanne)*, **30**, 45–60.

CARR, T. R., PAULL, R. K. and CLARK, D. L. 1984. Conodont paleoecology and biofacies analysis of the Lower Triassic Thaynes Formation in the Cordilleran Miogeocline. *Geological Society of America Special Papers*, **196**, 283–294.

CHEN, Y., TWITCHETT, R. J., JIANG, H., RICHOZ, S., LAI, X., YAN, C., SUN, Y., LIU, X. and WANG, L. 2013. Size variation of conodonts during the Smithian–Spathian (Early Triassic) global warming event. *Geology*, **41**, 823–826.

CHEN, Y., JIANG, H., LAI, X., YAN, C., RICHOZ, S., LIU, X. and WANG, L. 2015. Early Triassic conodonts of Jiarong, Nanpanjiang Basin, southern Guizhou Province, South China. *Journal of Asian Earth Sciences*, **105**, 104–121.

CHEN, Y., KOLAR-JURKOVŠEK, T., JURKOVŠEK, B., ALJINOVIĆ, D. and RICHOZ, S. 2016. Early Triassic conodonts and carbonate carbon isotope record of the Idrija–Žiri area, Slovenia. *Palaeogeography, Palaeoclimatology, Palaeoecology*, **444**, 84–100.

CHEN, Y., RICHOZ, S., KRYSTYN, L. and ZHANG, Z. 2019. Quantitative stratigraphic correlation of Tethyan conodonts across the Smithian–Spathian (Early Triassic) extinction event. *Earth-Science Reviews*, **195**, 37–51.

CHEN, Y., JOACHIMSKI, M. M., RICHOZ, S., KRYSTYN, L., ALJINOVIĆ, D., SMIRČIĆ, D., KOLAR-JURKOVŠEK, T., LAI, X. and ZHANG, Z. 2021. Smithian and Spathian (Early Triassic) conodonts from Oman and Croatia and their depth habitat revealed. *Global & Planetary Change*, **196**, 103362.

CHHABRA, N. L. and SAHNI, A. 1980. Late Lower Triassic and early Middle Triassic conodont faunas from Kashmir and Kumaun sequences in Himalaya. *Journal of the Palaeontological Society of India*, **25**, 135–147.

CLARK, D. L. 1972. Early Permian crisis and its bearing on Permo-Triassic taxonomy. *Geologica et Paleontologica*, **1**, 147–158.

CLARK, D. L. and MOSHER, L. C. 1966. Stratigraphic, geographic, and evolutionary development of the conodont genus Gondolella. *Journal of Paleontology*, **40**, 376–394.

CLARK, D. L., SINCAVAGE, J. P. and STONE, D. D. 1964. New conodont from the Lower Triassic of Nevada. *Journal of Paleontology*, **38**, 375–377.

CLARKSON, M. O., RICHOZ, S., WOOD, R. A., MAURER, F., KRYSTYN, L., MCGURTY, D. J. and ASTRATTI, D. 2013. A new high-resolution δ13C record for the Early Triassic: insights from the Arabian Platform. *Gondwana Research*, **24**, 233–242.

CLARKSON, M. O., KASEMANN, S. A., WOOD, R. A., LENTON, T. M., DAINES, S. J., RICHOZ, S., OHNEMUELLER, F., MEIXNER, A., POULTON, S. W. and TIPPER, E. T. 2015. Ocean acidification and the Permo-Triassic mass extinction. *Science*, **348**, 229–232.

CLARKSON, M. O., WOOD, R. A., POULTON, S. W., RICHOZ, S., NEWTON, R. J., KASEMANN, S. A., BOWYER, F. and KRYSTYN, L. 2016. Dynamic anoxic ferruginous conditions during the end-Permian mass extinction and recovery. *Nature Communications*, **7** (1), 12236.

DAGIS, A. A. 1984. Early Triassic conodonts of northern Middle Siberia. *Academy of Sciences of the USSR, Siberian Branch. Institute of Geology & Geophysics Transactions*, **554**, 1–69.

DAUFRESNE, M., LENGFELLNER, K. and SOMMER, U. 2009. Global warming benefits the small in aquatic ecosystems. *Proceedings of the National Academy of Sciences*, **106**, 12788–12793.

DAVIES, R. B. and SIMMONS, M. D. 2018. Triassic sequence stratigraphy of the Arabian Plate. 101–162. *In* PÖPPELREITER, M. C. (ed.) *Lower Triassic to Middle Jurassic Sequence of the Arabian Plate*. EAGE Publications.

DINGLE, H. and DRAKE, V. A. 2007. What is migration? *Bioscience*, **57**, 113–121.

DONOGHUE, P. C., PURNELL, M. A., ALDRIDGE, R. J. and ZHANG, S. 2008. The interrelationships of 'complex' conodonts (Vertebrata). *Journal of Systematic Palaeontology*, **6**, 119–153.

DURKOOP, A., RICHTER, D. K. and STRITZKE, R. 1986. Fazies, Alter und Korrelation der triadischen Rotkalke von Epidauros, Adhami und Hydra (Griechenland). *Facies*, **14**, 105–150.

DZIK, J. 1976. Remarks on the evolution of Ordovician conodonts. *Acta Palaeontologica Polonica*, **21**, 395–455.

EICHENBERG, W. 1930. Conodonten aus dem Culm des Harzes. *Palaeontologische Zeitschrift*, **12**, 177–182.

FRIESENBICHLER, E., HAUTMANN, M., GRĂDINARU, E. and BUCHER, H. 2019. A highly diverse bivalve fauna from a Bithynian (Anisian, Middle Triassic) *Tubiphytes*-microbial buildup in North Dobrogea (Romania). *Papers in Palaeontology*, **7**, 447–495.

GALFETTI, T., BUCHER, H., OVTCHAROVA, M., SCHALTEGGER, U., BRAYARD, A., BRÜHWILER, T., GOUDEMAND, N., WEISSERT, H., HOCHULI, P., CORDEY, F. and GUODON, K. 2007*a*. Timing of the Early Triassic carbon cycle perturbations inferred from new U-Pb ages and ammonoid biochronozones. *Earth & Planetary Science Letters*, **258**, 593–604.

GALFETTI, T., BUCHER, H., BRAYARD, A., HOCHULI, P. A., WEISSERT, H., GUODUN, K., ATUDOREI, V. and GUEX, J. 2007*b*. Late Early Triassic climate change: insights from carbonate carbon isotopes, sedimentary evolution and ammonoid paleobiogeography. *Palaeogeography, Palaeoclimatology, Palaeoecology*, **243**, 394–411.

GALFETTI, T., BUCHER, H., MARTINI, R., HOCHULI, P. A., WEISSERT, H., CRASQUIN-SOLEAU, S., BRAYARD, A., GOUDEMAND, N., BRÜHWILER, T. and GUODUN, K. 2008. Evolution of Early Triassic outer platform paleoenvironments in the Nanpanjiang Basin (South China) and their significance for the biotic recovery. *Sedimentary Geology*, **204**, 36–60.

GOEL, R. K. 1977. Triassic conodonts from Spiti (Himachal Pradesh), India. *Journal of Paleontology*, **51**, 1085–1101.

GOLDING, M. L. 2021. Abundant conodont faunas from the Olenekian (Early Triassic) of subsurface British Columbia, Canada and diversification of the Neogondolellinae around

the Smithian–Spathian boundary. *Global & Planetary Change*, **205**, 103613.

GOLDING, M. L. and ORCHARD, M. J. 2018. *Magnigondolella*, a new conodont genus from the Triassic of North America. *Journal of Paleontology*, **92**, 207–220.

GOUDEMAND, N., ORCHARD, M. J., TAFFOREAU, P., URDY, S., BRUEHWILER, T., BRAYARD, A., GALFETTI, T. and BUCHER, H. 2012*a*. Early Triassic conodont clusters from South China: revision of the architecture of the 15 element apparatuses of the superfamily Gondolelloidea. *Palaeontology*, **55**, 1021–1034.

GOUDEMAND, N., ORCHARD, M. J., BUCHER, H. and JENKS, J. 2012*b*. The elusive origin of *Chiosella timorensis* (Conodont Triassic). *Geobios*, **45**, 199–207.

GOUDEMAND, N., ROMANO, C., LEU, M., BUCHER, H., TROTTER, J. A. and WILLIAMS, I. S. 2019. Dynamic interplay between climate and marine biodiversity upheavals during the early Triassic Smithian–Spathian biotic crisis. *Earth-Science Reviews*, **195**, 169–178.

GRASBY, S. E., BEAUCHAMP, B., BOND, D. P., WIGNALL, P. B. and SANEI, H. 2016. Mercury anomalies associated with three extinction events (Capitanian crisis, latest Permian extinction and the Smithian/Spathian extinction) in NW Pangea. *Geological Magazine*, **153**, 285–297.

GUEX, J. 1991. *Biochronological correlations*. Springer, 252 pp.

HAMMER, Ø., HARPER, D. A. and RYAN, P. D. 2001. PAST: paleontological statistics software package for education and data analysis. *Palaeontologia Electronica*, **4** (1), 9.

HAMMER, O., HARPER, D. A. T. and RYAN, P. D. 2012. PAST: paleontological statistics, version 2.17. https://www.yumpu.com/s/YX7bqZwTr31U9Z9p

HAMMER, Ø., JONES, M. T., SCHNEEBELI-HERMANN, E., HANSEN, B. B. and BUCHER, H. 2019. Are Early Triassic extinction events associated with mercury anomalies? A reassessment of the Smithian/Spathian boundary extinction. *Earth-Science Reviews*, **195**, 179–190.

HASENMUELLER, W. A. 1970. Conodont biostratigraphy of the Lower Triassic Thaynes Formation of the Confusion Range, west-central Utah. PhD thesis, Ohio State University, USA.

HATLEBERG, E. W. and CLARK, D. L. 1984. Lower Triassic conodonts and biofacies interpretations: Nepal and Svalbard. *Geologica et Palaeontologica*, **18**, 101–125.

HAUSER, M., VACHARD, D., MARTINI, R., MATTER, A., PETERS, T. and ZANINETTI, L. 2000. The Permian sequence reconstructed from reworked carbonate clasts in the Batain Plain (Northeastern Oman). *Comptes Rendus de l'Académie des Sciences – Series IIA – Earth & Planetary Science*, **330**, 273–279.

HAUSER, M., MARTINI, R., BURNS, S., DUMITRICA, P., KRYSTYN, L., MATTER, A., PETERS, T. and ZANINETTI, L. 2001. Triassic stratigraphic evolution of the Arabian-Greater India embayment of the southern Tethys margin. *Eclogae Geologicae Helvetiae*, **94**, 29–62.

HAUSER, M., MARTINI, R., MATTER, A., KRYSTYN, L., PETERS, T., STAMPFLI, G. and ZANINETTI, L. 2002. The break-up of East Gondwana along the northeast coast of Oman: evidence from the Batain basin. *Geological Magazine*, **139**, 145–157.

HAUTMANN, M., BAGHERPOUR, B., BROSSE, M., FRISK, Å., HOFMANN, R., BAUD, A., NÜTZEL, A., GOUDEMAND, N. and BUCHER, H. 2015. Competition in slow motion: the unusual case of benthic marine communities in the wake of the end-Permian mass extinction. *Palaeontology*, **58**, 871–901.

HENDERSON, C. M., GOLDING, M. L. and ORCHARD, M. J. 2018. Conodont sequence biostratigraphy of the Lower Triassic Montney Formation. *Bulletin of Canadian Petroleum Geology*, **66**, 7–22.

HILTING, A. K., KUMP, L. R. and BRALOWER, T. J. 2008. Variations in the oceanic vertical carbon isotope gradient and their implications for the Paleocene–Eocene biological pump. *Paleoceanography & Paleoclimatology*, **23**, PA3222.

HIRSCH, F. 1994. Triassic conodonts as ecological and eustatic sensors. 949–959. *In* EMBRY, A. F., BEAUCHAMP, B. and GLASS, D. J. (eds) *Pangea: Global environments and resources*. Canadian Society of Petroleum Geologists, Memoir 17.

HOFFMANN, M., KOŁODZIEJ, B. and SKUPIEN, P. 2017. Microencruster-microbial framework and synsedimentary cements in the Štramberk Limestone (Carpathians, Czech Republic): insights into reef zonation. *Annales Societatis Geologorum Poloniae*, **87**, 325–347.

HUCKRIEDE, R. 1958. Die Conodonten der Mediterranen Trias und ihr stratigraphischer Wert. *Paläontologische Zeitschrift*, **32**, 141–175.

IMMENHAUSER, A. M., SCHREURS, G., PETERS, T., MATTER, A., HAUSER, M. and DUMITRICA, P. 1998. Stratigraphy, sedimentology and depositional environments of the Permian to uppermost Cretaceous Batain Group. *Eclogae Geologicae Helvetiae*, **91**, 217–236.

ISHIDA, K. and HIRSCH, F. 2011. The Triassic conodonts of the NW Malayan Kodiang Limestone revisited: taxonomy and paleogeographic significance. *Gondwana Research*, **19**, 22–36.

JEPPSSON, L. and ANEHUS, R. 1999. A new technique to separate conodont elements from heavier minerals. *Alcheringa*, **23**, 57–62.

JEPPSSON, L., ANEHUS, R. and FREDHOLM, D. 1999. The optimal acetate buffered acetic acid technique for extracting phosphatic fossils. *Journal of Paleontology*, **73**, 964–972.

JI, W., TONG, J., ZHAO, L., ZHOU, S. and CHEN, J. 2011. Lower–Middle Triassic conodont biostratigraphy of the Qingyan section, Guizhou province, Southwest China. *Palaeogeography, Palaeoclimatology, Palaeoecology*, **308**, 213–223.

JOACHIMSKI, M. M., LAI, X., SHEN, S., JIANG, H., LUO, G., CHEN, B., CHEN, J. and SUN, Y. 2012. Climate warming in the latest Permian and the Permian–Triassic mass extinction. *Geology*, **40**, 195–198.

KILIC, A. M. 2016. A new pelagic conodont taxon of the Central Pontides (Turkey). *Turkish Journal of Earth Sciences*, **25**, 456–466.

KLAPPER, G. and PHILIP, G. M. 1972. Familial classification of reconstructed Devonian conodont apparatuses. *Geologica et Palaeontologica*, **1**, 97–113.

KLETS, T. V. 2008. Paleogeographic regionalization of Triassic seas based on conodontophorids. *Stratigraphy & Geological Correlation*, **16**, 467–489.

KLETS, T. V. and KOPYLOVA, A. V. 2006. First finds of Triassic conodonts in northeaster Asia. *News of Paleontology & Stratigraphy Applied Russian Geology & Geophysics*, **47**, 95–105.

KOIKE, T. 1981. Biostratigraphy of Triassic conodonts in Japan. *Science Reports of the Yokohama National University, Section 2*, **38**, 53–69.

KOIKE, T. 1992. Morphological variation in Spathian conodont *Spathoicriodus collinsoni* (Solien) from the Taho Limestone, Japan. 355–364. *In* ISHIZAKI, K. and SAITŌ, T. (eds) *Centenary of Japanese micropaleontology: Contributed papers in honor of Professor Yokichi Takayanagi*. Terra Scientific Publishing Company.

KOIKE, T. 1996. The first occurrence of Griesbachian conodonts in Japan. *Transactions & Proceedings of the Paleontological Society of Japan. New Series*, **181**, 337–346.

KOIKE, T. 2004. Early Triassic Neospathodus (Conodonta) apparatuses from the Taho Formation, southwest Japan. *Paleontological Research*, **8**, 129–140.

KOIKE, T. 2016. Multielement conodont apparatuses of the Ellisonidae from Japan. *Paleontological Research*, **20**, 161–175.

KOIKE, T., YAMAKITA, S. and KADOTA, N. 2004. A natural assemblage of *Ellisonia* sp. cf. *E. triassica* Müller (Vertebrata: Conodonta) from the uppermost Permian in the Suzuka Mountains, central Japan. *Paleontological Research*, **8**, 241–253.

KOMATSU, T., TAKASHIMA, R., SHIGETA, Y., MAEKAWA, T., TRAN, H. D., CONG, T. D., SAKATA, S., DINH, H. D. and TAKAHASHI, O. 2016. Carbon isotopic excursions and detailed ammonoid and conodont biostratigraphies around Smithian–Spathian boundary in the Bac Thuy Formation, Vietnam. *Palaeogeography, Palaeoclimatology, Palaeoecology*, **454**, 65–74.

KORTE, C. and KOZUR, H. W. 2010. Carbon-isotope stratigraphy across the Permian–Triassic boundary: a review. *Journal of Asian Earth Sciences*, **39**, 215–235.

KOVÁCS, V. S. and KOZUR, H. 1980. Stratigraphische Reichweite der wichtigsten conodonten (ohne Zahnreihenconodonten) der Mittel- und Obertrias. *Geologische und Paläontologische Mitteilungen Innsbruck*, **10**, 47–78.

KOZUR, H. 1988. Division of the gondolellid platform conodonts. 244–245. *In* ZIEGLER, W. (ed.) *1st International Senckenberg Conference and 5th European Conodont Symposium (ECOS V). Contributions I. Part 2*. Courier Forschungsinstitut Senckenberg, vol. **102**.

KOZUR, H. 1989. The taxonomy of the gondolellid conodonts in the Permian and Triassic. 409–469. *In* ZIEGLER, W. (ed.) *1st International Senckenberg Conference and 5th European Conodont Symposium (ECOS V). Contributions III. Papers on Ordovician to Triassic Conodonts*. Courier Forschungsinstitut Senckenberg, vol. **117**.

KOZUR, H. 1994. *Chengyuania*, a new name for *Pseudogondolella* Kozur 1988 (Conodonta) [non *Pseudogondolella* Yang 1984 (hybodont fish teeth)]. *Paläontologische Zeitschrift*, **68**, 529–530.

KOZUR, H. and MOSTLER, H. 1976. Neue Conodonten aus dem Jungpaläozoikum und der Trias. *Geologische und Paläontologische Mitteilungen Innsbruck*, **6**, 1–33.

KOZUR, H. W., MOSTLER, H. and KRAINER, K. 1998. *Sweetospathodus* n. gen. and *Triassospathodus* n. gen., two important Lower Triassic conodont genera. *Geologia Croatica*, **51**, 1–5.

KRAHL, J., KAUFFMANN, G., KOZUR, H., RICHTER, D., FÖRSTER, O. and HEINRITZI, F. 1983. Neue Daten zur Biostratigraphie und zur tektonischen Lagerung der Phyllit-Gruppe und der Trypali-Gruppe auf der Insel Kreta (Griechenland). *Geologische Rundschau*, **72**, 1147–1166.

KRYSTYN, L., OM, N. B. and DEVENDRA, K. B. 2005. Muth (Spiti, Indian Himalaya): a candidate Global Stratigraphic Section and Point (GSSP) for the base of the Olenekian Stage. *Albertiana*, **33**, 51–53.

KRYSTYN, L., RICHOZ, S., BAUD, A. and TWITCHETT, R. J. 2003. A unique Permian–Triassic boundary section from the neotethyan Hawasina basin, Central Oman Mountains. *Palaeogeography, Palaeoclimatology, Palaeoecology*, **191**, 329–344.

LAI, X., WIGNALL, P. and ZHANG, K. 2001. Palaeoecology of the conodonts *Hindeodus* and *Clarkina* during the Permian–Triassic transitional period. *Palaeogeography, Palaeoclimatology, Palaeoecology*, **171**, 63–72.

LEHRMANN, D. J., STEPCHINSKI, L., ALTINER, D., ORCHARD, M. J., MONTGOMERY, P., ENOS, P., ELLWOOD, B. B., BOWRING, S. A., RAMEZANI, J., WANG, H., WEI, J., YU, M., GRIFFITHS, J. D., MINZONI, M., SCHAAL, E. K., LI, X., MEYER, K. M. and PAYNE, J. 2015. An integrated biostratigraphy (conodonts and foraminifers) and chronostratigraphy (paleomagnetic reversals, magnetic susceptibility, elemental chemistry, carbon isotopes and geochronology) for the Permian–Upper Triassic strata of Guandao section, Nanpanjiang Basin, south China. *Journal of Asian Earth Sciences*, **108**, 117–135.

LEU, M., BUCHER, H. and GOUDEMAND, N. 2019. Clade-dependent size response of conodonts to environmental changes during the late Smithian extinction. *Earth-Science Reviews*, **195**, 52–67.

LEU, M., BUCHER, H., VENNEMANN, T., BAGHERPOUR, B., CHENG, J., BROSSE, M. and GOUDEMAND, N. 2022. A unitary association-based conodont biozonation of the Smithian–Spathian boundary (Early Triassic) and associated biotic crisis from South China. *Swiss Journal of Palaeontology*, **141**, 19.

LEU, M., BUCHER, H., BAUD, A., VENNEMANN, T., LUZ, Z., HAUTMANN, M. and GOUDEMAND, N. 2023. Data from: An expanded Smithian–Spathian (Early Triassic) boundary from a reefal build-up record in Oman: implications for conodont taxonomy, high-resolution biochronology and the carbon isotope record. *Dryad Digital Repository*. https://doi.org/10.5061/dryad.37pvmcvp6

LI, H., JIANG, H., CHEN, Y., WIGNALL, P. B., WU, B., ZHANG, Z., ZHANG, M., OUYANG, Z. and LAI, X. 2019. Smithian platform-bearing gondolellid conodonts from Yiwagou Section, northwestern China and implications for their geographic distribution in the Early Triassic. *Journal of Paleontology*, **93**, 496–511.

LIANG, D., TONG, J. and ZHAO, L. 2011. Lower Triassic Smithian–Spathian Boundary at West Pingdingshan Section in Chaohu, Anhui Province. *Science China Earth Sciences*, **54**, 372–379.

LINDSTRÖM, M. 1970. A suprageneric taxonomy of the conodonts. *Lethaia*, **3**, 427–445.

LIU, S., SUN, Z., JI, C., ZHOU, M. and JIANG, D. 2020. Conodont biostratigraphy and age of the Early Triassic fish-bearing-nodule levels from Nanjing and Jurong, Jiangsu Province, South China. *Journal of Earth Science*, **31**, 9–22.

LUCAS, S. and ORCHARD, M. J. 2007. Triassic lithostratigraphy and biostratigraphy north of Currie, Elko County, Nevada. *Triassic of the American West: New Mexico Museum of Natural History & Science Bulletin*, **40**, 119–126.

MAEKAWA, T. and JENKS, J. F. 2021. Smithian (Olenekian, Early Triassic) conodonts from ammonoid-bearing limestone blocks at Crittenden Springs, Elko County, Nevada, USA. *Paleontological Research*, **25**, 201–245.

MAEKAWA, T., KOMATSU, T. and KOIKE, T. 2018. Early Triassic conodonts from the Tahogawa Member of the Taho Formation, Ehime Prefecture, Southwest Japan. *Paleontological Research*, **22** (Suppl. 1), 1–62.

MATSUDA, T. 1983. Early Triassic conodonts from Kashmir, India part 3: *Neospathodus* 2. *Journal of Geosciences Osaka City University*, **26**, 87–110.

MATSUDA, T. 1984. Early Triassic conodonts from Kashmir, India part 4: *Gondolella* and *Platyvillosus*. *Journal of Geosciences Osaka City University*, **27**, 119–141.

METCALFE, I. 1990. Triassic conodont biostratigraphy in the Malay Peninsula. *Bulletin of the Geological Society of Malaysia*, **26**, 133–145.

METCALFE, I., NICOLL, R. S., WILLINK, R., LADJAVADI, M. and GRICE, K. 2013. Early Triassic (Induan–Olenekian) conodont biostratigraphy, global anoxia, carbon isotope excursions and environmental perturbations: new data from Western Australian Gondwana. *Gondwana Research*, **23**, 1136–1150.

MEYER, K. M., YU, M., JOST, A. B., KELLEY, B. M. and PAYNE, J. L. 2011. δ13C evidence that high primary productivity delayed recovery from end-Permian mass extinction. *Earth & Planetary Science Letters*, **302**, 378–384.

MONNET, C. and BUCHER, H. 2002. Cenomanian (early Late Cretaceous) ammonoid faunas of Western Europe. Part I: biochronology (unitary associations) and diachronism of datums. *Eclogae Geologicae Helvetiae*, **95**, 57–74.

MOSHER, L. C. 1968. Triassic conodonts from western North America and Europe and their correlation. *Journal of Paleontology*, **42**, 895–946.

MOSHER, L. C. 1973. Triassic conodonts from British Columbia and the northern Arctic Islands. *Contributions to Canadian Paleontology, Geological Survey of Canada, Bulletin*, **222**, 141–193.

MÜLLER, K. J. 1956. Triassic conodonts from Nevada. *Journal of Paleontology*, **30**, 818–830.

MÜLLER, K. J. 1962. Zur systematischen Einteilung der Conodontophorida. *Paläontologische Zeitschrift*, **36**, 109–117.

NAKREM, H. A., ORCHARD, M. J., WEITSCHAT, W., HOUNSLOW, M. W., BEATTY, T. W. and MØRK, A. 2008. Triassic conodonts from Svalbard and their Boreal correlations. *Polar Research*, **27**, 523–539.

NOGAMI, Y. 1968. Trias-Conodonten von Timor, Malaysien und Japan. *Memoirs of the Faculty of Science, Kyoto University, Series of Geology & Mineralogy*, **34**, 115–136.

ORCHARD, M. J. 1995. Taxonomy and correlation of Lower Triassic (Spathian) segminate conodonts from Oman and revision of some species of *Neospathodus*. *Journal of Paleontology*, **69**, 110–122.

ORCHARD, M. J. 1996. Conodont fauna from the Permian–Triassic boundary: observations and reservations. *Permophiles*, **28**, 29–35.

ORCHARD, M. J. 2005. Multielement conodont apparatuses of Triassic Gondolelloidea. *Special Papers in Palaeontology*, **73**, 73–101.

ORCHARD, M. J. 2007. Conodont diversity and evolution through the latest Permian and Early Triassic upheavals. *Palaeogeography, Palaeoclimatology, Palaeoecology*, **252**, 93–117.

ORCHARD, M. J. 2008. Lower Triassic conodonts from the Canadian Arctic, their intercalibration with ammonoid-based stages and a comparison with other North American Olenekian faunas. *Polar Research*, **27**, 393–412.

ORCHARD, M. J. 2010. Triassic conodonts and their role in stage boundary definition. *Geological Society, London, Special Publications*, **334**, 139–161.

ORCHARD, M. J. 2021. North American Spathian (upper Olenekian, Lower Triassic) neogondolellin conodonts. *Papers in Palaeontology*, **8**, e1409.

ORCHARD, M. J. and ZONNEVELD, J. P. 2009. The Lower Triassic Sulphur Mountain Formation in the Wapiti Lake area: lithostratigraphy, conodont biostratigraphy, and a new biozonation for the lower Olenekian (Smithian) Earth Science Sector (ESS) Contribution 20080714. *Canadian Journal of Earth Sciences*, **46**, 757–790.

ORCHARD, M. J., LEHRMANN, D. J., WEI, J., WANG, H. and TAYLOR, H. J. 2007*a*. Conodonts from the Olenekian-Anisian boundary beds, Guandao, Guizhou Province, China. *New Mexico Museum of Natural History & Science Bulletin*, **41**, 347–354.

ORCHARD, M., GRADINARU, E. and NICORA, A. 2007*b*. A summary of the conodont succession around the Olenekian-Anisian boundary at Deşli Caira, North Dobrogea, Romania. *New Mexico Museum of Natural History & Science Bulletin*, **41**, 341–346.

OVTCHAROVA, M., GOUDEMAND, N., HAMMER, Ø., GUODUN, K., CORDEY, F., GALFETTI, T., SCHALTEGGER, U. and BUCHER, H. 2015. Developing a strategy for accurate definition of a geological boundary through radio-isotopic and biochronological dating: the Early–Middle Triassic boundary (South China). *Earth-Science Reviews*, **146**, 65–76.

PAYNE, J. L., LEHRMANN, D. J., WEI, J., ORCHARD, M. J., SCHRAG, D. P. and KNOLL, A. H. 2004. Large perturbations of the carbon cycle during recovery from the end-Permian extinction. *Science*, **305**, 506–509.

PERRI, M. C. and ANDRAGHETTI, M. 1987. Permian–Triassic boundary and Early Triassic conodonts from the southern Alps, Italy. *Rivista Italiana di Paleontologia e Stratigrafia*, **93**, 291–328.

PETERS, T., AL-BATTASHY, M., BLÄSI, H., HAUSER, M., IMMENHAUSER, A., MOSER, L. and AL-RAJHI, A. 2001. Geological map of Sur and Al Ashkharah, Sheet NF 40-8F and Sheet NF 40-12C, Scale 1: 100,000, explanatory

notes. Sultanate of Oman Ministry of Commerce & Industry, Directorate General of Minerals.

PILLEVUIT, A. 1993. Les blocs exotiques du Sultanat d'Oman: evolution paléogéographique d'une marge passive flexurale. *Mémoires de Géologie, Lausanne*, **17**, 1–249.

PILLEVUIT, A., MARCOUX, J., STAMPFLI, G. and BAUD, A. 1997. The Oman exotics: a key to the understanding of the Neotethyan geodynamic evolution. *Geodinamica Acta*, **10**, 209–238.

PURNELL, M. A., DONOGHUE, P. C. and ALDRIDGE, R. J. 2000. Orientation and anatomical notation in conodonts. *Journal of Paleontology*, **74**, 113–122.

QIU, X., XU, Y., CHEN, Z. Q., BENTON, M. J., WEN, W., HUANG, Y. and WU, S. 2019. The Early Triassic Jurong fish fauna, South China: age, anatomy, taphonomy, and global correlation. *Global & Planetary Change*, **180**, 33–50.

RICHOZ, S. 2006. Stratigraphie et variations isotopiques du carbone dans le Permien supérieur et le Trias inférieur de quelques localités de la Néotéthys (Turquie, Oman et Iran). *Mémoires de Géologie, Lausanne*, **46**, 1–251.

RICHOZ, S., BAUD, A., KRYSTYN, L., TWITCHETT, R. and MARCOUX, J. 2005. Permo-Triassic deposits of the Oman Mountains: from basin and slope to the shallow platform. International Association of Sedimentology 24th Regional Meeting: Post-conference excursion no. A13 in the Oman Mountains.

RICHOZ, S., KRYSTYN, L., BAUD, A., BRANDNER, R., HORACEK, M. and MOHTAT-AGHAI, P. 2010*a*. Permian–Triassic boundary interval in the Middle East (Iran and N. Oman): progressive environmental change from detailed carbonate carbon isotope marine curve and sedimentary evolution. *Journal of Asian Earth Sciences*, **39**, 236–253.

RICHOZ, S., KRYSTYN, L., WEIDLICH, O., BAUD, A., BEAUCHAMP, B., BERNECKER, M., CORDEY, F., GRASBY, S., HENDERSON, C., MARCOUX, J. and NICORA, A. 2010*b*. The Permian-Triassic transition in the Oman Mountains: transect of the Tethyan margin from shallow to deepwater deposits. IGCP 572 Field Guide Book 2, 109 pp. https://hal.archives-ouvertes.fr/hal-03276240

RICHOZ, S., BAUD, A., BEAUCHAMP, B., GRASBY, S. E., HENDERSON, C. M. and KRYSTYN, L. 2014. Khuff Margin: slope to oceanic deposits (Permian-Triassic allochthons and exotics, Oman). 55–76. *In* PÖPPELREITER, M. (ed.) *Permo-Triassic sequence of the Arabian Plate*. EAGE Publications.

RICOU, L. E. 1994. Tethys reconstructed: plates, continental fragments and their boundaries since 260 Ma from Central America to South-eastern Asia. *Geodinamica Acta*, **7**, 169–218.

ROGER, J., BÉCHENNEC, F., JANJOU, D., LE MÉTOUR, J., WYNS, R. and BEURRIER, M. 1991. Geological map of Ja'alan with explanatory notes. Sheet NF 40-8E, scale 1:100,000. Ministry of Petroleum & Minerals, Muscat, Oman.

ROMANO, C., GOUDEMAND, N., VENNEMANN, T. W., WARE, D., SCHNEEBELI-HERMANN, E., HOCHULI, P. A., BRÜHWILER, T., BRINKMANN, W. and BUCHER, H. 2013. Climatic and biotic upheavals following the end-Permian mass extinction. *Nature Geoscience*, **6**, 57–60.

RUSSO, F., GAUTRET, P., MASTANDREA, A. and PERRI, E. 2006. Syndepositional cements associated with nannofossils in the Marmolada Massif: evidences of microbially mediated primary marine cements? (Middle Triassic, Dolomites, Italy). *Sedimentary Geology*, **185**, 267–275.

SCHNEEBELI-HERMANN, E., BAGHERPOUR, B., VENNEMANN, T., LEU, M. and BUCHER, H. 2020. Sedimentary organic matter from a cored Early Triassic succession, Georgetown (Idaho, USA). *Swiss Journal of Palaeontology*, **139**, 5.

SCHREURS, G. and IMMENHAUSER, A. 1999. West-northwest directed obduction of the Batain Group on the eastern Oman continental margin at the Cretaceous–Tertiary boundary. *Tectonics*, **18**, 148–160.

SHACKLETON, R. M., RIES, A. C., BIRD, P. R., FILBRANDT, J. B., LEE, C. W. and CUNNINGHAM, G. C. 1990. The Batain Melange of NE Oman. *Geological Society, London, Special Publications*, **49**, 673–696.

SHEN, J., SCHOEPFER, S. D., FENG, Q., ZHOU, L., YU, J., SONG, H., WEI, H. and ALGEO, T. J. 2015. Marine productivity changes during the end-Permian crisis and Early Triassic recovery. *Earth-Science Reviews*, **149**, 136–162.

SHERIDAN, J. A. and BICKFORD, D. 2011. Shrinking body size as an ecological response to climate change. *Nature Climate Change*, **1**, 401–406.

SHIGETA, Y., ZAKHAROV, Y. D., MAEDA, H. and POPOV, A. M. (eds) 2009. The Lower Triassic System in the Abrek Bay Area, South Primorye, Russia. *National Museum of Nature & Science Monographs*, **38**, 1–218.

SHIGETA, Y., KOMATSU, T., MAEKAWA, T. and HUYEN, D. T. (eds) 2014. Olenekian (Early Triassic) stratigraphy and fossil assemblages in northeastern Vietnam. *National Museum of Nature & Science Monographs*, **45**, 1–309.

SOLIEN, M. A. 1979. Conodont biostratigraphy of the Lower Triassic Thaynes Formation, Utah. *Journal of Paleontology*, **53**, 276–306.

SONG, H., TONG, J., ALGEO, T. J., HORACEK, M., QIU, H., SONG, H., TIAN, L. and CHEN, Z. Q. 2013. Large vertical δ13CDIC gradients in Early Triassic seas of the South China craton: implications for oceanographic changes related to Siberian Traps volcanism. *Global & Planetary Change*, **105**, 7–20.

SONG, H., WIGNALL, P. B., CHU, D., TONG, J., SUN, Y., SONG, H., HE, W. and TIAN, L. 2014. Anoxia/high temperature double whammy during the Permian–Triassic marine crisis and its aftermath. *Scientific Reports*, **4**, 4132.

SONG, H., DU, Y., ALGEO, T. J., TONG, J., OWENS, J. D., SONG, H., TIAN, L., QIU, H., ZHU, Y. and LYONS, T. W. 2019. Cooling-driven oceanic anoxia across the Smithian/Spathian boundary (mid-Early Triassic). *Earth-Science Reviews*, **195**, 133–146.

SOUQUET, L. and GOUDEMAND, N. 2020. Exceptional basal-body preservation in some Early Triassic conodont elements from Oman. *Palaeogeography, Palaeoclimatology, Palaeoecology*, **549**, 109066.

SPÖTL, C. and VENNEMANN, T. W. 2003. Continuous-flow isotope ratio mass spectrometric analysis of carbonate minerals. *Rapid Communications in Mass Spectrometry*, **17**, 1004–1006.

STAESCHE, U. 1964. Conodonten aus dem Skyth von Südtirol. *Neues Jahrbuch für Geologie und Paläontologie*, **119**, 246–306.

STANLEY, S. M. 2009. Evidence from ammonoids and conodonts for multiple Early Triassic mass extinctions. *Proceedings of the National Academy of Sciences*, **106**, 15264–15267.

STEBBINS, A., ALGEO, T. J., KRYSTYN, L., ROWE, H., BROOKFIELD, M., WILLIAMS, J., NYE, S. W. JR. and HANNIGAN, R. 2019. Marine sulfur cycle evidence for upwelling and eutrophic stresses during Early Triassic cooling events. *Earth-Science Reviews*, **195**, 68–82.

SUN, Y., JOACHIMSKI, M. M., WIGNALL, P. B., YAN, C., CHEN, Y., JIANG, H., WANG, L. and LAI, X. 2012. Lethally hot temperatures during the Early Triassic greenhouse. *Science*, **338**, 366–370.

SUN, Y. D., WIGNALL, P. B., JOACHIMSKI, M. M., BOND, D. P. G., GRASBY, S. E., SUN, S., YAN, C. B., WANG, L. N., CHEN, Y. L. and LAI, X. L. 2015. High amplitude redox changes in the late Early Triassic of South China and the Smithian–Spathian extinction. *Palaeogeography, Palaeoclimatology, Palaeoecology*, **427**, 62–78.

SUN, Z. Y., LIU, S., JI, C., JIANG, D. Y. and ZHOU, M. 2020*a*. Gondolelloid multielement conodont apparatus (*Scythogondolella*) from the Lower Triassic of Jiangsu, East China, revealed by high-resolution X-ray microtomography. *Palaeoworld*, **30**, 286–295.

SUN, Z., LIU, S., JI, C., JIANG, D. and ZHOU, M. 2020*b*. Synchrotron-aided reconstruction of the prioniodinin multielement conodont apparatus (*Hadrodontina*) from the Lower Triassic of China. *Palaeogeography, Palaeoclimatology, Palaeoecology*, **560**, 109913.

SUN, Y. D., RICHOZ, S., KRYSTYN, L., GRASBY, S. E., CHEN, Y. L., BANERJEE, D. and JOACHIMSKI, M. M. 2021. Integrated bio-chemostratigraphy of Lower and Middle Triassic marine successions at Spiti in the Indian Himalaya: implications for the Early Triassic nutrient crisis. *Global & Planetary Change*, **196**, 103363.

SWEET, W. C. 1970. Uppermost Permian and Lower Triassic conodonts of the Salt Range and Trans-Indus Ranges, West Pakistan. 207–275. *In* KUMMELL, B. and TEICHERT, C. (eds) *Stratigraphic boundary problems, Permian and Triassic of West Pakistan*, **4**. University of Kansas Press, Department of Geology, Special Publications, vol., 474 pp.

SWEET, W., MOSHER, L., CLARK, D., COLLINSON, J. and HASENMUELLER, W. 1971. Spathian conodont taxonomy and biochronology. *Palaeogeography, Palaeoclimatology, Palaeoecology*, **93**, 21–46.

THOMAZO, C., BRAYARD, A., ELMEKNASSI, S., VENNIN, E., OLIVIER, N., CARAVACA, G., ESCARGUEL, G., FARA, E., BYLUND, K. G., JENKS, J. F., STEPHEN, D. A., KILLINGSWORTH, B., SANSJOFRE, P. and CARTIGNY, P. 2019. Multiple sulfur isotope signals associated with the late Smithian event and the Smithian/Spathian boundary. *Earth-Science Reviews*, **195**, 96–113.

TIAN, C., DAI, J. and TIAN, S. G. 1983. Triassic conodonts. 345–398. *In Palaeontological atlas of Southwest China, microfossils*. Chengdu Institute of Geological and Mineralogical Research.

TOZER, E. T. and CALON, T. J. 1990. Triassic ammonoids from Jabal Safra and Wadi Alwa, Oman, and their significance. *Geological Society, London, Special Publications*, **49**, 203–211.

TROTTER, J. A., WILLIAMS, I. S., NICORA, A., MAZZA, M. and RIGO, M. 2015. Long-term cycles of Triassic climate change: a new δ18O record from conodont apatite. *Earth & Planetary Science Letters*, **415**, 165–174.

TWITCHETT, R. J., KRYSTYN, L., BAUD, A., WHEELEY, J. R. and RICHOZ, S. 2004. Rapid marine recovery after the end-Permian mass-extinction event in the absence of marine anoxia. *Geology*, **32**, 805–808.

VÉRARD, C. 2019. Plate tectonic modelling: review and perspectives. *Geological Magazine*, **156**, 208–241.

WANG, C. and WANG, Z. 1976. Triassic conodonts from the Mount Jolmo Lungma region. 387–416. *In* XIZANG SCIENTIFIC EXPEDITION TEAM OF CHINESE ACADEMY OF SCIENCES (ed.) *A report of scientific expedition in the Mount Jolmo Lungma Region (1966–1968), Paleontology*, vol., **2**. Science Press, Beijing. [in Chinese]

WEI, H., SHEN, J., SCHOEPFER, S. D., KRYSTYN, L., RICHOZ, S. and ALGEO, T. J. 2015. Environmental controls on marine ecosystem recovery following mass extinctions, with an example from the Early Triassic. *Earth-Science Reviews*, **149**, 108–135.

WEITSCHAT, W. and LEHMANN, U. 1978. Biostratigraphy of the uppermost part of the Smithian Stage (Lower Triassic) at the Botneheia, W-Spitsbergen. *Mitteilungen aus dem Geologisch-Paläontologischen Institut Universität Hamburg, Heft*, **48**, 85–100.

WIDMANN, P. 2019. Temporal calibration and quantification of Early Triassic climatic disturbances through high-precision U-Pb zircon dating and an improved chemical abrasion procedure. PhD thesis, University of Geneva.

WIDMANN, P., BUCHER, H., LEU, M., VENNEMANN, T., BAGHERPOUR, B., SCHNEEBELI-HERMANN, E., GOUDEMAND, N. and SCHALTEGGER, U. 2020. Dynamics of the largest carbon isotope excursion during the Early Triassic Biotic Recovery. *Frontiers in Earth Science*, **8**, 196.

WOODS, A. D. and BAUD, A. 2008. Anachronistic facies from a drowned Lower Triassic carbonate platform: lower member of the Alwa Formation (Ba'id Exotic), Oman Mountains. *Sedimentary Geology*, **209**, 1–14.

WU, K., TIAN, L., LIANG, L., METCALFE, I., CHU, D. and TONG, J. 2019. Recurrent biotic rebounds during the Early Triassic: biostratigraphy and temporal size variation of conodonts from the Nanpanjiang Basin, South China. *Journal of the Geological Society*, **176**, 1232–1246.

WU, K., TONG, J., METCALFE, I., LIANG, L., XIAO, Y. and TIAN, L. 2020. Quantitative stratigraphic correlation of the Lower Triassic in South China based on conodont unitary associations. *Earth-Science Reviews*, **200**, 102997.

WYNS, R., BÉCHENNEC, F., LE MÉTOUR, J., ROGER, J. and CHEVREL, S. 1992. Geological map of Sur, Sheet NF 40-08, scale 1: 250 000. Muscat, Directorate General of Minerals, Ministry of Petroleum & Minerals.

YAN, C., WANG, L., JIANG, H., WIGNALL, P. B., SUN, Y., CHEN, Y. and LAI, X. 2013. Uppermost Permian to

Lower Triassic conodonts at Bianyang section, Guizhou province, South China. *PALAIOS*, **28**, 509–522.

YAN, C., JIANG, H., LAI, X., SUN, Y., YANG, B. and WANG, L. 2015. The relationship between the "Green-Bean Rock" layers and conodont *Chiosella timorensis* and implications on defining the Early-Middle Triassic boundary in the Nanpanjiang Basin, South China. *Journal of Earth Science*, **26**, 236–245.

ZAKHAROV, Y. D. and RYBALKA, S. V. 1987. A standard for the Permian-Triassic in the Tethys. 6–48. *In* ZAKHAROV, Y. D. and ONOPRIENKO, Y. I. (eds) *Problems of the Permian-Triassic biostratigraphy of the East USSR*. DVNC AN SSSR, Vladivostok. [in Russian]

ZHANG, S. 1990. On the Lower Triassic conodont sequence of Western Guangxi. *Geoscience*, **4**, 1–17. [in Chinese with English abstract]

ZHANG, S. and YANG, Z. 1991. On multielement taxonomy of the Early Triassic conodonts. *Stratigraphy and Paleontology of China*, **1**, 17–47.

ZHANG, S., ALDRIDGE, R. J. and DONOGHUE, P. C. 1997. An Early Triassic conodont with periodic growth? *Journal of Micropalaeontology*, **16**, 65–72.

ZHANG, F., ROMANIELLO, S. J., ALGEO, T. J., LAU, K. V., CLAPHAM, M. E., RICHOZ, S., HERRMANN, A. D., SMITH, H., HORACEK, M. and ANBAR, A. D. 2018. Multiple episodes of extensive marine anoxia linked to global warming and continental weathering following the latest Permian mass extinction. *Science Advances*, **4**, e1602921.

ZHANG, L., ORCHARD, M. J., BRAYARD, A., ALGEO, T. J., ZHAO, L., CHEN, Z. Q. and LYU, Z. 2019. The Smithian/Spathian boundary (late Early Triassic): a review of ammonoid, conodont, and carbon-isotopic criteria. *Earth-Science Reviews*, **195**, 7–36.

ZHAO, L. S. 2005. Study on the Lower Triassic conodont sequence and the Induan–Olenekian Boundary in Chaohu, Anhui Province. PhD thesis, China University of Geosciences, Wuhan.

ZHAO, L., ORCHARD, M. J., TONG, J., SUN, Z., ZUO, J., ZHANG, S. and YUN, A. 2007. Lower Triassic conodont sequence in Chaohu, Anhui Province, China and its global correlation. *Palaeogeography, Palaeoclimatology, Palaeoecology*, **252**, 24–38.

ZHAO, L., TONG, J., ZHANG, S. and SUN, Z. 2008. An update of conodonts in the Induan-Olenekian boundary strata at west Pingdingshan section, Chaohu, Anhui Province. *Journal of China University of Geosciences*, **19**, 207–216.

ZHAO, H., DAHL, T. W., CHEN, Z. Q., ALGEO, T. J., ZHANG, L., LIU, Y., HU, Z. and HU, Z. 2020. Anomalous marine calcium cycle linked to carbonate factory change after the Smithian Thermal Maximum (Early Triassic). *Earth-Science Reviews*, **211**, 103418.

# Sedimentological analysis by A.Baud

## 1. Wadi Musjah

Cycle 1 about 1m thick, comprises a lower red ammonoid limestone part (level A) and an upper light beige bivalve coquina cemented biostrome (level B). The irregular dissolution boundary between the level A and B (supplementary fig. 1) is due to strong pressure solution. The microfacies of level A consist of bioclastic partly recrystallized lime mud, with packed, partly crushed bivalve shells surrounded of ammonoid shells, peloides, rare bryozoan and echinoid spines. The microfacies of the light beige bivalve coquina (level B) consists of well sorted bioclastic, small sized monospecific bivalve tests (millimetric), in a blocky calcite cement matrix.

The Cycle 2, 0.9 m thick, illustrated in supplementary fig. 2, comprises, as cycle 1, a lower bivalve rich red ammonoid limestone part (level C) and an upper light beige bivalve coquina cemented biostrome (level D). The microfacies of the red limestone shows a well sorted bioclastic packed short sized (millimetric) monospecific bivalve tests in red lime mud and bioclastic lime mud, with packed, partly crushed bivalve shells within some ammonoid shells. It is interesting to note that the ammonoid samples WM 8 of Brühwiler et al. (2012) with *Inyoites oweni* is coming from level C and was analyzed for further studies on the ammonoid shell structure (Klug 2007). The microfacies of the light beige bivalve coquina (level D) is a well sorted bioclastic short-sized monospecific bivalve tests (millimetric) in a calcite cemented matrix.

The Cycle 3, 0.5 m thick comprises, as the two previous cycles, a lower red ammonoid limestone part (level E) and an upper light gray bivalve coquina cemented biostrome with some brachiopod shells (level F). The microfacies of level E consist of bioclastic lime mud, with packed, partly crushed bivalve shells within ammonoid shells (supplementary fig. 2 E). From this level is the Bruehwiler et al. (2012) ammonoid level WM 7 with a *Juvenites* fauna. Brachiopod shells appear in the upper light gray bivalve coquina.

The Cycle 4, 0.5 m thick, is showing the sudden crinoidal invasion with ossilcles deposited in rose lime mud (level G) followed by a light gray brachiopod coquina cemented biostrome (level H). The microfacies of the crinoidal limestone consist of a bioclastic crinoidal packstone with brachiopod and bivalve crushed tests, ostracods and mini foraminifera showing partly cemented laminae in dark red lime muddy matrix, partly recrystallized (supplementary fig. 3). The *Anasibirites* ammonoid fauna was found from level G.

The Cycle 5, 1.3 m thick, consist of a thick bioclastic lime mud slightly recrystallized with crinoids, brachiopods levels and rare unidentifiable ammonoids, followed by light bioclastic, high-energy crinoidal cemented grainstone. The microfacies of the bioclastic red limestone (level I) shows brachiopod shells in a lime muddy matrix with bivalve crushed tests, ostracods and some crinoid

ossicles; but also crinoidal limestone and some sponge fibers of crushed sponge bodies can be found (see supplementary fig. 4).

The microfacies of the overlying high energy light rose crinoidal limestone (encrinites) (level J) shows densely packed crinoidal ossicles and spines in cemented matrix with brachiopod and bivalve crushed tests, ostracods and rare intraclasts.

The base of Cycle 6, 0.5m, is visible and consists of a bioclastic lime mud with brachiopod rich levels, crinoids, and crushed thin shelled bivalves. The microfacies (level K) shows full brachiopod sections in a dark lime muddy matrix withthin bivalve shells, ostracods, crinoid ossicles and small sized foraminifers.

## 2. Jebel Aweri

### 2.1 Lower block, description of lower block (parts A – C)

The lower part A (see fig. 3) consists of five cycles of shell supported biostrome and clast supported bioherm succession

Cycle 1, 1.1m thick comprises a lower shell supported biostrome part and an upper bioherm part with the following microfacies of cycle 1a and cycle 1b. Cycle 1a consists of a bivalve shells boundstone with early diagenetic cement. Microfacies of cycle 1b consists of a dentrolitic stromatolite with a “cloudy” appearance of the 2-3mm spaced microbial crust and a dendrolite boundstone (supplementary fig. 8 A, B).

Cycle 2, 2.9m thick, is made of thin bedded, coquinite at the base and the bioherm consists of dendrolitic type stromatolite similar to cycle 1. The microfacies consists of a dendrolitic stromatolite, with microconchids and possible bryozoans in cycle 2a and microbial peloid boundstone with microconchids, stromatactis and possible sponge fibers in cycle 2b.

Cycle 3, 2.5m thick, consists of a basal coquinite biostrome (3a) and a bioherm made of boundstone clasts coated by synsedimentary radial-fibrous cement. (supplementary fig. 7 A -E, part of 3b).

Cycle 4, 1.7m thick, is made of thin bedded, coquinite at the base (microfacies of cycle 4a, a cemented bivalve coquina, supplementary fig. 5 E) followed by well laminated stromatolite with domal and partly broken structures (supplementary fig. 6 A). The microfacies of cycle 4b shows millimetric contorted dark laminae belonging to dendrolitic stromatolite (supplementary fig. 6 B, C).

Cycle 5, 1.8m thick, consists of well bedded coquinite at the base (microfacies of cycle 5a, supplementary fig. 5 C) cemented stacked bivalve shells and dark intraclasts surrounded by yellowish fibrous calcite cement followed by light calcite needles (former aragonite?), and of a bioherm made dendrolite boundstone with rare bioclastes (cycle 5b).

The biostrome middle part (B) consists of a lower bivalve shell accumulations Level 6) (supplementary. fig. 5 A) followed by a brachiopod shell level 7 and a mixed bivalve and brachiopod shell accumulations (level 8, supplementary. fig. 5 D).

Level 6: 5.2 m thick, consists of cemented stacked bivalve shells (supplementary. fig. 5 B).

Level 7, 0.8m thick, is made of a cemented brachiopod accumulation and the microfacies shows the radial-fibrous cement surrounding the brachiopod shell and empty space filled by dark lime mud.

Level 8, 3m thick, consists of cemented stacked bivalve shells comprising two main levels 0.5 m thick richer in brachiopods, one about one meter above the level 7 and the second at the top. The microfacies of level 8 (illustrated in the supplementary material) is showing cemented and encrusted stacked bivalve shells and rare crinoid ossicles.

Part C consists of the bioherm top with lime clasts (level 9). Level 9, 2.2m thick, is showing an apparently erosive base over the shell level 8.

The base of level 9 consists of lime clast with a thrombolytic type of microbialite and a colony of possible sponge bodies with radial-fibrous cement filling stromatactis voids. The microfacies shows, as in cycle 3, many boundstone clasts (here possible sponge bodies) coated by synsedimentary radial-fibrous cement (lower part of level 9), and an upper part mainly of centimetric to decimetric lime clasts surrounded by microbial peloid boundstone with bioclasts and crinoid ossicles supplementary. fig. 8 E, F).

**2.2 Description of the upper block (parts D-F)**

The upper block, early Spathian in age, is more diversified and subdivided in 6 levels (10-15), with a shell supported biostrome base, a bioherm with clasts upper part and a top characterized by a crinoidal biostrome, overlaid by red lime mudstone.

Part D (=Level 10), 1m thick, is similar to level 7 and consists of a biostrome of stacked, cemented brachiopod shells with preserved shell structure surrounded by fibrous calcite cement within an incrusted grainstone matrix and crinoid ossicles.

Part E consists of level 11-13. Level 11, 2m thick, consists of a biohermal microbial peloid boundstone with bioclasts and crinoid ossicles. Level 12, 1.8m thick, is a bioherm with the microfacies showing a peloid microclotted dendrolite type of microbialite. Level 13, 2m thick, consists partly of clasts coated by synsedimentary radial-fibrous cement with voids of stromatactis type filled by fibrous calcite cement (supplementary. fig. 8 C). The microfacies is showing a reef clast with the coating of synsedimentary fibrous calcite (fc) cement (supplementary. fig. 8 D).

The uppermost part F consists of level 14 and 15). Level 14, 0.3m thick, consists of a crinoidal biostrome, with the microfacies showing a microbial stabilized peloid grainstone with crinoid ossicles, echinoid spines, microforaminfera, and rare fragmented bivalve and brachiopod shells

Level 15, 0.3m visible, is a rose-colored lime mudstone, Hallstatt type (supplementary. fig. 8 G).

## References

BRÜHWILER, T., BUCHER, H., GOUDEMAND, N. & GALFETTI, T. 2012. Smithian (Early Triassic) ammonoid faunas from Exotic Blocks from Oman: taxonomy and biochronology. *Palaeontographica* Abteilung – Palaozoologie-Stratigraphie 296, 3-107.

KLUG, C., BRÜHWILER, T., KORN, D., SCHWEIGERT, G., BRAYARD, A. AND TILSLEY, J., 2007. Ammonoid shell structures of primary organic composition. *Palaeontology*, *50*(6), pp.1463-1478. https://doi.org/10.1111/j.1475-4983.2007.00722.x

## Figures

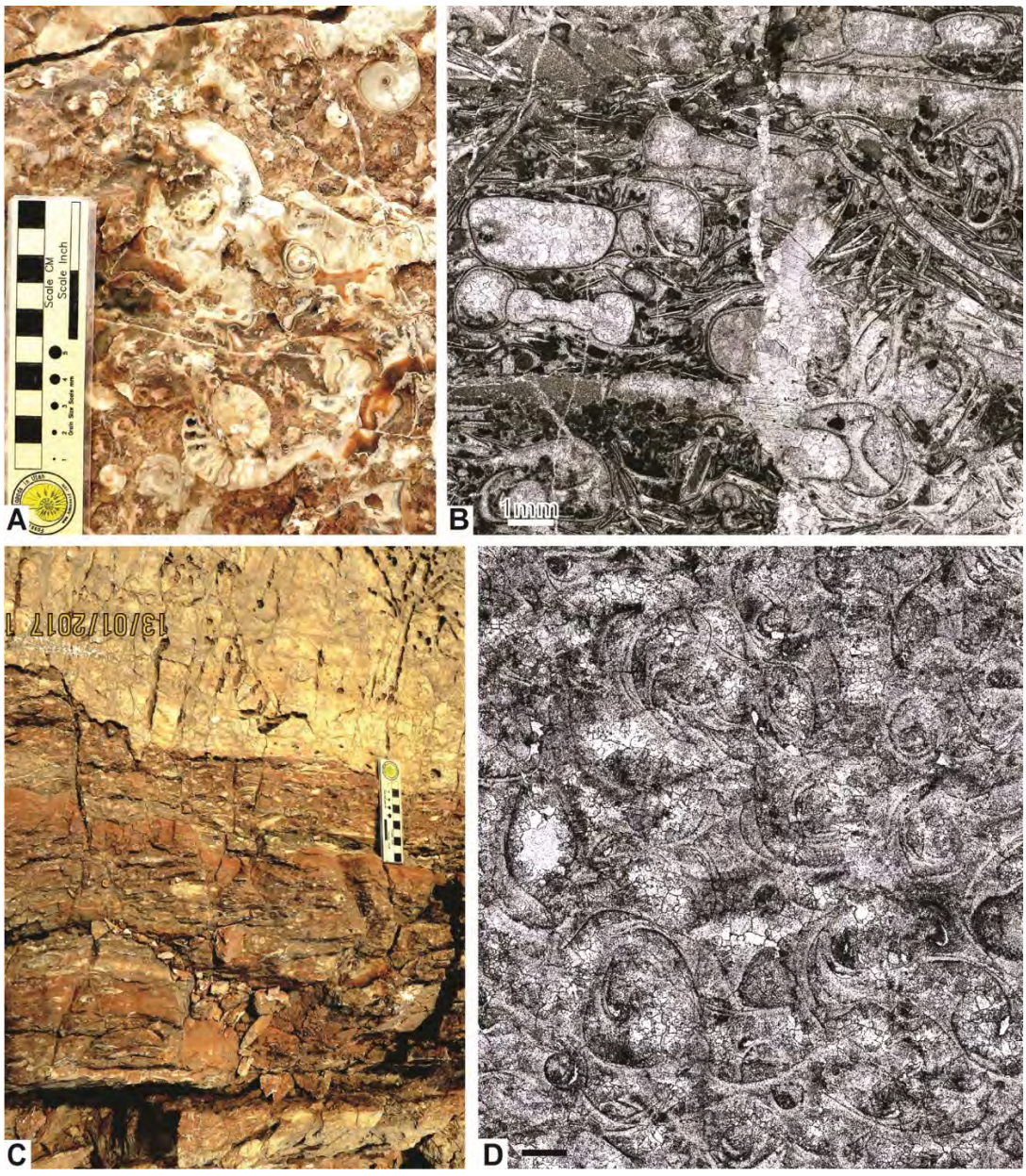


***Supplementary figure 1 : Wadi Musjah; A****: outcrop view of the red ammonoid limestone level A, base of the outcrop.* ***B:*** *Microfacies (level A, WM8iso, bioclastic recrystalized limestone with packed, partly crushed bivalve shells within ammonoid shells, peloides, intraclasts and echinid spines (scale bar=1mm).* ***C:*** *outcrop view of part of Cycle 1, with the contact between the red ammonoid limestone level A and the beige bivalve coquina cemented biostrome level B.* ***D:*** *Microfacies (from level B, between WM iso 11 and WM iso 12), bioclastic limestone with calcite cemented packed, millimetric, thin shelled bivalves (biostrome, scale bar=1mm).*

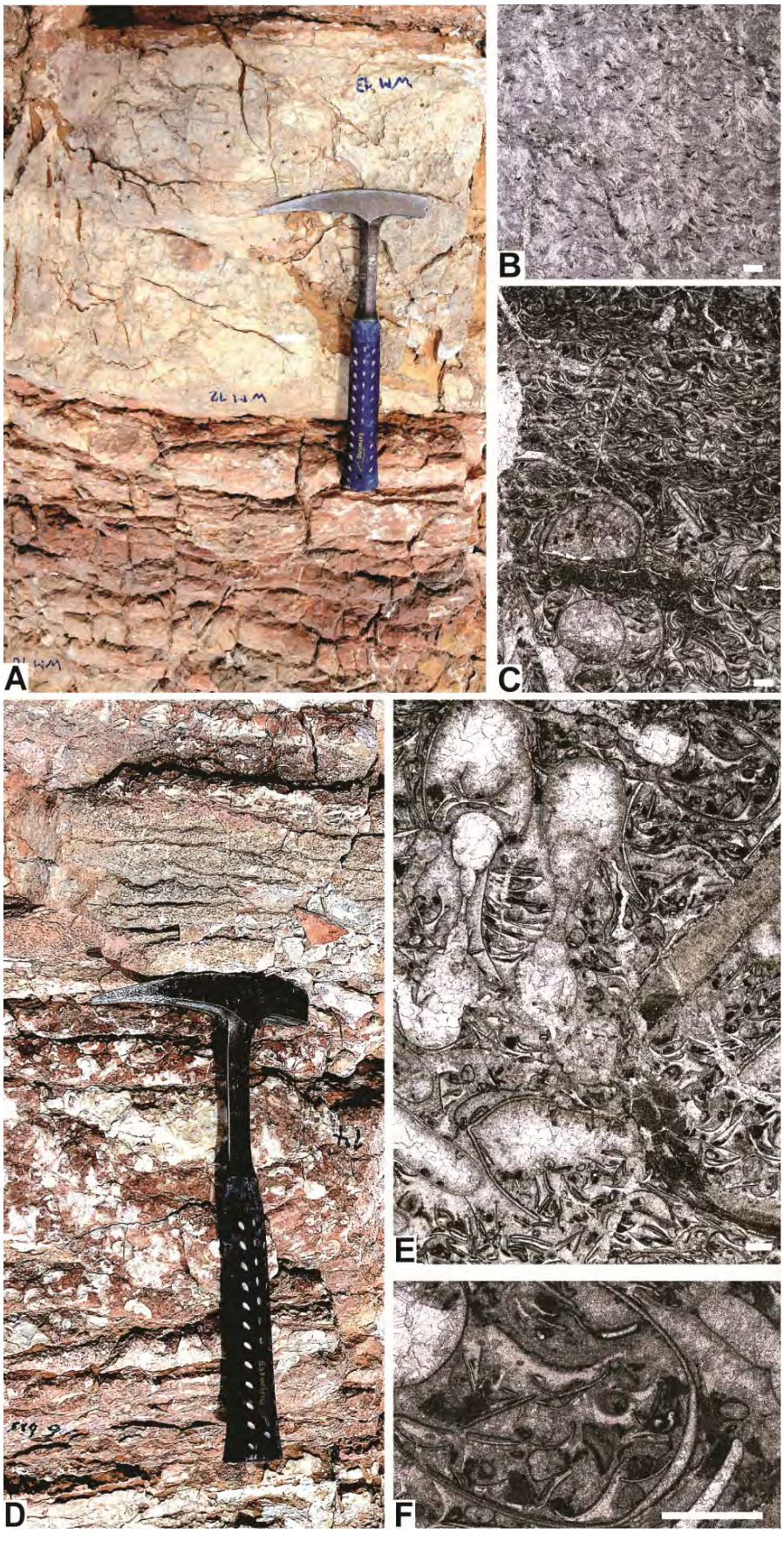


***Supplementary figure 2: Wadi Musjah; A:*** *outcrop view of Cycle 2,with the contact between the red ammonoid limestone level C and the beige bivalve coquina cemented biostrome level D;* ***B:*** *Microfacies from level D (WM iso 16), bioclastic limestone with calcite cemented packed, millimetric, thin shelled bivalves (biostrome);* ***C:*** *Microfacies from level C (WM iso 15), bioclastic lime mud with packed, thin shelled bivalve and some ammonoid shells (scale bar=1mm).* ***D:*** *outcrop view of Cycle 3, with the contact between the red ammonoid limestone level E and the gray bivalve-brachiopod coquina cemented biostrome level F;* ***E:*** *Microfacies from top of level E (WM iso 20), bioclastic lime mud slightly recrystalized with ammonoid shells and thin shelled bivalve (scale bar=1mm).* ***F:*** *detail of microfacies from top of level E (WM iso 20).*

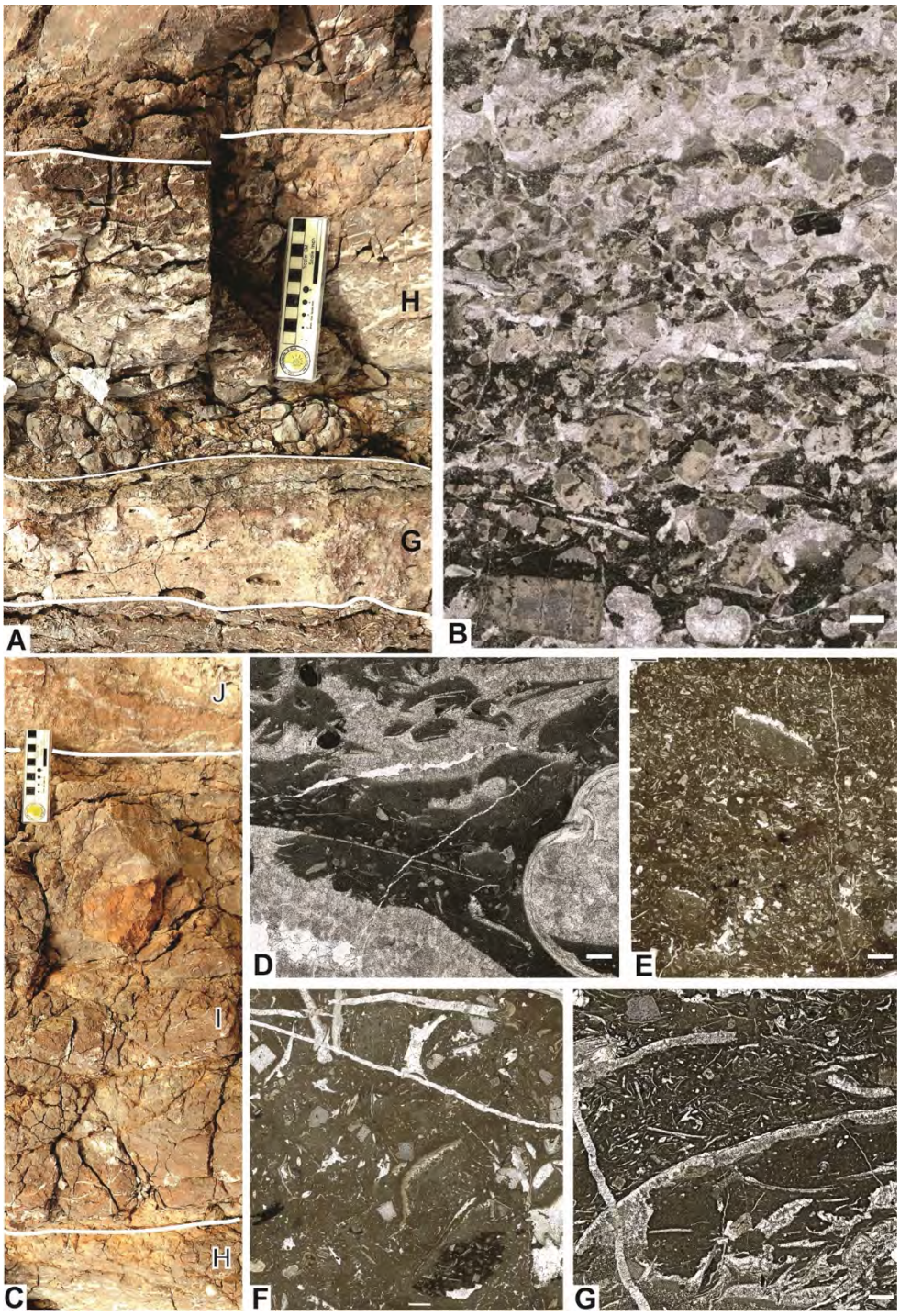


***Supplementary figure 3: Wadi Musjah; A:*** *outcrop view of Cycle 4, with the contact between the rosa coloured crinoidal limestone level G and the gray brachiopod coquina cemented biostrome level H;* ***B:*** *Microfacies from upper part of unit G (WM iso 23), bioclastic crinoidal lime packstone (scale bar=1mm). Figure 9,* ***C:*** *outcrop view of lower part (level I) of Cycle 5, showing the contacts with the underlying level H and the overlying level J.* ***D****=Microfacies from lower part of level I (WM iso 26), bioclastic lime packstone with preseved brachiopods and gastropods shells, crushed thin shelled bivalve and crinoid ossicles in a lime mudy matrix;* ***E****= Microfacies from middle part of level I (WM iso 28), bioclastic crinoidal lime packstone, with bivalve crushed tests, ostracodes and fibers of crushed sponges;* ***F****= Microfacies from upper part of level I, bioclastic crinoidal lime wackestone, with some crushed bivalve tests, fibers of crushed sponges and dark coloured intraclast;* ***G****= Microfacies from middle part of level I (WM 3 C), bioclastic limestone with recrystalized brachiopod shells, crushed thin shelled bivalve and crinoid ossicles in a lime mudy matrix (scale bar=1mm).*

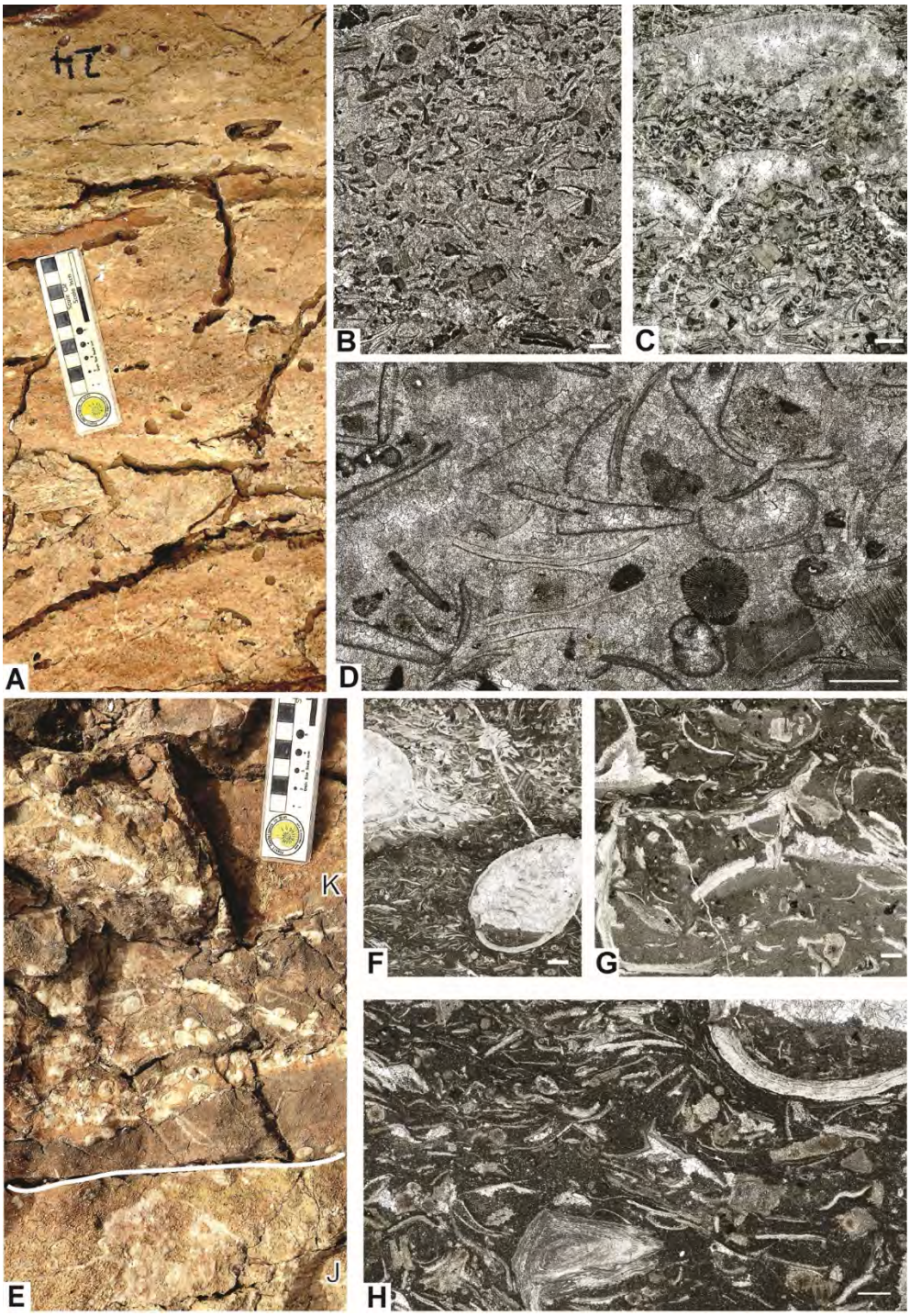


***Supplementary figure 4: Wadi Musjah; A:*** *outcrop view of the upper part (level J) of Cycle 5, with apparently crossbedded, light bioclastic, high energy crinoidal cemented grainstone. Microfacies:* ***B****= Microfacies from lower part of level J (WM iso 30), bioclastic crinoidal grainstone, with brachiopod and bivalve crushed tests, ostracodes and rare intraclasts;* ***C****= Microfacies from middle part of level J (WM 23 C), bioclastic grainstone with brachiopod and bivalve crushed tests, ostracode, crinoidal ossicles and spines, peloides and small intraclasts in calcite cemented matrix.* ***D****=enlargement of fig. 4.C (scale bar=1mm).* ***E:*** *outcrop view of the lower part (level K) of Cycle 6, showing the contacts with the underlying level J and a brachiopod abundance at the base, Microfacies:* ***F=*** *Microfacies from lower part of level K (WM 25 C), bioclastic brachiopod packstone with small bivalve shells, ostracodes, crinoides ossicles and mini-foraminifera in a dark lime mudy matrix;* ***G****= Microfacies from upper part of level J (WM 26 C), bioclastic packstone with crushed brachiopod and bivalves tests and crinoides ossicles;* ***H****=enlargement of fig. 4F; (scale bar=1mm).*

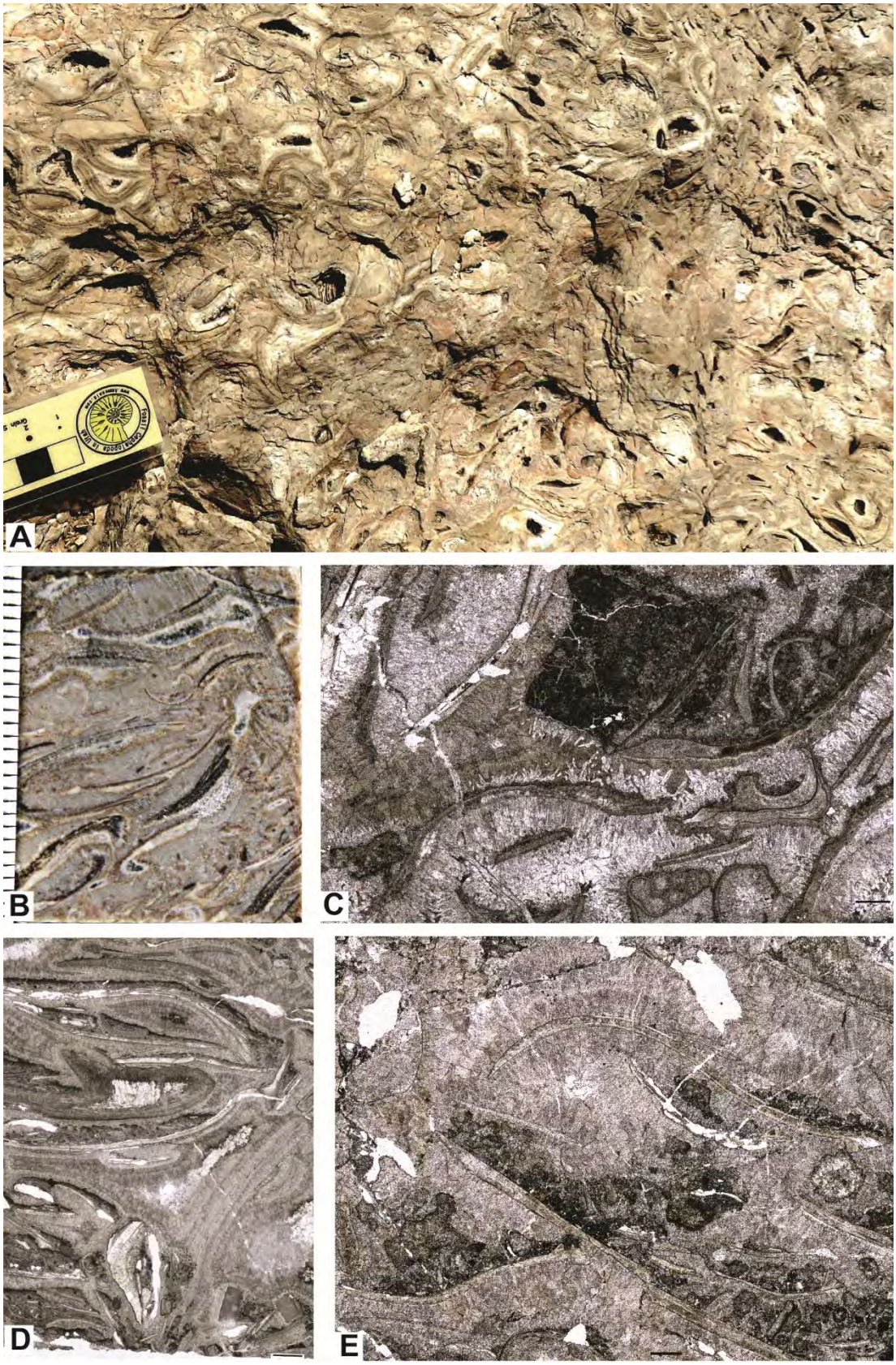


***Supplementary figure 5: Jebel Aweri; A:*** *outcrop view of a bivalve biostrome (level 6).* ***B:*** *polished surface of the biostrome, level 6.* ***C:*** *microfacies of level 5a;* ***D:*** *microfacies of level 8;* ***E:*** *microfacies of level 4a (scale bar=1mm).*

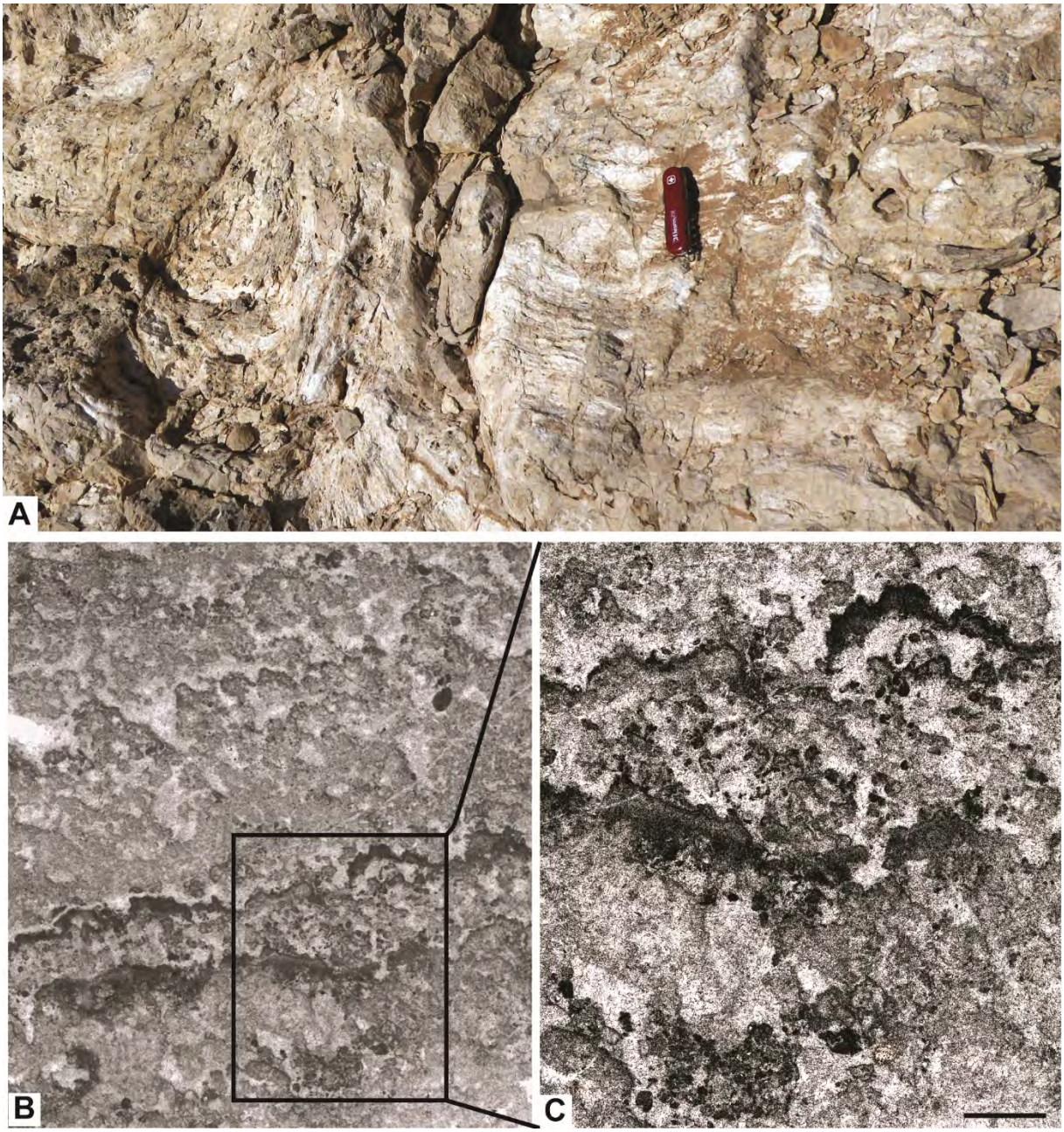


***Supplementary figure 6: Jebel Aweri; A:*** *outcrop view of level 4b with horizontal and domal stromatolite structures.* ***B and C:*** *microfacies showing dentrolitic stromatolite with a "cloudy" appearance of the 2-3mm spaced microbial crusts (both from level 4b, scale bar=1mm).*

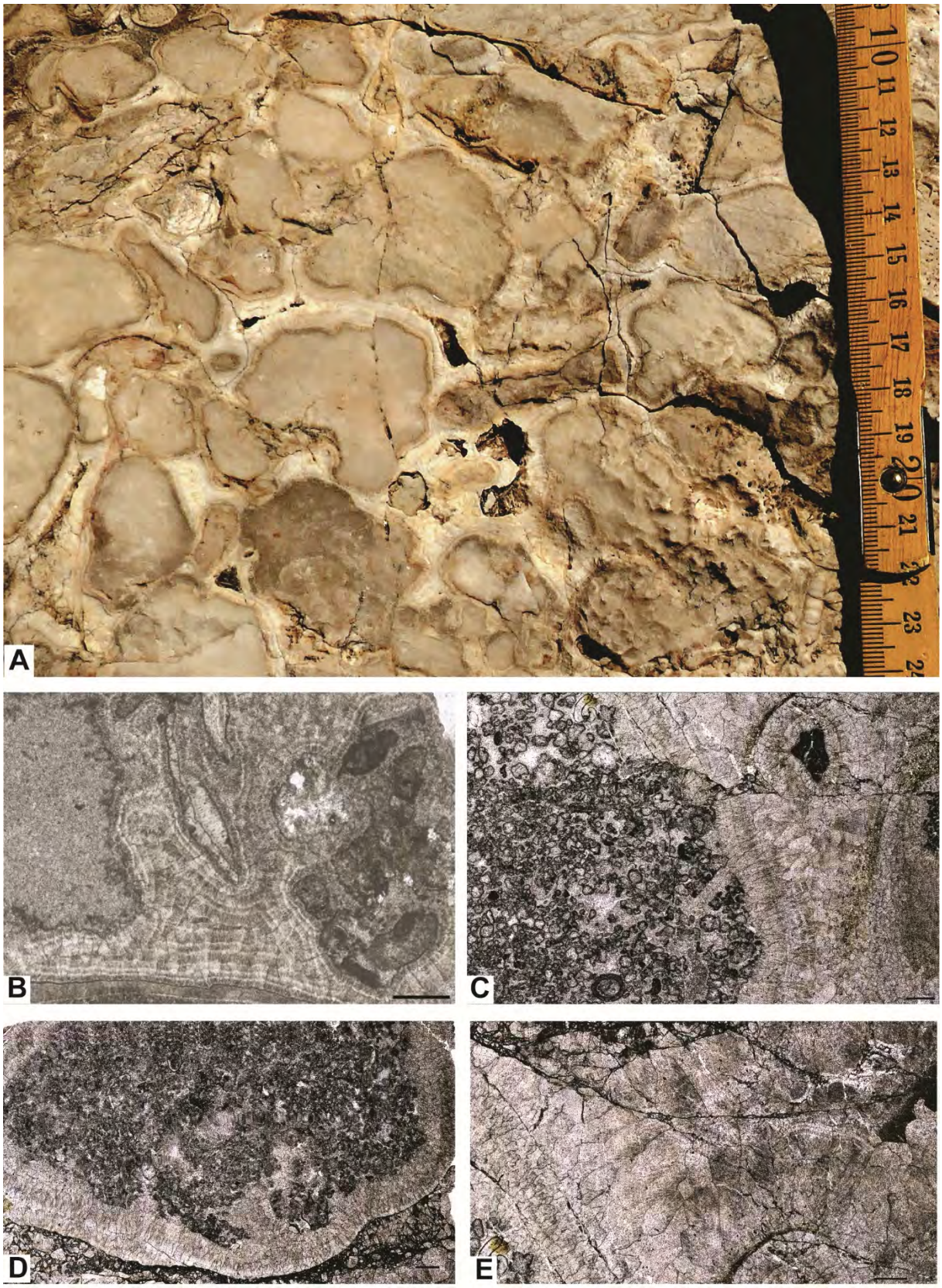


***Supplementary figure 7: Jebel Aweri; A level 3b:*** *outcrop view of reef clasts surrounded by fibrous calcite cement and voids filled by blocky calcite.* ***B:*** *clasts surrounded by fibrous calcite cement and voids filled by concentric and botroidal calcite cement.* ***C and D:*** *clasts surrounded by fibrous calcite cement.* ***E:*** *spheres in the "fibrous" cement. (scale bar=1mm.).*

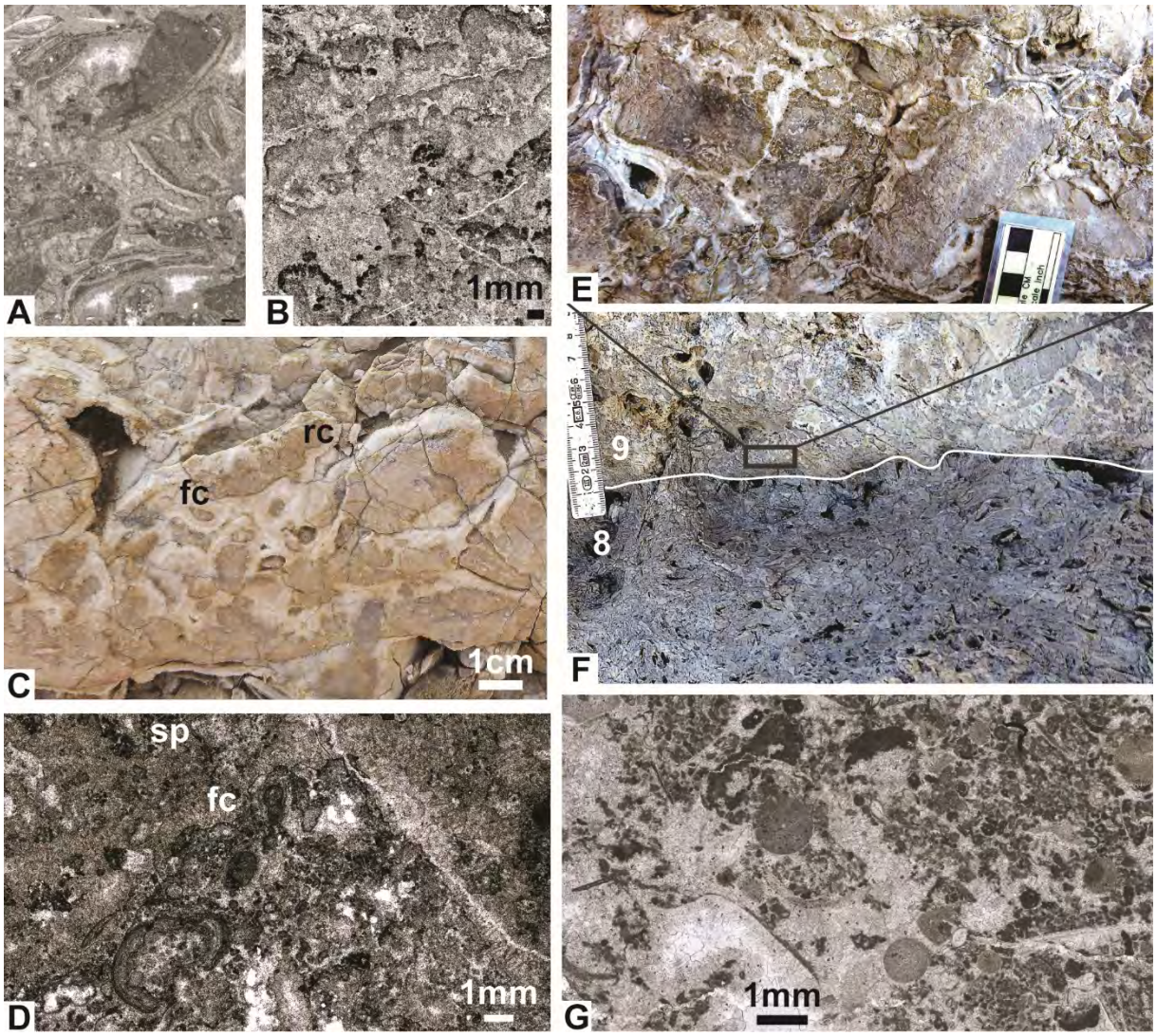


***Supplementary figure 8: Jebel Aweri; A:*** *bivalve shells boundstone with early diagenetic cement, from level 1b.* ***B:*** *dentrolitic stromatolite with a "cloudy" appearance of the 2-3mm spaced microbial crust from level 1b, scale bar=1mm).* ***C:*** *Outcrop view of part of level 13 with some reef clast (rc) and fibrous cement (fc).* ***D:*** *microfacies of level 13 with part of a reef clast surrounded by a millimeter thick synsedimentary radial-fibrous cement (fc). Possible sponge tissue (sp) in the upper part left.* ***E*** *(part of the view of fig. 8F)****:*** *outcrop view of the base of the bioherm level 9 with a thrombolite type of microbialite and possible sponge bodies surrounded by light radialfibrous cement filling also voids (possible crushed sponge bodies).* ***F:*** *outcrop view of the boundary between the top of the shell supported biostrome level 8 and the base of the clast supported bioherm level 9 with heterogeneous sized lime clasts in a calcite cementd matrix (rectangle corresponds to fig. 8E view).* ***G:*** *microfacies of level 15 showing a microbial stabilized peloid grainstone with crinoid ossicles, echinid spines, microforaminfera, and rare fragmented bivalve and brachiopod shells. (scale bar=1mm).*